TU/e EINDHOVEN UNIVERSITY OF TECHNOLOGY

# Validation, improvement and analysis of moving base simulation model

*Citation for published version (APA):*
Meulen, van der, S. H. (2004). *Validation, improvement and analysis of moving base simulation model*. (DCT rapporten; Vol. 2004.056). Technische Universiteit Eindhoven.

*Document status and date:*
Published: 01/01/2004

*Document Version:*
Publisher's PDF, also known as Version of Record (includes final page, issue and volume numbers)

*Please check the document version of this publication:*

• A submitted manuscript is the version of the article upon submission and before peer-review. There can be important differences between the submitted version and the official published version of record. People interested in the research are advised to contact the author for the final version of the publication, or visit the DOI to the publisher's website.
• The final author version and the galley proof are versions of the publication after peer review.
• The final published version features the final layout of the paper including the volume, issue and page numbers.

Link to publication

*General rights*
Copyright and moral rights for the publications made accessible in the public portal are retained by the authors and/or other copyright owners and it is a condition of accessing publications that users recognise and abide by the legal requirements associated with these rights.

• Users may download and print one copy of any publication from the public portal for the purpose of private study or research.
• You may not further distribute the material or use it for any profit-making activity or commercial gain
• You may freely distribute the URL identifying the publication in the public portal.

If the publication is distributed under the terms of Article 25fa of the Dutch Copyright Act, indicated by the "Taverne" license above, please follow below link for the End User Agreement:

www.tue.nl/taverne

*Take down policy*
If you believe that this document breaches copyright please contact us at:

openaccess@tue.nl

providing details and we will investigate your claim.

Download date: 16. Nov. 2023

# Validation, Improvement and Analysis of Moving Base Simulation Model

S.H. van der Meulen s0471815

Report No. DCT 2004.56

Research Report

Supervisors: prof.dr.ir. M. Steinbuch TU/e
ir. J. Ploeg TNO

Eindhoven University of Technology
Department of Mechanical Engineering
Dynamics and Control Technology Group

TNO Automotive
Advanced Chassis and Transport Systems
Advanced Transport Systems Group

Helmond, May 2004

# Abstract

Within the framework of a full scale Hardware-In-the-Loop intelligent vehicle simulator called VEHIL, TNO Automotive in Helmond has developed two automatic guided vehicles, which represent traffic participants. In order to validate the dynamic simulation model of these identical vehicles, called Moving Bases, several specific tests are developed, which are performed on both simulation and experimental level. Based on the results, the simulation model is improved and conclusions are drawn with respect to the validity of the simulation model and the performance of the real Moving Bases.

# Contents

# Chapter 1

# Introduction

## 1.1 Introduction

Among the most promising developments in road transport are driver support systems and fully automated intelligent transport systems. In this context, one can think of automatic cruise control systems or people movers. Such systems are highly mechatronic in nature and can be characterized by the presence of sensors, actuators and on-board computers, which convert the sensor information in commands to the engine and actuators. Extensive development and testing processes are necessary to ensure that these systems are safe and reliable, because the driving tasks of the driver are automated either partially or entirely.

Until now, the development process of intelligent transport systems leans on two important pillars. The first is computer simulation modelling. This method is relatively cheap and is ideal for analyzing and understanding the functional relations between the components and subsystems. The first specifications are often based on calculations with the simulation models. However, the quality of the simulation results strongly depends on the used structure as well as parameters and on the interpretation of the simulation engineer. To test the system behaviour and to validate the simulation results, full scale road tests with real prototypes are necessary. This is the second pillar, in which the human (test) driver can judge the functionality of the complete system. Due to the high system complexity and the limited controllability of test-conditions, this is the most expensive and time-consuming part of the development process.

To evaluate the functionality of intelligent vehicles, the vehicle's sensors and actuators have to be subjected to realistic driving conditions, such as high vehicle speeds and large tracking distances. This usually involves expensive and risky outdoor full scale vehicle tests. TNO Automotive in Helmond has developed an alternative, in which a full scale intelligent vehicle can be tested in laboratory conditions, while realistic road conditions are being simulated. This reduces the necessary space and vehicle speed considerably. As a result, the safety of the test engineers is greatly improved and the reproducibility of the tests increases.

In this 'VEhicle Hardware-In-the-Loop' (VEHIL) test facility, experiments on full scale intelligent vehicles and their infrastructure can be conducted. First, a virtual environment is defined, in which the vehicles, the infrastructure and their interactions are simulated. Next, the full scale Vehicle Under Test (VUT) is placed on a chassis dynamometer, providing a realistic drive line load and interfaced with this virtual environment. This is the Hardware-In-the-Loop aspect of the simulator: the unknown hardware (a validated simulation model of the new intelligent system is not available yet) is connected to a simulated environment. The VUT can be treated as a 'black box', of which its states (speed of travel, steer angle, etc.) can be measured and communicated to a real-time traffic simulation. One or more surrounding traffic participants are selected to be represented by a 'real' artefact, the so called Moving Base (MB). The Moving Base is an autonomous positioning platform that responds to open loop position commands of the traffic simulator. The Moving Base carries out the relative motions to the VUT, which are in high correlation to the

throttle and steering actions of the VUT. Environment sensors of the VUT monitor the Moving Base reactions, which closes the HIL control loop: the VUT board computer thinks he is actually driving the vehicle. Figure 1.1 illustrates the described VEHIL concept.

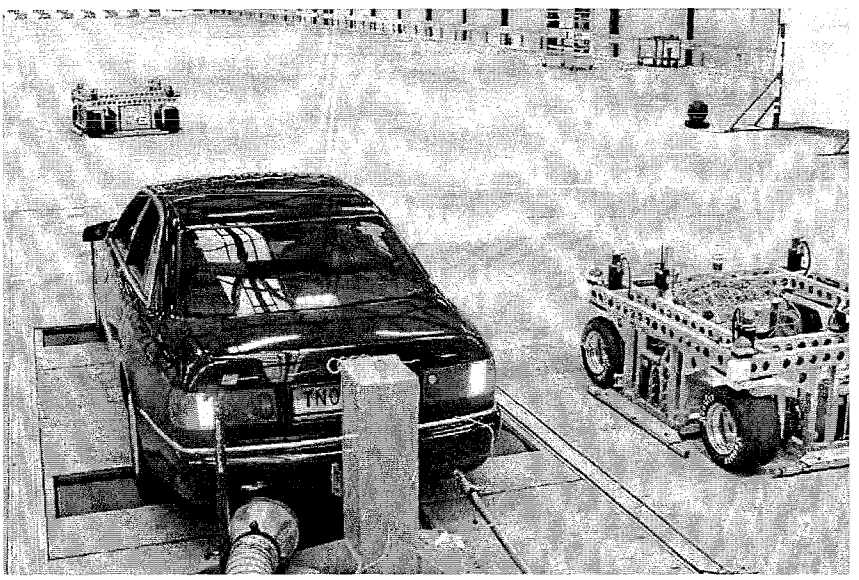

Figure 1.1: Impression of the VEHIL test facility.

As already mentioned, the Moving Bases are key components of the Hardware-In-the-Loop simulator, as they represent the surrounding traffic of the VUT. For this purpose, each Moving Base simulates the motion of a specific traffic participant relative to the VUT. As a matter of fact, these Moving Bases are intelligent vehicles in itself, as they are capable of autonomous path following. Consequently, the Moving Base is a true Automatic Guided Vehicle (AGV). To be able to execute the complex manoeuvres associated with the relative motion in VEHIL, this AGV must have an extreme freedom in manoeuvrability. Moreover, its dynamic response on position commands has to exceed the handling performance of modern road vehicles considerably.

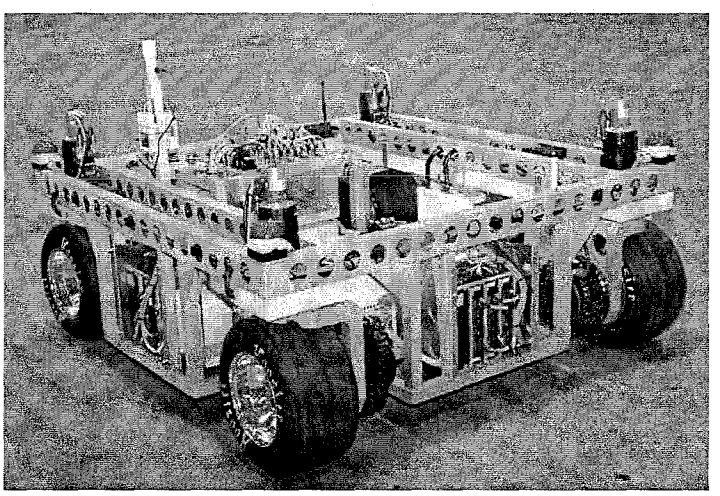

Figure 1.2: Moving Base I.

Within the framework described above, TNO Automotive has developed two high performance AGV's, called Moving Base I and Moving Base II, respectively. Moving Base I is depicted in figure 1.2. If required, a lightweight (plastic) representation of a car body can be mounted on the Moving Base chassis. This completes the resemblance to a normal vehicle in traffic, which can be important for accurate testing of the VUT's environmental sensors. Since the Moving Base has a four wheel drive and steering concept, it is possible to control the vehicle's three directions of movement independently of each other, see figure 1.3. The Moving Base platform is therefore designed to enable movement in the $x$-direction (a), the crab-like movement in the $y$-direction (b), a pure rotation around the center of gravity (c) and a combination of the aforementioned movements, namely a rotation around an arbitrary pole (d). Hence, it can be concluded that this concept enables the execution of complex manoeuvres at high speeds and accelerations.

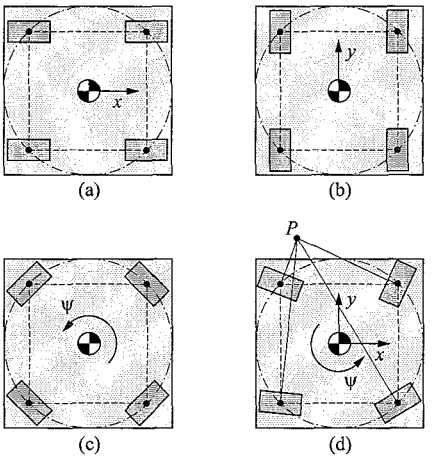


Figure 1.3: Moving Base platform concept.

An important feature of the applied design methodology is the application of a dynamic simulation model to support the system specification. This model has played a crucial role in the specification of the electric drives, the desired tyre characteristics, the battery package and the sensors. Also with respect to control system design, extensive use has been made of the simulation model. During the development process, the simulation model and the control system have been adapted in an iterative way, for instance based on data obtained from test rig experiments. By making use of these test rig experiments, component models have been validated and local control loops have been tested/tuned. The overall performance evaluation, however, must be based on full scale Moving Base experiments, which have not yet been performed.

## 1.2 Problem Statement

*Validate, improve and analyze the full Moving Base simulation model by making use of experimental data, obtained from newly to develop experiments.*

## 1.3 Approach and Overview

The research is started by investigation of the most important hardware components of the Moving Base. In this context, the Moving Base concept is highlighted and the actuator systems and sensor systems are discussed in chapter 2. During the investigation, increased knowledge with respect to hardware details is obtained, which appears to be useful later on in the research. However, the main reason to discuss the hardware components is found in the simulation model.

In order to validate and improve the complete Moving Base simulation model, it is necessary to obtain a detailed view of the model. For this reason, the dynamic simulation model is discussed in chapter 3, where it appears to be relatively complex. The model consists of several submodels, representing specific components of the Moving Base. Using the knowledge from chapter 2, the model structure is relatively easy to understand.

The Moving Base, like any other AGV, has to drive from its current position to a designated position along a desired trajectory. In order to realize this reference trajectory, a dedicated control system has been designed, which is discussed in chapter 4. With respect to the development of new experiments, it is necessary to understand the different control structures that are used. Moreover, this is important for the interpretation of the results and the evaluation of the control system.

After discussion of the simulation model and the control system, it is possible to validate the simulation model and to evaluate the overall performance of the Moving Base. To this end, new experiments are developed, which are performed using the simulation model as well as the real Moving Bases. After comparison of simulation and experimental results, it is possible to draw a conclusion about the validity of the simulation model and to improve the model. Depending on the experiment type, it is also possible to evaluate the performance of the Moving Base. The results are discussed in chapter 5.

From the experiments in chapter 5, it follows that the Moving Base control system functions properly. However, certain specific situations may occur during execution of a position reference trajectory, which require modifications of the controller. In order to obtain adequate modifications, the dynamic simulation model needs to be analyzed. This is the subject of chapter 6.

Finally, several conclusions and recommendations are given in chapter 7.

# Chapter 2

# Moving Bases

## 2.1 Introduction

Moving Bases are robot-vehicles that are used to simulate the traffic flow around the VUT in the VEHIL simulator. To execute the complex manoeuvres that arise from the relative movements of the vehicles surrounding the VUT, the Moving Base must be able to move freely in the horizontal plane. Furthermore, its dynamic response to a position command must significantly exceed the handling characteristics of modern vehicles.

During the development process and still, extensive use is made of a dynamic simulation model. Component specifications and control system design, for instance, are based on this model. At this moment, the simulation model is used mainly to obtain the Moving Base response on the application of specific position reference trajectories. In chapter 3, the dynamic simulation model is discussed and it appears to be relatively complex. The model consists of several submodels, representing specific components of the Moving Base. In order to obtain more insight in the model structure, it is desired to get a more detailed view of the hardware components of the Moving Base, such as the actuators and sensors.

For this reason, the most important hardware components of the Moving Base are discussed in this chapter. First, in section 2.2, the Moving Base concept is highlighted and general information is given. The actuator system can be divided into two systems: the electrical drive line and the electrical steering system. Both systems are discussed in section 2.3. To be able to calculate the position, for example, the Moving Base is equipped with several sensors. The relevant sensor equipment, required during the experiments later on, is considered in section 2.4.

## 2.2 Concept

The Moving Base platform design is based on a four wheel drive and four wheel steer concept, which allows for a high handling performance in combination with the ability to execute very complex manoeuvres. These performance requirements are accomplished using four high power AC servo motors for generating the traction forces and four additional AC servo motors for controlling the steer angles. Furthermore, special attention has been paid to the design of a lightweight aluminium space frame vehicle chassis, with the center of gravity located close to the road. The on-board energy is provided by a battery package, consisting of NiMH D-cells, which is situated on the floor of the chassis. Table 2.1 lists the main specifications of the Moving Base.

In figure 2.1, Moving Base I is depicted and several on-board devices are indicated. One of the main components of the electronic infrastructure is the adaptorbox. The adaptorbox is the interface between dSPACE, actuator systems, sensor systems and communication system. Use is made of wireless ethernet for the communication between dSPACE ControlDesk and the dSPACE AutoBox, which is present in the Moving Base. This dSPACE system is a so called Rapid Control Prototyping (RCP) environment and is used as a development and application

Table 2.1: Moving Base specifications.

| | |
|---|---|
| wheel base | 1.4 [m] |
| track width | 1.4 [m] |
| maximum speed | 50 [km/h] |
| maximum acceleration | 10 [m/s$^2$] |
| installed power | 30 [kW] |

platform for the Moving Base control system. Both the actuator systems and sensor systems will now be discussed more thoroughly in section 2.3 and section 2.4, respectively.

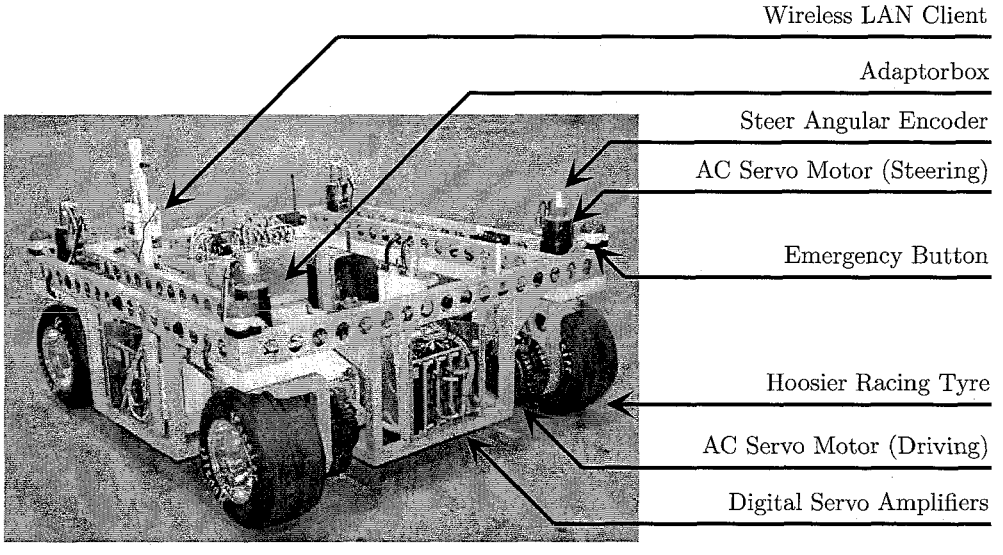


Figure 2.1: Moving Base I and on-board devices.

## 2.3 Actuator Systems

### 2.3.1 Electrical Drive Line

As a result of the four wheel drive concept, the Moving Base incorporates four identical electrical drive lines. The electrical drive line consists of several components, the most important one being the AC servo motor. In this case, use is made of the MAVILOR MA-55 AC Servo Motor, see appendix A and Mavilor Motors [Mav01] for important specifications. The choice for this AC servo motor is made because it is of a servo disc type, allowing a compact design with a high torque-weight ratio. Furthermore, it incorporates a fail-safe holding brake within the structure of the motor and a built-in resolver, which can be used to obtain the angular velocity. Notice that this servo motor is controlled by a digital servo amplifier. The outgoing motor shaft is connected to a SERVOFIT planetary gear set, see appendix A for the corresponding specifications. A reduction in angular velocity is accomplished by this planetary gear set, which is connected to the wheel. Use is made of aluminium wheels, in combination with HOOSIER racing tyres ($18.0 \times 7.5 - 10$).

### 2.3.2 Electrical Steering System

Similar to the electrical drive lines, the Moving Base incorporates four identical electrical steering systems. Each electrical steering system consists of three main components. The first component is the AC servo motor, in this case the MAVILOR MSA-02 AC Servo Motor, see appendix A and Mavilor Motors [Mav] for more details. Again, this servo motor is controlled by a digital servo amplifier. In order to obtain the steer angle, a FRABA absolute value encoder is connected to the AC servo motor. The outgoing motor shaft is connected to a SUMITOMO CYCLO EUROPE planetary gear set, see appendix A for the corresponding specifications. This planetary gear set accomplishes a reduction in angular velocity and is connected to the wheel suspension.

## 2.4 Sensor Systems

In order to determine, for instance, the position and velocity of the Moving Base, it is equipped with several sensor systems. Two of these sensor systems are discussed in subsection 2.3.1 and subsection 2.3.2. The first sensor is the resolver in the drive line AC servo motor, to determine the wheel angular velocity. The second sensor is the absolute value encoder, connected to the steering system AC servo motor, to determine the steer angle. However, more sensor systems are present. In this section, the remaining relevant sensor equipment, required during the experiments later on, is discussed.

### 2.4.1 Fiber Optic Gyro

Angular rotation is one of the parameters that needs to be accurately measured in order to control the position and orientation of the Moving Base. For this reason, a KVH E-Core 2000 Fiber Optic Gyro is mounted on the Moving Base, which measures the rate of rotation about a single axis. The physical principle of operation is based on the Sagnac effect, which is analogous to the Doppler effect, but in this case it involves determination of the phase shift between two counterpropagating light beams.

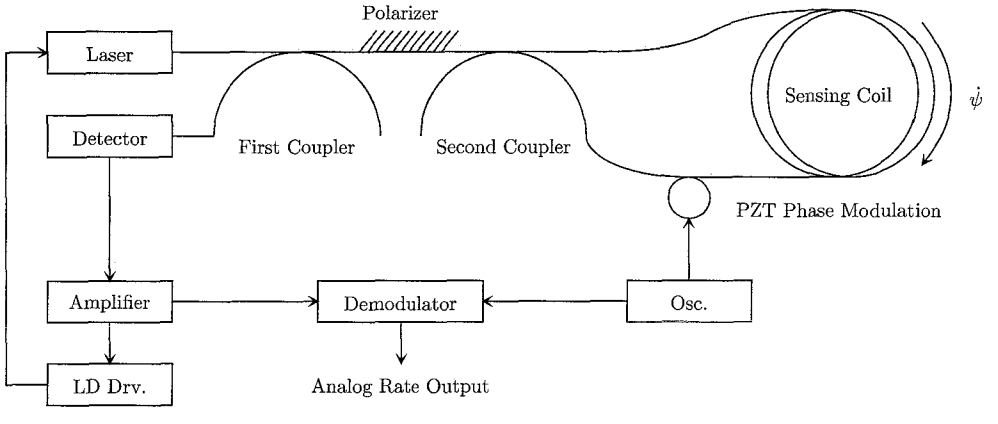


Figure 2.2: Block diagram of optical and electronic circuits of an open loop fiber optic gyro.

In figure 2.2, the open loop configuration of an (interferometric) fiber optic gyro is illustrated, which consists of a fiber coil, two directional couplers, a polarizer, optical source (laser) and detector. A piezoelectric (PZT) device, wound with a small length of one end of the fiber coil, applies a non-reciprocal phase modulation. Light from the laser traverses the first directional coupler, polarizer and second directional coupler, where it is split into two signals of equal intensity that travel around the coil in opposite directions. Subsequently, the light recombines at the coupler, returning through the polarizer and half of the light is directed by the first coupler into a photodetector.

Notice that both directions of light travel are through the same path and almost all environmental effects, except rotation, have the same effect on each beam and are, therefore, cancelled. The light intensity returning from the coil to the polarizer is a sinusoidal function of the Sagnac phase shift, having a maximum value when there is no rotation and a minimum value when the optical phase difference is half an optical wavelength. Due to the fact that the Sagnac phase shift is a known function of the angular velocity about the sensitive axis, it is possible to determine the latter. This can be done very accurately, as a result of the usage of special materials and dedicated signal processing techniques. However, the fiber optic gyro output signal may show a bias drift as a function of time, which varies slowly with temperature. In case more details are desired, the reader is referred to Bennett et al. [BDA+98].

### 2.4.2 Accelerometer

In order to measure the acceleration of the Moving Base, a CROSSBOW high sensitivity three axis accelerometer is mounted on the chassis. This acceleration sensor allows the measurement of acceleration in $x$-, $y$- and $z$-direction. The sensing element is a bulk micro-machined three layer silicon structure. These three layers form a differential capacitor with low noise. The sensor is bounded to a high-quality ceramic substrate, where it is coupled to signal conditioning electronics. For more information, the reader is referred to Crossbow Technology [Cro].

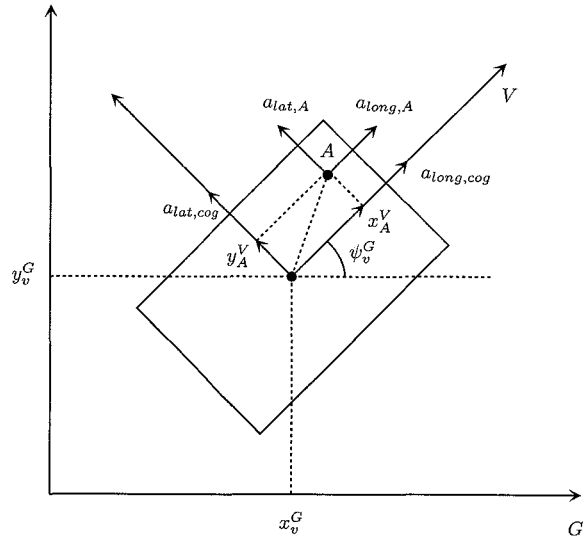


Figure 2.3: Definition of coordinate reference systems for acceleration transformations.

Due to the fact that the sensor is not mounted in the center of gravity of the Moving Base, certain signal transformations are required. Consider figure 2.3 for this purpose. In this figure, a top view of the Moving Base is depicted. The global coordinate reference system is indicated by $G$, while the vehicle coordinate reference system is indicated by $V$. Assume that the accelerometer is mounted in point $A$. Next, it is desired to transform the measured accelerations $a_{long,A}$ and $a_{lat,A}$ into the accelerations in the center of gravity $a_{long,cog}$ and $a_{lat,cog}$. This is done according to the following relations:

$$\begin{aligned} a_{long,cog} &= a_{long,A} + \ddot{\psi}_v^G y_A^V + \dot{\psi}_v^{G^2} x_A^V \\ a_{lat,cog} &= a_{lat,A} - \ddot{\psi}_v^G x_A^V + \dot{\psi}_v^{G^2} y_A^V, \end{aligned} \tag{2.1}$$

where $x_A^V$ and $y_A^V$ are constant lengths. A disadvantage of the accelerometer being placed out of the center of gravity is that the yaw acceleration $\ddot{\psi}_v^G$ is required for the transformation.

### 2.4.3 Magnet Grid and Rulers

To be able to carry out real-time experiments, it is of great importance to know exactly where on the laboratory floor the Moving Base is. At this moment, two separate position measuring systems are being used for this purpose. As already mentioned in this chapter, the drive line and steering system motors are provided with encoders, which measure the wheel angular velocity and the steer angle, enabling a specific algorithm to derive the position of the Moving Base relative to a known start position. This method is referred to as odometry and is sensitive to tyre slip.

The second position measuring system does not have this disadvantage and consists of a magnet grid in the laboratory floor, combined with four linear antenna's (rulers) on each Moving Base. A close-up of the ruler on the front of the Moving Base is shown in figure 2.4. In figure 2.5, the magnet grid is depicted, which consists of 8000 magnets in a diamond shaped pattern at distances of 1 meter. Each time a ruler passes a magnet, this is registered and it is possible to derive the location of the Moving Base. Both position measuring systems are combined in a discrete Kalman filter, which is discussed in section 4.5.

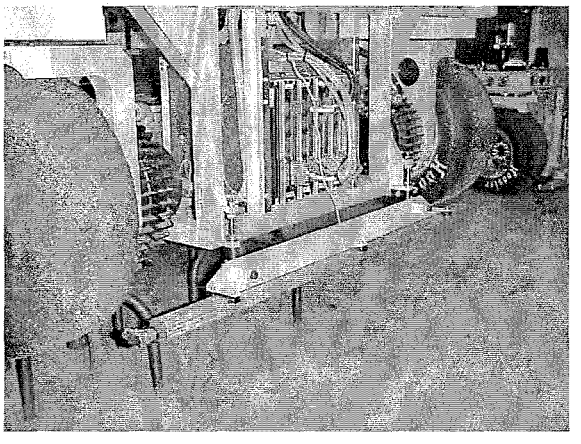

Figure 2.4: Close-up of Moving Base front ruler.

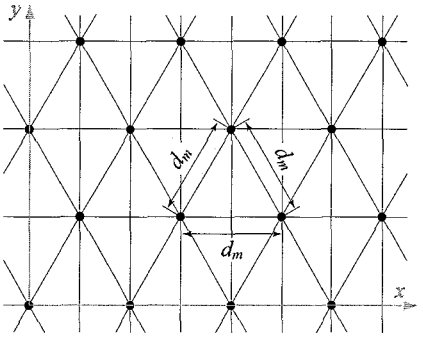


Figure 2.5: Magnet grid pattern.

# Chapter 3

# Simulation Model

## 3.1 Introduction

Considering the high performance requirements that the Moving Base must satisfy and the tight time schedule, an efficient design process had to be applied. For this reason, a thorough design methodology has been adopted, which allows for a structured and efficient design process, see Ploeg et al. [PKV02]. An important feature of the design methodology is the application of a dynamic simulation model. The specification of the electrical drive lines, the electrical steering systems, the desired tyre characteristics, the battery package and the sensors is based on this model to a large extent. During control system design, extensive use is made of the simulation model as well.

The Moving Base simulation model is developed in MATLAB/SIMULINK and consists of several submodels. Basically, the main component models are the electrical drive line model, the tyre model, the electrical steering system model and the vehicle body model. By making use of test rig experiments, several component models and component specifications have already been validated. In order to validate and improve the complete Moving Base simulation model, it is necessary to obtain a detailed view of the model and its component models.

For this reason, the Moving Base simulation model is discussed in this chapter. In section 3.2, an overview of the structure of the simulation model is considered and the component models are indicated. Subsequently, the two-track vehicle model and the tyre model are highlighted in section 3.3 and section 3.4, respectively. The electrical drive line model is discussed in section 3.5, followed by the electrical steering system model in section 3.6. In case the information given in this chapter is insufficient, the reader is referred to Van der Knaap et al. [KP00].

## 3.2 Model Overview

In figure 3.1, the top layer of the Moving Base simulation model is depicted. The Moving Base itself is represented by the block 'AGV 2T 3DoF', which has several inputs and outputs. The inputs are given by the reference driving torques $T_{ij,drv,ref}$ and the reference steering torques $T_{ij,str,ref}$, where $i = 1, 2$ and $j = L, R$. Here, the index $i$ refers to the front and rear side of the Moving Base and the index $j$ to the left and right side of the Moving Base, respectively. The outputs are given by the different sensor signals. These are the steer angles $\delta_{ij}$, the wheel angular velocities $\omega_{ij}$, the accelerations in longitudinal, lateral and vertical direction, the yaw velocity $\dot{\psi}$ and the ruler output signals. Transformation of the sensor signals and addition of noise takes place in the block 'sensors'. Subsequently, the sensor signals are pre processed in the block 'signal pre-processing', after which they are available for control. The block 'controllers' incorporates the different control structures, see chapter 4. It makes use of position, velocity and acceleration reference signals $S_{mref}, V_{mref}, A_{mref}$ or just velocity reference signals $V_{mref}$, obtained from the remote control unit.

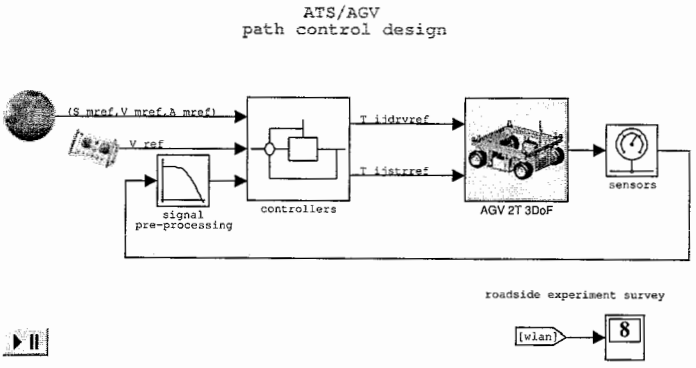


Figure 3.1: Moving Base simulation model top layer.

Next, the block 'AGV 2T 3DoF' will be investigated in more detail. The structure of this block is depicted in figure 3.2. It is obvious that there are four identical actuator systems, each consisting of an electrical drive line model, a tyre model and an electrical steering system model. Furthermore, a two-track, three degrees of freedom vehicle model is present, representing the AGV body. These submodels are discussed in the subsequent sections.

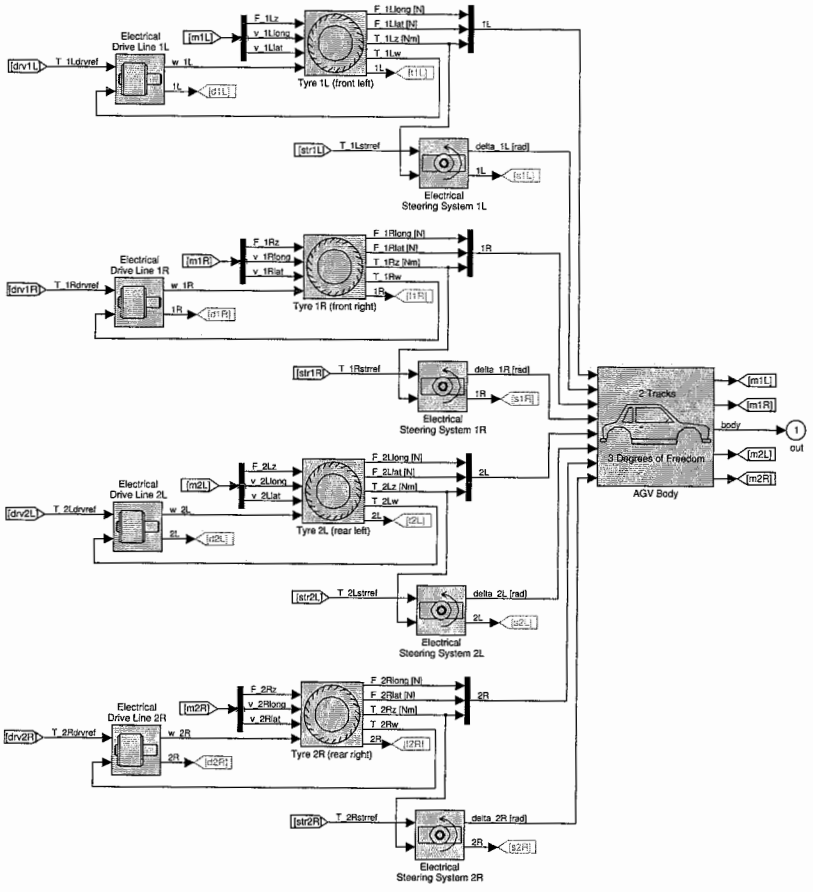


Figure 3.2: Moving Base simulation model AGV 2T 3DoF block.

## 3.3 Two-Track Vehicle Model

In order to analyze the four wheel drive and four wheel steer concept, it is necessary to develop a mathematical model of the relevant static and dynamic behaviour of the Moving Base. Consider the two-track vehicle model in figure 3.3 for this purpose. This figure shows the body of the Moving Base, as well as the forces and torques acting on it. These forces and torques, originating in the tyre-road contact patches, cause the vehicle body to move over a certain path. This path can be described as a rotation with respect to a momentary pole $P$. As the vehicle body is assumed to be rigid, the path of each specific point of the vehicle body has the same momentary pole $P$. Figure 3.3 demonstrates this principle by means of the paths of the body corners and the center of gravity (c.o.g.).

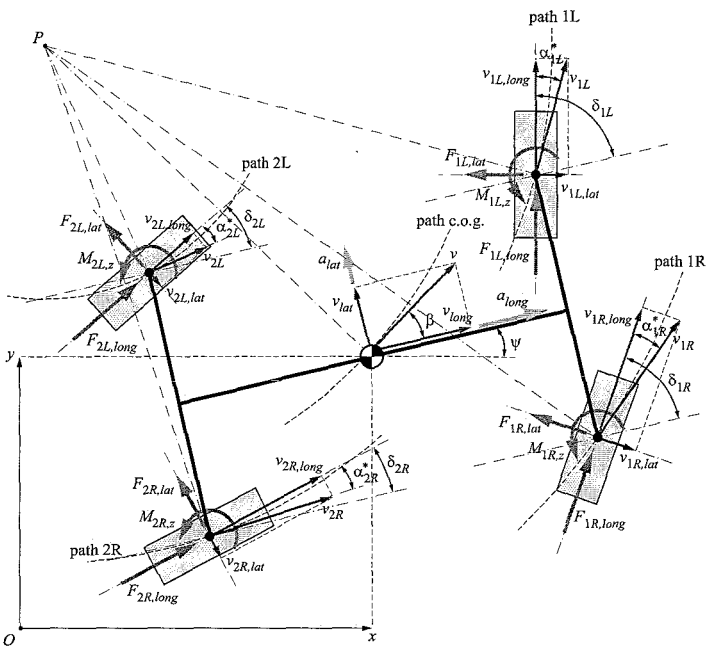


Figure 3.3: Two-track vehicle model.

The resulting position of the body is uniquely described by three coordinates, being $x$, $y$ and the yaw angle $\psi$ of the c.o.g. with respect to a fixed point $O$ in the absolute world. Notice that vertical motion of the body is neglected, because the Moving Base does not have wheel suspension. This leaves a negligible vertical motion, caused by elastic deformation of the tyres. The velocity and acceleration of the body can also be described in Cartesian absolute coordinates. It is, however, common to define velocity $v$ and acceleration $a$ in longitudinal and lateral direction with respect to the body, indicated by the subscripts *long* and *lat* in figure 3.3, respectively.

Based on the above, the equations of motion of the body model are as follows:

$$\begin{aligned} m\ddot{x} &= F_{1L,long}\cos(\psi+\delta_{1L}) + F_{1R,long}\cos(\psi+\delta_{1R}) + F_{2L,long}\cos(\psi+\delta_{2L}) + \\ &\quad F_{2R,long}\cos(\psi+\delta_{2R}) - F_{1L,lat}\sin(\psi+\delta_{1L}) - F_{1R,lat}\sin(\psi+\delta_{1R}) - \\ &\quad F_{2L,lat}\sin(\psi+\delta_{2L}) - F_{2R,lat}\sin(\psi+\delta_{2R}), \qquad (3.1) \\ m\ddot{y} &= F_{1L,long}\sin(\psi+\delta_{1L}) + F_{1R,long}\sin(\psi+\delta_{1R}) + F_{2L,long}\sin(\psi+\delta_{2L}) + \\ &\quad F_{2R,long}\sin(\psi+\delta_{2R}) + F_{1L,lat}\cos(\psi+\delta_{1L}) + F_{1R,lat}\cos(\psi+\delta_{1R}) + \\ &\quad F_{2L,lat}\cos(\psi+\delta_{2L}) + F_{2R,lat}\cos(\psi+\delta_{2R}), \qquad (3.2) \end{aligned}$$

$$
\begin{aligned}
I_z\ddot{\psi} \;=\; & L_1\left(F_{1L,long}\sin(\delta_{1L}) + F_{1L,lat}\cos(\delta_{1L})\right) - \frac{1}{2}S_1\left(F_{1L,long}\cos(\delta_{1L}) - F_{1L,lat}\sin(\delta_{1L})\right) + \\
& L_1\left(F_{1R,long}\sin(\delta_{1R}) + F_{1R,lat}\cos(\delta_{1R})\right) + \frac{1}{2}S_1\left(F_{1R,long}\cos(\delta_{1R}) - F_{1R,lat}\sin(\delta_{1R})\right) - \\
& L_2\left(F_{2L,long}\sin(\delta_{2L}) + F_{2L,lat}\cos(\delta_{2L})\right) - \frac{1}{2}S_2\left(F_{2L,long}\cos(\delta_{2L}) - F_{2L,lat}\sin(\delta_{2L})\right) - \\
& L_2\left(F_{2R,long}\sin(\delta_{2R}) + F_{2R,lat}\cos(\delta_{2R})\right) + \frac{1}{2}S_2\left(F_{2R,long}\cos(\delta_{2R}) - F_{2R,lat}\sin(\delta_{2R})\right) + \\
& M_{1L,z} + M_{1R,z} + M_{2L,z} + M_{2R,z}. \qquad (3.3)
\end{aligned}
$$

Here, $F_{ij,long}$ are the longitudinal slip forces, $F_{ij,lat}$ the lateral forces, $M_{ij,z}$ the torques acting in the tyre-road contact patch and $\delta_{ij}$ are the steer angles. These equations provide the coordinates $x$, $y$ and $\psi$ and their first and second time derivatives. By making use of these variables, the absolute velocity $v$ of the center of gravity can be calculated, as well as its longitudinal component $v_{long}$ and its lateral component $v_{lat}$. Expressions for the accelerations $a_{long}$ and $a_{lat}$ are obtained by projecting the accelerations in $x$- and $y$-direction on the longitudinal and lateral axes. In order to be able to calculate the slip values, required as an input for the tyre model (see section 3.4), the slip velocities of front and rear wheels have to be determined. These slip velocities are denoted by $v_{ij,long}$ and $v_{ij,lat}$, for $i = 1, 2$ and $j = L, R$. Notice that in this case the longitudinal and lateral directions are related to the rotated vertical wheel plane, see figure 3.3. For the explicit expressions, the reader is referred to Ploeg [Plo03a].

An additional input for the tyre model is the dynamical vertical tyre load, see section 3.4. In figure 3.4, a side view of the vehicle model is depicted. From this figure, it can be seen that the center of gravity is located at a certain height $h_{car}$ above the road. At vehicle standstill, the only force that acts on the c.o.g. is the gravitational force $F_{z,tot} = mg$. Subsequently, the static wheel loads can be computed by assuming that the c.o.g. is located exactly in the middle between the left and right wheels. Again, the reader is referred to Ploeg [Plo03a] for the equations.

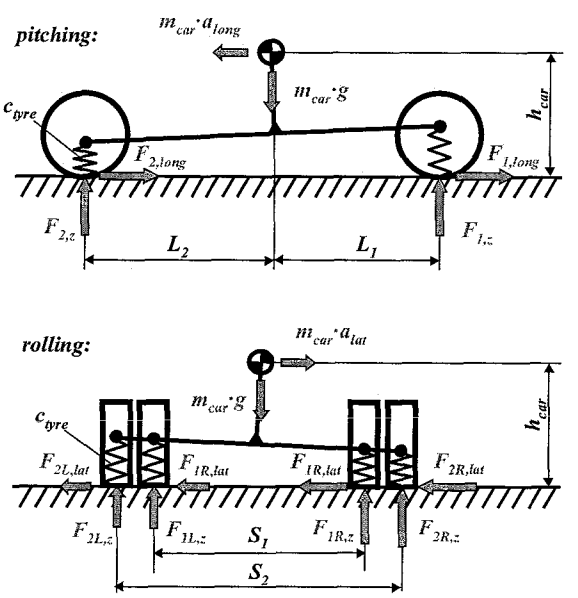


Figure 3.4: Dynamic vertical tyre load during pitching and rolling.

During accelerating and cornering, the total gravitational force remains constant, but its distribution between the four wheels is strongly dependent on the location of the c.o.g. and the level of longitudinal and lateral acceleration. In order to solve the four dynamic vertical tyre forces, vertical compliance has to be added to the model. With respect to the Moving Base, the only

compliance that has to be dealt with is the tyre vertical spring stiffness. The tyre vertical spring stiffness is considered to have a linear characteristic and to be identical for each wheel. Figure 3.4 shows views of the vehicle in a pitching and rolling condition, under the influence of the inertial forces acting in the center of gravity. Solving the forces in vertical direction and the moments of equilibrium about the lateral and longitudinal axis of the vehicle body, combined with the introduction of four identical vertical springs, the dynamic vertical tyre loads can be computed, see Ploeg [Plo03a]. The dynamical behaviours of the two dynamic load transfers are modelled by simple second order transfer functions:

$$\frac{\Delta F_{z,pitch}}{a_{long}} = \frac{K_{pitch}}{\frac{s^2}{\omega_{0,p}^2} + 2\beta_p \frac{s}{\omega_{0,p}} + 1}, \tag{3.4}$$

$$\frac{\Delta F_{z,roll}}{a_{lat}} = \frac{K_{roll}}{\frac{s^2}{\omega_{0,r}^2} + 2\beta_r \frac{s}{\omega_{0,r}} + 1}. \tag{3.5}$$

The parameter $\beta$ is the dimensionless damping coefficient, $\omega_0$ is the undamped frequency of the motions and the factor $K$ coincides with the dynamic load transfer terms. Both dynamic transfer functions are merely included to avoid any algebraic loops, but also represent realistic roll and pitch angle dynamics, to a certain extent.

## 3.4 Tyre Model

As already indicated, the main forces that control the course of the vehicle body are generated and transmitted in the contact patches between the tyres and the road. For this reason, a tyre model is used to compute the longitudinal force $F_{ij,long}$, the lateral force $F_{ij,lat}$ and the so called self aligning torque $M_{ij,z}$, which are indicated in figure 3.3.

In vehicle dynamics, the static longitudinal slip $\kappa_{ij,static}$ is used as an input variable for computing the longitudinal tyre force $F_{ij,long}$ and is defined by:

$$\kappa_{ij,static} = \frac{v_{s,ij,long}}{|v_{ij,long}|} = \frac{R_e\omega_{ij} - v_{ij,long}}{|v_{ij,long}|}, \tag{3.6}$$

where the longitudinal slip velocity $v_{s,ij,long}$ is defined as the difference between the rolling velocity of the wheel $R_e\omega_{ij}$ and the forward velocity of the wheel center $v_{ij,long}$. Notice that $\omega_{ij}$ denotes the wheel angular velocity and $R_e$ denotes the effective tyre rolling radius. For calculating the lateral tyre force $F_{ij,lat}$ and the self aligning torque $M_{ij,z}$, the lateral slip velocity $v_{ij,lat}$ is used for determining the static lateral slip $\alpha_{ij,static}$:

$$\alpha_{ij,static} = \frac{v_{s,ij,lat}}{|v_{ij,long}|} = \frac{v_{ij,lat}}{|v_{ij,long}|}. \tag{3.7}$$

It is well known that the force and moment responses of the tyre to various external inputs show a lag in time. The fact that tyre deflections (deflections of tyre side walls, carcass and rubber thread) have to be built up to create a force calls for a model that contains carcass compliance. This transient behaviour of the tyre is modelled by filtering the slip. Introducing the approximately constant relaxation length $\sigma_\kappa$, the transient characteristic of the tyre in longitudinal direction can be described using a first order transfer function:

$$\kappa_{ij} = \frac{1}{\sigma_\kappa s + |v_{ij,long}|}\left(R_e\omega_{ij} - v_{ij,long}\right), \tag{3.8}$$

where $s$ is the complex frequency. Similar to (3.8), the transient characteristic of the tyre in lateral direction is given by the transfer function:

$$\alpha_{ij} = \frac{1}{\sigma_\alpha s + |v_{ij,long}|} v_{ij,lat}, \tag{3.9}$$

where $\sigma_\alpha$ is the lateral relaxation length. A variation of the slip velocity $v_{s,ij,long}$ or $v_{s,ij,lat}$ will generate a transient slip through differential equation (3.8) or (3.9), which is used as an input for the stationary slip characteristics.

For modelling the non-linear tyre characteristics, an empirical tyre model, the so called Magic Formula, is used. This model is based on a set of mathematical expressions, with coefficients that are strongly related to the physical tyre properties (friction level, slip stiffness, etc.), representing experimental tyre data. The general shape of the Magic Formula for describing the pure slip characteristics is a sine function with an arctangent as an argument:

$$F^* = D \sin\left[C \arctan\left\{Bx - E(Bx - \arctan(Bx))\right\}\right], \tag{3.10}$$

where $F^*$ denotes the steady-state tyre characteristic and $x$ denotes the slip value $\kappa$ or $\alpha$. The coefficients $B$, $C$, $D$ and $E$ characterize the shape of the slip characteristics. The real Magic Formula, see Pacejka et al. [PB97], uses an enormous amount of parameters to describe the load, camber, ply-steer and friction dependencies of its coefficients. All these parameters have to be defined and validated in case a new tyre is used. Therefore, the objective of the tyre model is to use the Magic Formula's basic shape according to (3.10), but the definition of the tyre characteristics has to be fulfilled with a minimal set of parameters. This might lead to synthetic tyre characteristics that aren't a full representation of a real tyre, but at least the principal tyre properties, such as slip stiffness and friction level are depicted correctly. This makes the Moving Base manoeuvre in a very realistic manner, even at limit performance conditions.

On the left side of figure 3.5, the pure longitudinal slip curve as a function of $\kappa_{ij}$ is depicted, parameterized to the local vertical load $F_{ij,z}$. From this figure, it follows that the tyre behaviour shows a highly non-linear character, which strongly depends on the vertical load. This latter property plays an important role due to tyre load transfer during acceleration, deceleration and cornering. With respect to the lateral tyre behaviour, the same type of friction curve applies, as can be seen on the right side of figure 3.5. As a result of the tyre construction, the longitudinal slip stiffness, i.e. the slope of the longitudinal curve at $\kappa_{ij} = 0$, is approximately three times larger than the lateral slip stiffness.

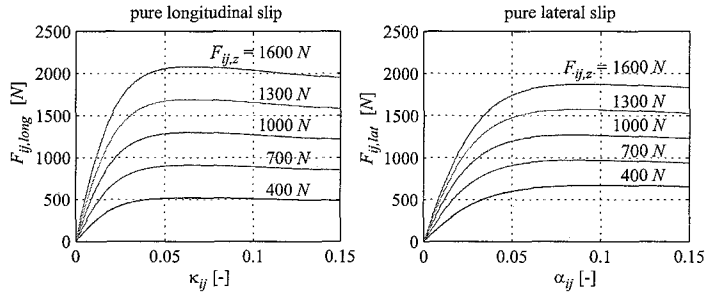


Figure 3.5: Pure longitudinal and lateral slip characteristics, parameterized to vertical load $F_{ij,z}$.

Due to the strong dependence of the characteristics on the level of vertical tyre load, the normalized slip characteristics are introduced. These are merely a division of the horizontal tyre force $F^*$ by the vertical tyre force $F_{ij,z}$, see Ploeg et al. [PK00]. In the model, its coefficients are labelled with *norm*. The shape of the normalized longitudinal tyre force is approximately independent of the vertical tyre load and can thus be modelled with only one curve. This curve can be defined by only three parameters, the normalized slip stiffness $K_{norm}$, the peak friction coefficient $\mu_{peak}$ and the friction coefficient at total sliding $\mu_{slide}$. In case of the lateral tyre force, these relations are more complex, because the cornering stiffness (lateral slip stiffness) is a non-linear function of the vertical load. The normalized lateral tyre force can, therefore, not be defined with only one shape and thus needs more input parameters and mathematical equations to describe its dependency on lateral slip $\alpha_{ij}$ and vertical load $F_{ij,z}$, see Ploeg et al. [PK00].

The lateral tyre force $F_{ij,lat}$ does not strike in the center of the contact patch, but has a point of application at a certain distance, called the pneumatic trail $t_{ij}$, behind the geometric middle of the contact patch. This phenomenon causes a self aligning torque $M_{ij,z}$ about the wheel's vertical axis, which tries to reduce the generated slip angle. The self aligning torque $M_{ij,z}$ is a function of the pneumatic trail $t_{ij}$ and the lateral tyre force $F_{ij,lat}$. Due to the fact that the pneumatic trail is a decaying function of side slip and is strongly dependent on vertical load, again the Magic Formula is used to model the normalized pneumatic trail.

It should be noted that figure 3.5 only shows the pure longitudinal and pure lateral tyre characteristics. In case of combined cornering and braking manoeuvres, however, the total friction force is not equal to the vector addition of both the longitudinal and lateral forces. Fortunately, the Magic Formula also offers a solution for this combined situation in the form of a purely empirical method, which describes the effect of combined slip on both the longitudinal and lateral forces. Weighting functions $G$ are introduced, which, when multiplied with the original pure slip functions, produce the interactive effects of longitudinal slip $\kappa_{ij}$ on cornering force $F_{ij,lat}$ and of lateral slip $\alpha_{ij}$ on longitudinal force $F_{ij,long}$. Also for modelling the characteristics of the self aligning torque in the combined slip condition, an adapted approach is used. For more details, the reader is referred to Ploeg et al. [PK00] and Van der Knaap et al. [KP00].

The rolling resistance of tyres results in dissipation of energy in the tyre, due to the continuous deformations near the contact zone. At low and medium velocities, the rolling resistance is approximately constant and is a direct result of the damping in the tyre, especially the damping of the thread compound. Also the tyre air pressure is of influence. From experiments, it is known that the rolling resistance force $F_{ij,r}$ is proportional to the vertical force $F_{ij,z}$:

$$F_{ij,r} = f_r F_{ij,z}, \tag{3.11}$$

where $f_r$ denotes the constant rolling resistance coefficient. The total wheel load, called the wheel load torque $T_{ij,w}$, is constituted from the rolling resistance and the longitudinal tyre force, according to:

$$T_{ij,w} = R_l f_r F_{ij,z} \text{sign}(\omega_{ij}) + R_l F_{ij,long}, \tag{3.12}$$

with $R_l$ being the loaded tyre radius. The wheel load torque plays a role in the wheel model, see section 3.5.

## 3.5 Electrical Drive Line Model

As already mentioned in subsection 2.3.1, the AC servo motor is one of the main components of the electrical drive line. An elaborate description on the theoretical backgrounds of this electrical machine can be found in Ploeg et al. [PK03a]. Here, only the most important results will be summarized.

One of the main parameters of interest is the drive output torque $T_{ij,drv}$. This parameter can be derived from the power balance. Consider for this purpose the mechanical power $P_{ij,m}$:

$$P_{ij,m} = T_{ij,drv}\omega_{ij,drv}, \tag{3.13}$$

where $\omega_{ij,drv}$ denotes the angular velocity of the outgoing motor shaft. Furthermore, the electrical power $P_{ij,e}$ is given by:

$$P_{ij,e} = (U_{ij} - U_{ij,EMF})\, I_{ij}. \tag{3.14}$$

Here, $P_{ij,e}$ corresponds to the amount of 'electrical' heat generated in the drive, i.e. heat caused by the current $I_{ij}$. Moreover, $U_{ij,EMF}$ is the back EMF (electro magnetic force), i.e. the rotor voltage due to the magnetic flux $\varphi$ from the stator, acting against the supply voltage $U_{ij}$. The back EMF can be calculated from:

$$U_{ij,EMF} = K_{mot,drv}(\varphi)\omega_{ij,drv}, \tag{3.15}$$

where $K_{mot,drv}$ is the motor constant or torque constant, which is actually a function of the magnetic flux $\varphi$. The power $P_{ij}$ supplied to the drive, for instance through the battery package, equals:

$$P_{ij} = U_{ij} I_{ij}. \tag{3.16}$$

Neglecting any mechanical friction, the power $P_{ij}$ is partly converted to mechanical power and partly results in heat generation. The power balance of the drive, therefore, reads:

$$P_{ij} = P_{ij,m} + P_{ij,e}. \tag{3.17}$$

Substitution of (3.13), (3.14) and (3.16) into (3.17) leads to:

$$U_{ij} I_{ij} = T_{ij,drv} \omega_{ij,drv} + (U_{ij} - U_{ij,EMF})\, I_{ij}. \tag{3.18}$$

Finally, after substitution of (3.15) into (3.18), an expression for the drive output torque $T_{ij,drv}$ is obtained:

$$T_{ij,drv} = K_{mot,drv}(\varphi) I_{ij}. \tag{3.19}$$

In general, an AC drive includes an application specific current control loop. Assuming that this loop consists of a PI-controller and by making use of an angular velocity feedforward loop, it is possible to compensate for angular velocity variations to a large extent. The resulting transfer function $I_{ij,ref} \rightarrow I_{ij}$ reduces to a second order system, with a left half plane zero, see Ploeg et al. [PK03a]. Referring to (3.19), it can be remarked that the current control loop in fact is a torque controller. Therefore, it is assumed that the AC drive is equipped with a torque controller instead of a current controller. The main reason for this assumption is that torque control is more convenient, since it corresponds to the actual application of the AC servo motor in the Moving Base. Based on the above results, the dynamic behaviour of a torque controlled AC servo motor can be described as:

$$T_{ij,drv} = H_{drv}(s) T_{ij,drv,ref}, \tag{3.20}$$

where $T_{ij,drv,ref}$ is the reference value for the drive output torque $T_{ij,drv}$ and $H_{drv}(s)$ is the transfer function. From the above, it follows that $H_{drv}(s)$ can be a second order dynamic transfer function with a left half plane zero. Taking into account the actual AC servo motor specifications, however, it can be concluded that a first order transfer function might do just as well. As a result, the following first order transfer function is used:

$$T_{ij,drv} = \frac{1}{\tau_e s + 1} T_{ij,drv,ref}, \tag{3.21}$$

where $\tau_e = \frac{L}{R}$ is the electrical time constant of the drive, with $L$ being the winding inductance and $R$ the winding resistance.

In order to implement a realistic behaviour of the AC servo motor, (3.21) needs to be extended with torque limits. These limits are essentially originating in the fact that the current $I_{ij}$ is bounded by a maximum allowable current $I_{ij,max}$, in order to prevent from burn out. For more details, the reader is referred to Ploeg et al. [PK03a].

The second main component of the electrical drive line is the planetary gear set. The ingoing shaft of this planetary gear set is connected to the AC servo motor shaft, while the outgoing shaft is connected to the wheel. A model for this planetary gear set is provided by a simple static gearbox, according to the following set of equations:

$$\begin{aligned} n_{in} &= i_g n_{out} \\ T_{out} &= i_g T_{in} - T_c(n_{out}), \end{aligned} \tag{3.22}$$

where $T_{out}$ and $n_{out}$ are the torque and velocity at the output shaft and $T_{in}$ and $n_{in}$ the torque and velocity at the input shaft. Furthermore, $i_g$ denotes the transmission ratio and $T_c(n_{out})$ is

the Coulomb friction as a function of the output shaft velocity. Hence, the gearbox friction is allocated entirely to the output shaft. Notice that the input parameters are the velocity at the output shaft $n_{out}$ and the torque at the input shaft $T_{in}$. In this case, these parameters correspond to the wheel angular velocity $\omega_{ij}$ and the drive output torque $T_{ij,drv}$, respectively. The output parameters consist of $n_{in}$ and $T_{out}$, which correspond to the angular velocity of the outgoing motor shaft $\omega_{ij,drv}$ and the driving torque $T_{ij,d}$, respectively.

Next, it is possible to consider the third main component, which is the wheel. The wheel inertia model, see Ploeg et al. [PK03b], essentially describes the rotational inertia of the wheel and is required to couple the AC servo motor model to the tyre model. In general, a number of torques are acting on the wheel, being the driving torque $T_{ij,d}$, the brake torque $T_{ij,br}$ and the so called wheel load torque $T_{ij,w}$. The latter is specified in (3.12). It should be remarked that the brake torque $T_{ij,br}$, induced by the brakes, is normally set to zero. Introducing a wheel inertia $J_w$, the following equation of motion is obtained for the wheel:

$$J_w\dot{\omega}_{ij} = T_{ij,d} - T_{ij,br} - T_{ij,w}, \tag{3.23}$$

where $\omega_{ij}$ is the wheel angular velocity.

## 3.6 Electrical Steering System Model

The construction of the electrical steering system is similar to that of the electrical drive line. Again, an AC servo motor is used, with its outgoing motor shaft being coupled to the input shaft of a planetary gear set. This planetary gear set accomplishes a reduction in angular velocity and its output shaft is coupled to the wheel suspension.

For this reason, the modelling of the AC servo motor and the planetary gear set is chosen identical to the corresponding models for the electrical drive line, see section 3.5. Notice that the subscript *drv* changes into *str*. The difference between both electrical drives is found in the component being connected to the output shaft of the planetary gear set. For the electrical drive line, this is the wheel, whereas for the electrical steering system, this is the wheel suspension. With this conclusion, it is not possible to copy the wheel inertia model from section 3.5.

In order to determine the steer angular velocity $\dot{\delta}_{ij}$ and, by integration, the steer angle $\delta_{ij}$, it is necessary to perform an analysis of the torques acting on the wheel suspension. The gearbox provides a steering torque $T_{ij,s}$ at its output shaft, which drives the suspension. Furthermore, the self aligning torque $M_{ij,z}$, generated in the contact patch between tyre and road, acts on the wheel suspension as well. The summation of both torques acts on the steering inertia $J_{st}$, leading to the following equation of motion:

$$J_{st}\ddot{\delta}_{ij} = T_{ij,s} + M_{ij,z}, \tag{3.24}$$

where $\ddot{\delta}_{ij}$ is the steer angular acceleration. The summation of both torques in (3.24) is due to the definition of the self aligning torque $M_{ij,z}$, see figure 3.3.

# Chapter 4

# Control Structure

## 4.1 Introduction

The Moving Base, like any other AGV, has to drive from its current position to a designated position along a desired trajectory. This trajectory, which can be expressed in terms of a generalized reference position $s_{ref}$ as a function of time $t$, is generated from within the VEHIL experiment controller, see Verburg et al. [VKP02]. Basically, the reference trajectory arises from the relative motion of two vehicles with respect to each other. It is generated using dynamic vehicle models and the state of the VUT itself.

In order to realize the reference trajectory, the control system acts on the four reference torques $T_{ij,drv,ref}$ of the electrical drive lines and the four reference torques $T_{ij,str,ref}$ of the electrical steering systems. The fact that there are three control objectives, being the $x$- and $y$-position and the yaw angle $\psi$, opposite to eight actuating system inputs, implies that the Moving Base is an over-actuated system. As a consequence, the control strategy is not straightforward and a dedicated approach needs to be followed.

A solution for the control problem is obtained by application of a so called master-slave control structure. This control design strategy will be investigated in section 4.2. Subsequently, the slave controller, referred to as motion control, is discussed in section 4.3. The master controller, referred to as tracking control, is considered in section 4.4. Finally, the so called motion observer is highlighted in section 4.5.

## 4.2 Control Design Strategy

As already mentioned, the Moving Base has to drive from its current position to a designated position along a desired trajectory. This reference trajectory can be expressed in terms of a generalized reference position $s_{ref}$ as a function of time $t$:

$$s_{ref}(t) = [x_{ref}(t), y_{ref}(t), \psi_{ref}(t)]^T . \tag{4.1}$$

In order to realize the reference trajectory, a control system has been designed. The control solution is obtained by considering the Moving Base as a mass, which has a 'virtual actuator' in its center of gravity. Using this approach, the control problem is actually split into two separate problems. The master controller forces the mass to traverse the desired trajectory, using the virtual actuator. Subsequently, the slave controller controls the eight actuators in such a way that they behave as one actuator in the center of gravity. This control strategy is illustrated in figure 4.1.

In this figure, the controller which realizes the reference trajectory is called 'Tracking'. This controller generates three outputs $\overline{u} = [u_1, u_2, u_3]^T$, which serve as inputs for the virtual actuator. The meaning of the input $\overline{u}$ is determined by the virtual actuator, which controls the actual

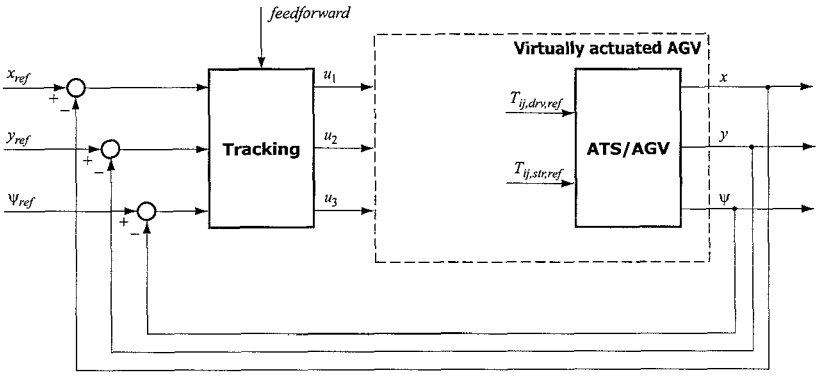


Figure 4.1: Moving Base control design strategy based on the application of a virtual actuator.

Moving Base by means of the reference driving torques $T_{ij,drv,ref}$ and the reference steering torques $T_{ij,str,ref}$.

In general, the virtual actuator can be designed from two different perspectives: force actuation and motion actuation. A third possibility is given by the combination of both concepts.

In case of force actuation, the virtual actuator coordinates the forces, generated by the tyres, in such a way that the resultant in the center of gravity of the Moving Base equals a specific desired value. This desired value is determined by the tracking controller, which provides a generalized force vector for this reason:

$$\overline{u} = \begin{bmatrix} u_1 \\ u_2 \\ u_3 \end{bmatrix} = \begin{bmatrix} F_{x,ref} \\ F_{y,ref} \\ M_{z,ref} \end{bmatrix} = F_{ref}. \tag{4.2}$$

The choice of these components is initiated by the fact that the tracking controller must realize an $x$-position, a $y$-position and a yaw angle $\psi$. This can be done relatively easy in case the controller is allowed to generate a desired force in $x$-direction and $y$-direction, respectively, as well as a desired torque in $z$-direction. The forces, generated in the contact patch between tyre and road, consist of a force $F_{ij,x}$ in $x$-direction and a force $F_{ij,y}$ in $y$-direction, see the left figure in figure 4.2. It is possible to influence the traction forces $F_{ij,x}$ and $F_{ij,y}$ by means of the reference driving torques $T_{ij,drv,ref}$ and the reference steer angles $\delta_{ij,ref}$, where the electrical steering systems are provided with a local steer angle control loop. For this reason, the force actuator has to compute eight inputs in order to realize three force components, see (4.2). This implies the presence of an over-actuated system, ultimately leading to the iterative solution of a complex system of eight algebraic equations, see Ploeg [Plo03b].

In case the virtual actuator is designed as a motion actuator, it has to realize a desired motion of the center of gravity, which is determined by the tracking controller. For this reason, the tracking controller output is a desired generalized velocity:

$$\overline{u} = \begin{bmatrix} u_1 \\ u_2 \\ u_3 \end{bmatrix} = \begin{bmatrix} \dot{x}_{ref} \\ \dot{y}_{ref} \\ \dot{\psi}_{ref} \end{bmatrix} = \dot{s}_{ref}. \tag{4.3}$$

Next, the virtual actuator can be designed based on a vehicle motion analysis. First, the desired motions of the steering points of the vehicle are computed, based on the desired motion of the center of gravity. These desired motions can be expressed as velocity vectors $\overline{v}_{ij,ref}$, with components in $x$- and $y$-direction: $\overline{v}_{ij,ref} = [v_{ij,x,ref}, v_{ij,y,ref}]^T$. This approach is illustrated in the right figure in figure 4.2. The desired steering point velocities $\overline{v}_{ij,ref}$ are now used to control the electrical drive lines, which are equipped with local velocity control loops. Hereby, the longitudinal tyre slip is actually neglected. In case the lateral tyre slip is neglected as well, the desired steer

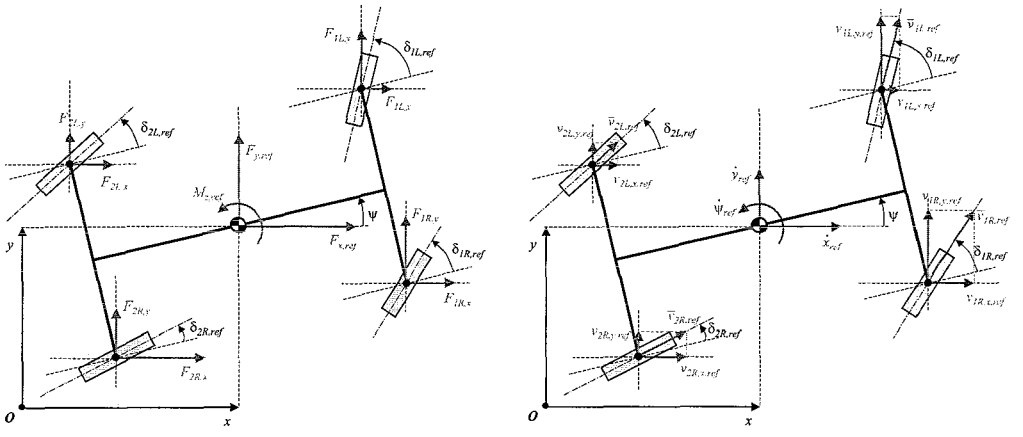

Figure 4.2: *Left*: Virtual force actuator; *Right*: Virtual motion actuator.

angles $\delta_{ij,ref}$ can be determined from the orientation of $\overline{v}_{ij,ref}$, see the right figure in figure 4.2. Subsequently, these reference steer angles are the inputs of local steer angle control loops of the electrical steering systems. This approach of the virtual actuator appears to be relatively simple, as a result of neglecting the longitudinal and lateral tyre slip. However, during high dynamic operations of the Moving Base, tyre slip is of crucial importance for the behaviour of the vehicle. For this reason, a different approach is followed.

A third alternative for the virtual actuator can be found by starting from the statement that the vehicle motion is caused by the forces and torques acting on it. The role of the steering system merely is to employ the traction forces in an effective way. A direct consequence of this approach is that the determination of the steer angles and the required driving torques can take place independent of each other. This leads to a simplification of the force actuator, because now there are only four unknowns instead of eight. These unknown reference driving torques $T_{ij,drv,ref}$ can be computed according to a linear system of four equations, as will be shown in section 4.3. The steer angles are determined according to the motion actuator. Independent of the forces acting on the Moving Base, the steer angles are determined on the base of the directions of the velocities in the steering points. Notice that in this case the outputs of the tracking controller $\overline{u}$ are chosen identical to (4.3). Therefore, the determination of the reference steer angles entirely corresponds to the motion actuator. The translation of the desired motion $\dot{s}_{ref}$ to the desired generalized force $F_{ref}$, which is required for the force actuator, can take place by construction of a controller for the vehicle velocity $\dot{s}$, which intervenes on the desired generalized force $F_{ref}$. The resulting control structure is depicted in figure 4.3. In this figure, the virtual actuator is called motion control, due to the fact that the inputs are the desired motions. Notice that the motion controller is depicted in a simplified way, by leaving out the necessary feedback loops.

## 4.3 Motion Control

As already mentioned in section 4.2, the motion control needs to realize a desired value of the generalized velocity, given by:

$$\dot{s}_{ref}(t) = \left[\dot{x}_{ref}(t), \dot{y}_{ref}(t), \dot{\psi}_{ref}(t)\right]^T. \tag{4.4}$$

In order to achieve this, four electrical drive lines and four electrical steering systems are available. This implies that the Moving Base is an over-actuated system, in this case leading to five additional degrees of freedom, which can be used to realize additional control objectives. These degrees of freedom will be used primarily to minimize tyre slip, as will be discussed later on. Notice that this

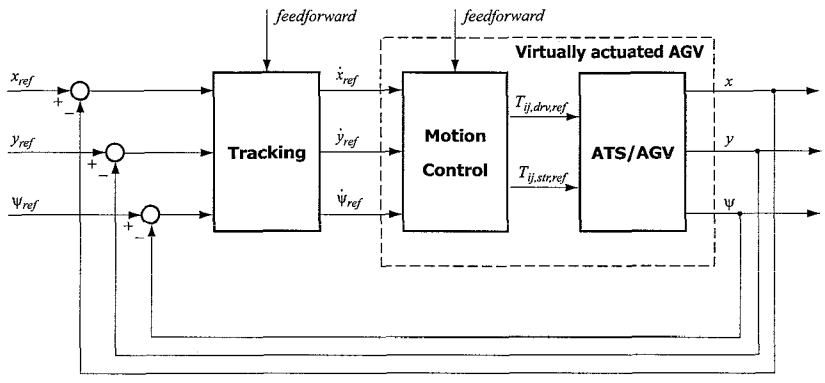


Figure 4.3: Moving Base control design strategy.

leads to little energy dissipation and, furthermore, the non-linear part of the tyre characteristics is avoided as much as possible.

To obtain an efficient and clear description of the motion controller, the first two elements of the generalized velocity $\dot{s}$, which are based on a Cartesian coordinate reference system, are converted into longitudinal and lateral velocity components:

$$\begin{aligned} v_{long} &= \dot{x}\cos\psi + \dot{y}\sin\psi \\ v_{lat} &= -\dot{x}\sin\psi + \dot{y}\cos\psi. \end{aligned} \tag{4.5}$$

This leads to a new generalized velocity vector, represented by:

$$\dot{p}(t) = \left[v_{long}(t), v_{lat}(t), \dot{\psi}(t)\right]^T. \tag{4.6}$$

In accordance with section 4.2, a desired generalized velocity $\dot{p}_{ref}$ will be realized by taking as a starting point that the velocity of the vehicle is influenced by force actuation, using the driving torques $T_{ij,drv}$. The motion actuation influences the direction of the vehicle, by controlling the steer angles $\delta_{ij}$. As a result of the fact that the electrical steering systems are torque controlled, it is necessary to implement local steer angle control loops, with inputs $\delta_{ij,ref}$ and outputs $T_{ij,str,ref}$. In subsection 4.3.1, the force actuation in the shape of velocity control will be discussed. Subsequently, the motion actuation in the shape of direction control is considered in subsection 4.3.2.

### 4.3.1 Velocity Control

The velocity components in (4.6) can be influenced by the resulting force components and the resulting torque component in the center of gravity of the vehicle, being the virtual actuator. According to the control strategy in section 4.2, the motion control needs to generate a desired generalized force $F_{ref}$, based on the desired velocity $\dot{p}_{ref}$ from the tracking controller, after which $F_{ref}$ is converted into reference driving torques $T_{ij,drv,ref}$. This can take place by application of a feedback loop, in addition with feedforward.

#### Feedback

The forces acting on the vehicle are depicted in figure 4.4, where the traction forces act in longitudinal direction, related to the tyres. These traction forces $F_{ij}$ are a direct consequence of the driving torques $T_{ij,drv}$, related to the motor shaft:

$$F_{ij} = \frac{T_{ij,drv} i_g - J_{w,eff}\dot{\omega}_{ij}}{R_l}, \tag{4.7}$$

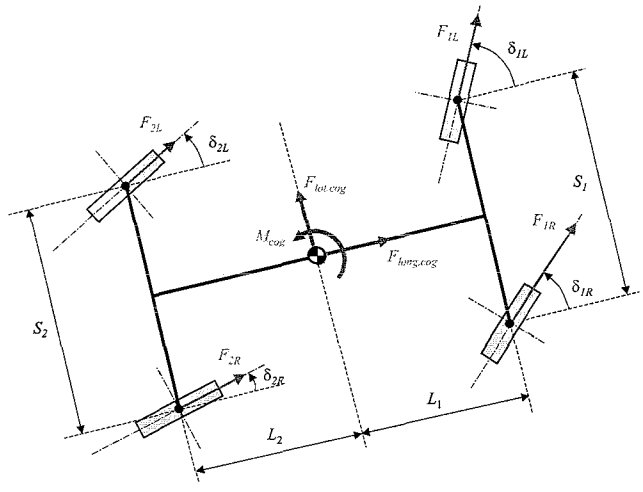


Figure 4.4: Driving forces and resulting forces and torque in center of gravity.

where $J_{w,eff}$ is the effective mass moment of inertia, related to the gearbox output shaft, $\dot{\omega}_{ij}$ the wheel angular acceleration, $i_g$ the transmission ratio and $R_l$ the loaded tyre radius.

With respect to the left figure in figure 4.2, the forces are defined with respect to the vehicle coordinate reference system, instead of using the Cartesian coordinate reference system. The main reason for this change is that this choice allows a more efficient description of the feedback loop.

Based on the forces $F_{ij}$, it is possible to compute a longitudinal force $F_{long,cog}$, a lateral force $F_{lat,cog}$ and a torque $M_{cog}$ in the center of gravity, by making use of:

$$F_{long,cog} = F_{1L}\cos\delta_{1L} + F_{1R}\cos\delta_{1R} + F_{2L}\cos\delta_{2L} + F_{2R}\cos\delta_{2R} \tag{4.8}$$

$$F_{lat,cog} = F_{1L}\sin\delta_{1L} + F_{1R}\sin\delta_{1R} + F_{2L}\sin\delta_{2L} + F_{2R}\sin\delta_{2R} \tag{4.9}$$

$$\begin{aligned} M_{cog} = {} & F_{1L}\left(-\frac{S_1}{2}\cos\delta_{1L} + L_1\sin\delta_{1L}\right) + F_{1R}\left(\frac{S_1}{2}\cos\delta_{1R} + L_1\sin\delta_{1R}\right) + \\ & F_{2L}\left(-\frac{S_2}{2}\cos\delta_{2L} - L_2\sin\delta_{2L}\right) + F_{2R}\left(\frac{S_2}{2}\cos\delta_{2R} - L_2\sin\delta_{2R}\right). \end{aligned} \tag{4.10}$$

In behalf of control, it is necessary to determine the forces $F_{ij}$ and, consequently, the driving torques $T_{ij,drv}$, as a function of $F_{long,cog}$, $F_{lat,cog}$ and $M_{cog}$. Besides (4.8) – (4.10), an additional equation is required. Because it is desired to minimize tyre slip, an equation is introduced, which indicates that the distribution of the driving torques among the vehicle's front and rear axle corresponds to the distribution of the current vertical wheel loads. This results into a condition with respect to the longitudinal weight transfer:

$$\frac{F_{1L} + F_{1R}}{F_{1L,z} + F_{1R,z}} = \frac{F_{2L} + F_{2R}}{F_{2L,z} + F_{2R,z}}. \tag{4.11}$$

Actually, only the absolute values of the forces $F_{ij}$ are of importance. Assuming that the forces $F_{ij}$ are positive, the absolute value signs are left out in (4.11). However, in Ploeg [Plo03b], it is shown that two additional equations with respect to weight transfer are required, to avoid singularities. This results into an equation with respect to the lateral weight transfer:

$$\frac{F_{1L} + F_{2L}}{F_{1L,z} + F_{2L,z}} = \frac{F_{1R} + F_{2R}}{F_{1R,z} + F_{2R,z}} \tag{4.12}$$

and an equation with respect to the diagonal weight transfer:

$$\frac{F_{1L} + F_{2R}}{F_{1L,z} + F_{2R,z}} = \frac{F_{1R} + F_{2L}}{F_{1R,z} + F_{2L,z}}. \tag{4.13}$$

Starting from (4.8) – (4.10) and the weight transfer requirements (4.11) – (4.13), the forces $F_{ij}$ can be determined. For this reason, the following matrix equation is constructed:

$$\begin{bmatrix} F_{long,cog} \\ F_{lat,cog} \\ M_{cog} \\ 0 \\ 0 \\ 0 \end{bmatrix} = \begin{bmatrix} \cos\delta_{1L} & \cos\delta_{1R} \\ \sin\delta_{1L} & \sin\delta_{1R} \\ -\frac{S_1}{2}\cos\delta_{1L} + L_1\sin\delta_{1L} & \frac{S_1}{2}\cos\delta_{1R} + L_1\sin\delta_{1R} \\ F_{2L,z} + F_{2R,z} & F_{2L,z} + F_{2R,z} \\ F_{1R,z} + F_{2R,z} & -(F_{1L,z} + F_{2L,z}) \\ F_{1R,z} + F_{2L,z} & -(F_{1L,z} + F_{2R,z}) \end{bmatrix} \begin{bmatrix} \cos\delta_{2L} & \cos\delta_{2R} \\ \sin\delta_{2L} & \sin\delta_{2R} \\ -\frac{S_2}{2}\cos\delta_{2L} - L_2\sin\delta_{2L} & \frac{S_2}{2}\cos\delta_{2R} - L_2\sin\delta_{2R} \\ -(F_{1L,z} + F_{1R,z}) & -(F_{1L,z} + F_{1R,z}) \\ F_{1R,z} + F_{2R,z} & -(F_{1L,z} + F_{2L,z}) \\ -(F_{1L,z} + F_{2R,z}) & F_{1R,z} + F_{2L,z} \end{bmatrix} \begin{bmatrix} F_{1L} \\ F_{1R} \\ F_{2L} \\ F_{2R} \end{bmatrix}, \quad (4.14)$$

which can also be written as $\overline{u} = K_m\overline{f}$, where $\overline{u}$ represents the modified output of the tracking controller. In Ploeg [Plo03b], it is shown that the matrix $K_m$ has a rank which is always equal to or larger than four. Therefore, no exact solution $\overline{f}$ of (4.14) will exist in general and a least squares solution is constructed. For this reason, an error vector $\overline{\varepsilon}$ is introduced, leading to $\overline{u} = K_m\overline{f} + \overline{\varepsilon}$. Now, the objective is to determine $\overline{f}$ in such a way that the quadratic error $J = \overline{\varepsilon}^T\overline{\varepsilon}$ is minimized. The solution of this least squares problem equals:

$$\overline{f} = \left(K_m^T K_m\right)^{-1} K_m^T \overline{u}, \quad (4.15)$$

see Gelb et al. [GKN+99]. However, the least squares solution according to (4.15) does not distinguish between weight transfer conditions, which have to be minimized and the force and torque balance, which are constraints. As a result, the force and torque balance will in general not be satisfied exactly. In order to improve this, weighting factors are introduced. In this way, it is possible to obtain a least squares solution, which violates the force and torque balance with only a small error. To achieve this, a diagonal weighting matrix $W$ is introduced, leading to the criterion $J = \overline{\varepsilon}^T W\overline{\varepsilon}$. Consequently, the least squares solution equals:

$$\overline{f} = \left(K_m^T W K_m\right)^{-1} K_m^T W\overline{u}. \quad (4.16)$$

By assigning large values to the first three diagonal elements in $W$, compared to the last three elements, a solution is obtained which approximates the equations (4.8) – (4.10) quite well, at the expense of the weight transfer requirements. Using (4.7), it is now possible to compute the reference driving torques. For the computation of the vertical loads $F_{ij,z}$, the reader is referred to Ploeg [Plo03b].

The equations presented above make it possible to translate desired forces $F_{long,cog}$ and $F_{lat,cog}$ and a desired torque $M_{cog}$ in the center of gravity into driving torques. Next, it is necessary to determine certain values for $F_{long,cog}$, $F_{lat,cog}$ and $M_{cog}$. This is accomplished by a velocity controller, which is based on feedback of $v_{long}$, $v_{lat}$ and $\dot{\psi}$, extended with feedforward. Use is made of three independent PID controllers, because the velocities $v_{long}$, $v_{lat}$ and $\dot{\psi}$ can be influenced by $F_{long,cog}$, $F_{lat,cog}$ and $M_{cog}$, respectively.

### Feedforward

Taking into account the mass of the Moving Base, the required forces $F_{long,cog,ff}$ and $F_{lat,cog,ff}$ in the center of gravity can be determined, using the reference accelerations $\dot{v}_{long,ref}$ and $\dot{v}_{lat,ref}$, respectively:

$$\begin{aligned} F_{long,cog,ff} &= m\dot{v}_{long,ref} \\ F_{lat,cog,ff} &= m\dot{v}_{lat,ref}. \end{aligned} \quad (4.17)$$

The total desired forces in the center of gravity of the Moving Base can now be determined by adding the feedforward signals in (4.17) to the respective control outputs.

A similar feedforward signal is obtained by computing the required torque $M_{cog,ff}$, using the reference yaw acceleration $\ddot{\psi}_{ref}$:

$$M_{cog,ff} = I_z \ddot{\psi}_{ref}, \tag{4.18}$$

where $I_z$ is the mass moment of inertia of the Moving Base in vertical direction with respect to the center of gravity. The total desired torque in the center of gravity of the vehicle can now be determined by adding $M_{cog,ff}$ to the controller output.

### 4.3.2 Direction Control

In Ploeg [Plo03b], several different concepts for direction control, which influences the direction of motion by adjusting the steer angles $\delta_{ij}$, are proposed. In contrast to the motion actuator, discussed in section 4.2, these concepts take lateral tyre slip into account. However, due to interaction, this results into a badly damped system. For this reason, the direction controller is designed according to the previously discussed motion actuator. Hence, the direction controller actually is a steer angle controller.

Implementation of the steer angle controller requires the computation of the reference steer angles $\delta_{ij,ref}$. In order to perform this computation, the desired motions of the steering points of the Moving Base are calculated, based on the desired motion of the center of gravity. The motions of the steering points can be expressed as velocity vectors $\overline{v}_{ij}$, with components in longitudinal and lateral direction: $\overline{v}_{ij} = [v_{ij,long}, v_{ij,lat}]^T$. This is illustrated in figure 4.5.

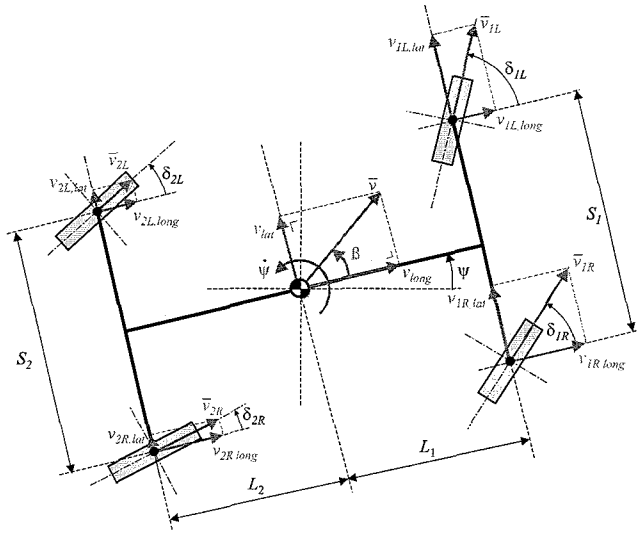


Figure 4.5: Velocity components in steering points and center of gravity.

The relation between steering point motion and center of gravity motion is now given by:

$$\begin{bmatrix} v_{1L,long} \\ v_{1L,lat} \\ v_{1R,long} \\ v_{1R,lat} \\ v_{2L,long} \\ v_{2L,lat} \\ v_{2R,long} \\ v_{2R,lat} \end{bmatrix} = \begin{bmatrix} 1 & 0 & -\frac{S_1}{2} \\ 0 & 1 & L_1 \\ 1 & 0 & \frac{S_1}{2} \\ 0 & 1 & L_1 \\ 1 & 0 & -\frac{S_2}{2} \\ 0 & 1 & -L_2 \\ 1 & 0 & \frac{S_2}{2} \\ 0 & 1 & -L_2 \end{bmatrix} \begin{bmatrix} v_{long} \\ v_{lat} \\ \dot{\psi} \end{bmatrix}, \tag{4.19}$$

where use is made of the chassis geometry of the Moving Base. Notice that the terms *longitudinal* and *lateral* are related to the orientation of the chassis and not to the orientation of the wheel plane. With (4.19), the velocity components of the four steering points are available. The direction of the velocity in a steering point, which in this case equals the reference steer angle, is given by:

$$\delta_{ij,ref} = \arctan\left(\frac{v_{ij,lat}}{v_{ij,long}}\right). \tag{4.20}$$

Summarizing, it can be stated that (4.19) and (4.20) define the exact relation between center of gravity motion and reference steer angles. These reference steer angles are realized by four identical steer angle controllers, which generate the reference steering torques $T_{ij,str,ref}$. With this conclusion, the design of the direction controller is completed.

Next, it is possible to combine both controllers, resulting in the motion controller. The block diagram of the motion controller is depicted in figure 4.6, where the velocity controller from subsection 4.3.1 and the direction controller from this subsection can be clearly distinguished.

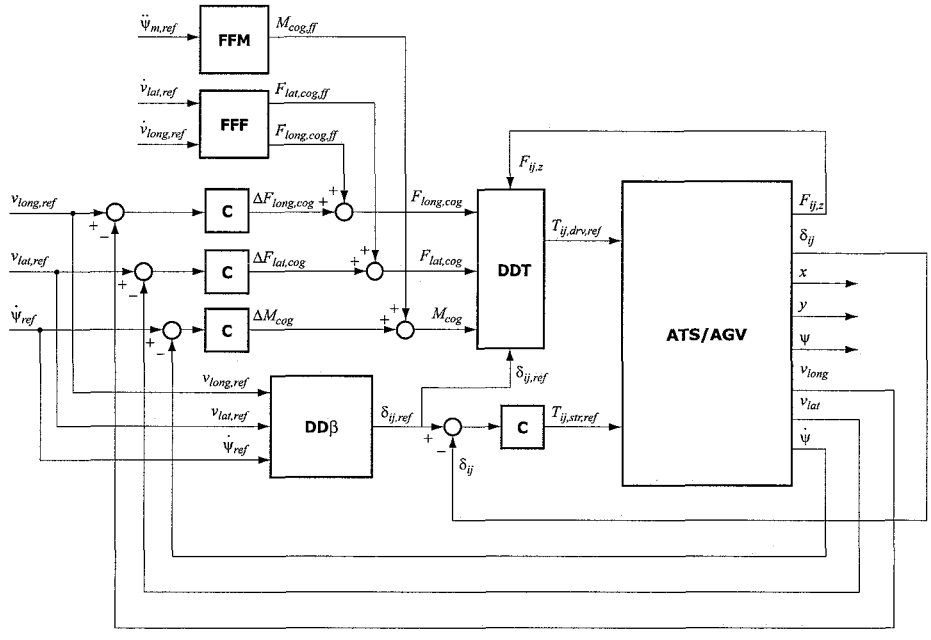


Figure 4.6: Motion Control block diagram consisting of velocity control and direction control.

## 4.4 Tracking Control

The motion controller, designed in the previous section, coordinates the eight available actuators in such a way that they behave as one virtual actuator, acting in the center of gravity. Furthermore, the feedback loops in the motion controller impose a linearizing effect. As a result, the tracking controller has a relatively simple structure, as will be shown in this section.

The task of the tracking controller is to realize a certain desired generalized position $s_{ref}(t)$, see (4.1), by intervening on the desired velocity $\dot{s}_{ref}(t)$ of the 'virtually actuated' Moving Base, see (4.4). Due to this choice for the inputs of the motion control, an (approximately) uncoupled system arises from the perspective of the tracking control. This implies the possibility for the tracking control to consist of three independent controllers, for instance simple PIDs, leading to the block diagram in figure 4.7.

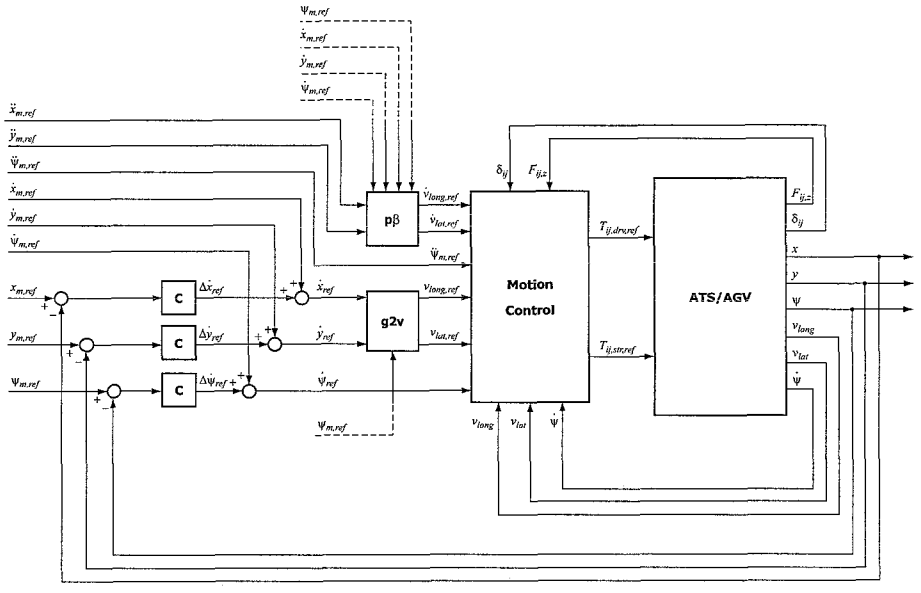


Figure 4.7: Tracking Control block diagram.

From the block diagram, it can be concluded that extensive use is made of feedforward. Notice that this is possible because the first time derivative $v_{ref}$ and the second time derivative $a_{ref}$ of the generalized reference position $s_{ref}$ are known, see Verburg et al. [VKP02]. Acceleration feedforward is required for the motion control. Besides the reference yaw acceleration $\ddot{\psi}_{ref}$, the longitudinal and lateral reference accelerations, denoted by $\dot{v}_{long,ref}$ and $\dot{v}_{lat,ref}$, respectively, are required. The latter two accelerations are determined according to the relations:

$$\begin{aligned} \dot{v}_{long,ref} &= \ddot{x}_{ref}\cos\psi_{ref} + \ddot{y}_{ref}\sin\psi_{ref} - (\dot{x}_{ref}\sin\psi_{ref} - \dot{y}_{ref}\cos\psi_{ref})\,\dot{\psi}_{ref} \\ \dot{v}_{lat,ref} &= -\ddot{x}_{ref}\sin\psi_{ref} + \ddot{y}_{ref}\cos\psi_{ref} - (\dot{x}_{ref}\cos\psi_{ref} + \dot{y}_{ref}\sin\psi_{ref})\,\dot{\psi}_{ref}. \end{aligned} \tag{4.21}$$

Feedforward of the velocity vector $v_{ref}$ takes place by adding the reference velocities to the corresponding controller outputs, as indicated in figure 4.7.

## 4.5 Motion Observer

During the design of the tracking control and the motion control, it is assumed that the Moving Base position $s = [x, y, \psi]^T$ and velocity $\dot{p} = [v_{long}, v_{lat}, \dot{\psi}]^T$ are available. From subsection 2.4.1, it follows that the yaw velocity $\dot{\psi}$ is measured using a fiber optic gyro. Consequently, the yaw angle $\psi$ is obtained by integration. However, the remaining components of the velocity vector ($v_{long}$ and $v_{lat}$), as well as the position vector ($x$ and $y$), are not measured directly. There are two methods available for estimating these components. In subsection 4.5.1, a so called odometry based estimation method is discussed, which is sensitive to tyre slip. Subsequently, a discrete time optimal Kalman filter is considered in subsection 4.5.2.

### 4.5.1 Odometry Based

The odometry based motion observer makes use of the measured wheel angular velocities $\omega_{ij}$ and steer angles $\delta_{ij}$, in order to determine $v_{long}$ and $v_{lat}$. Consider (4.19) for this reason, which relates the velocity components in the center of gravity to the longitudinal and lateral velocity components in the four steering points of the Moving Base. These velocity components, $v_{ij,long}$

and $v_{ij,lat}$, are related to the longitudinal and lateral direction of the Moving Base, respectively. They can be projected onto the longitudinal and lateral axes of the wheel plane, as depicted in figure 4.8.

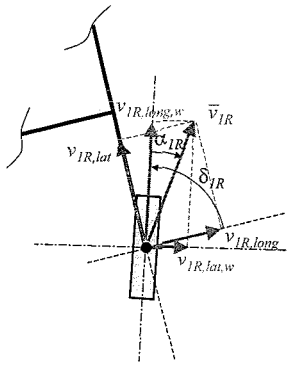


Figure 4.8: Definition of longitudinal and lateral velocity components, depicted in positive direction.

In order to do this, a $2 \times 2$ transformation matrix $\Delta_{ij}$ is introduced, see Ploeg [Plo03b]. The velocity components $v_{ij,long,w}$ and $v_{ij,lat,w}$, related to the wheel plane, are then given by:

$$\begin{bmatrix} v_{1L,long,w} \\ v_{1L,lat,w} \\ v_{1R,long,w} \\ v_{1R,lat,w} \\ v_{2L,long,w} \\ v_{2L,lat,w} \\ v_{2R,long,w} \\ v_{2R,lat,w} \end{bmatrix} = \begin{bmatrix} \Delta_{1L} \\ \Delta_{1R} \\ \Delta_{2L} \\ \Delta_{2R} \end{bmatrix} \begin{bmatrix} v_{long} \\ v_{lat} \end{bmatrix} + \begin{bmatrix} \Delta_{1L} & O_2 & O_2 & O_2 \\ O_2 & \Delta_{1R} & O_2 & O_2 \\ O_2 & O_2 & \Delta_{2L} & O_2 \\ O_2 & O_2 & O_2 & \Delta_{2R} \end{bmatrix} \begin{bmatrix} -\frac{S_1}{2} \\ L_1 \\ \frac{S_1}{2} \\ L_1 \\ -\frac{S_2}{2} \\ -L_2 \\ \frac{S_2}{2} \\ -L_2 \end{bmatrix} \dot{\psi}, \tag{4.22}$$

where $O_2$ is a $2 \times 2$ zero matrix. Relation (4.22) can also be written as $\overline{v}_w = \Delta_c \overline{v} + \Delta_d \bar{l} \dot{\psi}$. The objective of the estimator is to determine the vector $\overline{v}$, which can only be done approximately in case all matrices in (4.22) are of full rank. For this reason, an error vector $\bar{\varepsilon}$ is introduced and (4.22) is rewritten as $\overline{v}_w - \Delta_d \bar{l} \dot{\psi} = \Delta_c \overline{v} + \bar{\varepsilon}$. Minimizing the quadratic error $J = \bar{\varepsilon}^T W_v \bar{\varepsilon}$, where $W_v$ is a diagonal weighting matrix, leads to the least squares solution:

$$\widehat{\overline{v}} = \left(\Delta_c^T W_v \Delta_c\right)^{-1} \Delta_c^T W_v \left(\overline{v}_w - \Delta_d \bar{l} \dot{\psi}\right). \tag{4.23}$$

As a result of the fact that only the longitudinal velocities $v_{ij,long,w}$ are available, the weighting matrix $W_v$ is necessary to take the absence of the lateral velocities $v_{ij,lat,w}$ into account. After computation of $v_{long}$ and $v_{lat}$, these components can be transformed into $\dot{x}$ and $\dot{y}$, using a slightly modified version of (4.5). Integration subsequently leads to the position vector $s$.

### 4.5.2 Kalman Filter Based

Besides the odometry based motion observer, discussed above, also a Kalman filter based motion observer is available. This discrete time optimal Kalman filter is based on the general state space model:

$$\begin{aligned} x(k+1) &= Ax(k) + Bu(k) + w(k) \\ y(k) &= Cx(k) + v(k), \end{aligned} \tag{4.24}$$

where $A$, $B$ and $C$ denote the system matrix, input matrix and output matrix, respectively. Furthermore, $w(k)$ and $v(k)$ represent Gaussian process and measurement noise, respectively. The system state vector $x(k)$, the input vector $u(k)$ and the measurement vector $y(k)$ are given by:

$$\begin{aligned} x(k) &= [x, y, \dot{x}, \dot{y}]^T \\ u(k) &= [a_x, a_y]^T \\ y(k) &= [x_m, y_m, \dot{x}_{odo}, \dot{y}_{odo}]^T. \end{aligned} \tag{4.25}$$

The objective of the Kalman filter is to compute an optimal estimate of the state vector $x(k)$. This state vector consists of the Moving Base position coordinates $x$ and $y$, added with the Moving Base velocity components $\dot{x}$ and $\dot{y}$. From (4.25), it follows that the inputs of the system model are given by the measured accelerations in $x$- and $y$-direction. The measurement vector $y(k)$ incorporates $x_m$ and $y_m$. These are the Moving Base coordinates obtained from the magnet grid, in combination with the rulers. It should be noted that this measurement is not always available. The computation of $x_m$ and $y_m$, based on the ruler output signals, is rather difficult and of less importance in this report. Therefore, it will not be discussed. In addition to $x_m$ and $y_m$, the output vector $y(k)$ consists of $\dot{x}_{odo}$ and $\dot{y}_{odo}$. This is the odometric vehicle velocity, which is computed as discussed in subsection 4.5.1.

Using the signals described above, the discrete time optimal Kalman filter is able to calculate a state estimate at each time instant $k$. Transformation of $\dot{x}$ and $\dot{y}$ into $v_{long}$ and $v_{lat}$ is performed by (4.5). In case more information about the discrete time optimal Kalman filter is desired, the reader is referred to Gelb et al. [GKN+99].

# Chapter 5

# Model Validation and Improvement

## 5.1 Introduction

In chapter 3 and 4, the Moving Base simulation model and the control structure are discussed, respectively. Both the simulation model and the control system are a result of the design methodology that has been adopted during the Moving Base development process, see Ploeg et al. [PKV02]. Recall that another important feature of this design process is the application of test rig experiments, in order to validate component models and to test/tune local control loops.

During the Moving Base design process, specific test rig experiments were carried out for the electrical drives, their local current control loops and the selection of the battery cells, see Koopman [Koo02b]. The experimental results led to an iterative improvement of the mathematical model and, consequently, the control system. At this moment, both Moving Bases are fully operational. However, the overall performance evaluation, as well as the validation of the complete simulation model, has not yet been performed.

In order to validate and, depending on the results, improve the complete simulation model, new experiments are developed. These experiments are performed using the simulation model, as well as the real Moving Bases. Notice that use is made of an identical control system in both cases. After comparison of simulation and experimental results, it is possible to draw a conclusion about the validity of the simulation model and to improve the model if necessary. Depending on the experiment type, it is also possible to evaluate the performance of the Moving Base. It should be remarked that all experiments are performed using Moving Base I. Only during the flywheel experiments, Moving Base II is used as well.

The experiments can be divided into a number of different categories. In section 5.2, the handling behaviour of the Moving Base is evaluated. Experimental results concerning several friction measurements are discussed in section 5.3. Subsequently, section 5.4 contains results with respect to measurements, conducted to determine an inertia estimate. In section 5.5 and 5.6, experiments are discussed, in which use is made of motion control and tracking control, respectively. From the results in the aforementioned sections, it can be concluded that substantial differences between simulation and experimental results occur. In order to explain these differences, flywheel measurements are necessary, which are considered in section 5.7.

Notice that only the main results are highlighted in this chapter. In appendix B, section B.1, one can find short descriptions of all experiments. Furthermore, in section B.2 a list is presented, containing all data file names. Extended results concerning the different experiments can be found in Van der Meulen [Meu04].

## 5.2 Handling Behaviour

In order to investigate the handling behaviour of the Moving Base, a so called steady state circular test is performed, see Besselink [Bes03]. During the experiment, the Moving Base drives in a circle with fixed radius $R$, which in this case equals 7 m. The circle radius is maintained by using tracking control and motion control. Moreover, use is made of Kalman filter based position/velocity estimates. By increasing the forward reference velocity $v_{long,ref}$ very slowly, which may be considered steady state, the lateral acceleration in the center of gravity $a_{cog,lat}$ also increases. Setting the maximum longitudinal reference velocity equal to 7 m/s implies a maximum lateral acceleration of 7 m/s$^2$, according to $a_{cog,lat} = \frac{v_{long}^2}{R}$. Using the measured steer angles $\delta_{ij}$ and the lateral acceleration in the center of gravity $a_{cog,lat}$, it is possible to construct four handling diagrams. These are depicted in figure 5.1, for simulations as well as experiments.

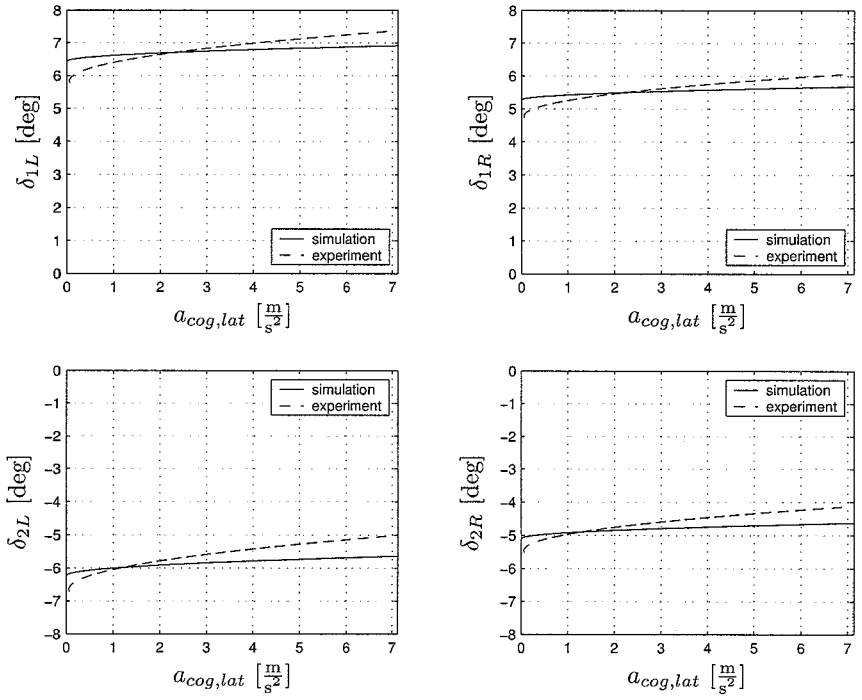


Figure 5.1: Handling diagrams for all four wheels obtained from fit procedures (solid: simulation; dashed: experiment).

From figure 5.1, it can be concluded that the Moving Base shows nearly neutral behaviour. According to the upper two figures, the steer angle slightly increases, which implies understeer behaviour. On the contrary, the lower two figures show a decreasing steer angle, which implies oversteer behaviour. However, these conclusions with respect to understeer and oversteer behaviour are no absolute truths, due to two reasons. The first reason is that the tracking controller just consists of P-control, which may lead to a constant (steady state) error in the yaw angle $\psi$. The second reason is that the fiber optic gyro incorporates a certain unknown offset, see subsection 2.4.1. Both effects result in an actual yaw angle of the Moving Base which does not equal the reference yaw angle, leading to a slight change in steer angles. Notice that the offset in the yaw angle measurement is only present in practice, which may be a possible explanation for the larger change in steer angles for the experiments compared to the simulations. Hence, a conclusion about the handling behaviour of the Moving Base, by making use of these specific results, is not very straightforward.

## 5.3 Friction Measurements

### 5.3.1 Driving Torques

The behaviour of driving torque $T_{ij,drv}$ as a function of wheel angular velocity $\omega_{ij}$ is investigated by conducting seven experiments. During each experiment, a constant longitudinal reference velocity is set, ranging from 1 to 7 m/s. This reference velocity is realized by the motion controller in combination with the Kalman filter. Using the obtained data leads to four characteristics, consisting of seven data points each. Averaging these four characteristics results in one characteristic, which is depicted in figure 5.2. Notice that the driving torque $T_{drv}$ in figure 5.2 is related to the transmission input shaft, while the wheel angular velocity is related to the transmission output shaft. The driving torque incorporates the torque loss in the transmission and the wheel load torque (rolling resistance only), see section 3.4. Air resistance plays a minor role.

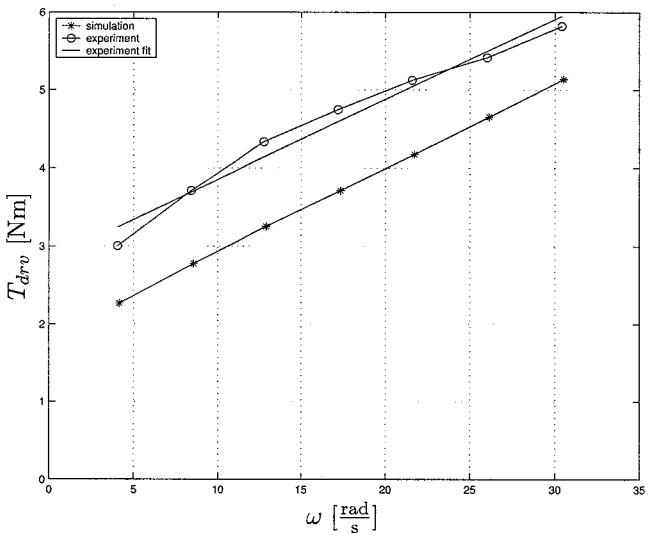


Figure 5.2: Average driving torque (related to input) as a function of wheel angular velocity (related to output) including first order fit (solid-star: simulation data; solid-circle: experimental data; solid: experimental data fit).

It can be seen from the simulation and the experimental results in figure 5.2 that both characteristics are approximately linear. For this reason, both characteristics are fit by first order polynomials. The following first order polynomial is obtained for the simulation data:

$$T_{drv} = 1.8 + 0.1\omega, \tag{5.1}$$

which is not depicted in figure 5.2 for clarity reasons. In addition, the fit for the experimental data is given by:

$$T_{drv} = 2.8 + 0.1\omega. \tag{5.2}$$

From (5.1) and (5.2), it can be concluded that the difference between the simulation and the experimental characteristic is constant and approximately equal to 1.0 Nm. The cause of this difference will be addressed in section 5.7.

### 5.3.2 Steering Torques

In the Moving Base simulation model, the electrical steering system gearbox model, see section 3.6, does not incorporate a friction torque as a function of steer angular velocity. For this reason, these

torque characteristics need to be determined. This is done by lifting the wheels of the Moving Base, in such a way that there is no contact between tyres and floor. Next, a series of different steer angular velocities is set for each electrical steering system. By measuring the required steering torques $T_{ij,str}$, it is possible to construct the desired characteristics. Because it appears that the behaviour is quite the same for all wheel units, the data points from all four characteristics can be used to obtain a first order fit. The resulting characteristic is depicted in figure 5.3 and can be applied in the simulation model. In addition, the corresponding mathematical expression is given by:

$$T_{str} = 0.30 + 5.1 \cdot 10^{-3}\dot{\delta}. \tag{5.3}$$

Notice that the steering torque $T_{str}$ is related to the transmission input, while the steer angular velocity $\dot{\delta}$ is related to the transmission output.

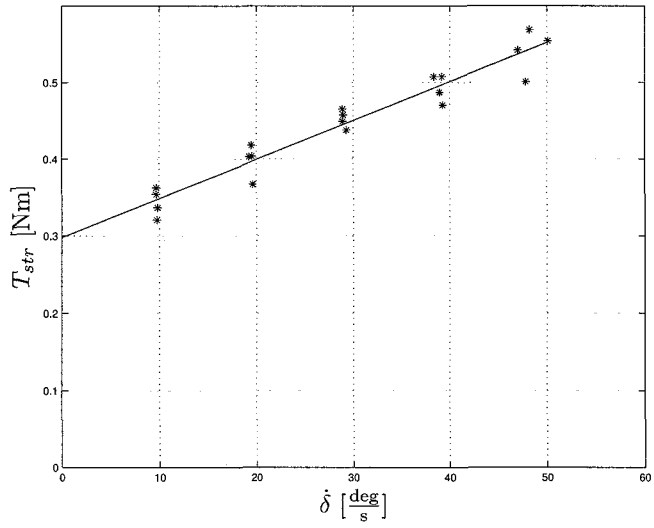


Figure 5.3: Steering torque (related to input) as a function of steer angular velocity (related to output) including first order fit (stars: data points for independent wheel units; solid: experimental data fit).

### 5.3.3 Self Aligning Torques

The tyre model, described in section 3.4, incorporates a formula for the self aligning torque in the combined slip condition. With combined slip condition, a manoeuvre consisting of simultaneous cornering and braking is indicated. However, the proposed description of the self aligning torque characteristic is somewhat simplified with respect to the approach presented in Pacejka et al. [PB97]. Moreover, the share of turn slip, denoted by $\varphi_t$, in the steady state moment generation property of the tyre is neglected. In Pacejka [Pac02], it is shown that the influence of turn slip is considerable, although the modelling is quite difficult and certainly not easy to integrate in the simplified tyre model discussed in section 3.4. Therefore, it is desired to investigate the ability of the tyre model to describe the self aligning torque $M_z$. For this reason, two different types of experiments are conducted, which will now be discussed.

The first experiment is identical to the one discussed in subsection 5.3.2, except that in this case the Moving Base is placed at the floor. The experiment, where the wheels track a certain steer angle trajectory during standstill of the Moving Base, is performed for several steer angular velocities. However, during a number of experiments, not all wheels traversed the prescribed trajectory completely. This is due to the $I^2t$ requirement of the AC servo motor, which is related

to power consumption. In general, better results are obtained for larger steer angular velocities. Using the available data, it is possible to determine the steering torque as a function of steer angular velocity at $v = 0$ km/h. In principle, this can be done for each independent wheel unit. However, as a result of the fact that all wheel units show similar characteristics, the steering torques are averaged, leading to one characteristic. This experiment is also performed on simulation level, after implementation of the characteristic from figure 5.3.

The second experiment is conducted in order to determine the steering torques in case the velocity of the Moving Base is unequal to zero. For this reason, a velocity $\overline{v}(t)$ is defined, specified by magnitude $v(t)$ and direction $\beta(t)$. The direction $\beta(t)$ is defined such that a constant steer angular velocity is obtained during a certain time period. Consequently, the magnitude $v(t)$ needs to be constant during this time period as well. Two different values for $v(t)$ are set, being 5 and 10 km/h. As a result of this particular definition of the velocity $\overline{v}(t)$, a trajectory in the $x$-$y$ plane is obtained for $\dot{\delta}$ equal to 10 deg/s and $v$ equal to 10 km/h that is too large. Therefore, this measurement cannot be performed in practice. The data, available from the remaining measurements, is used to determine the steering torque as a function of steer angular velocity at $v = 5$ km/h and $v = 10$ km/h. For the same reason as in the first experiment, the data from the independent wheel units is averaged. Again, this experiment is performed on simulation level as well.

Using the results from both experiments, it is possible to construct a three dimensional diagram, depicting the steering torque $T_{str}$ (related to input) as a function of Moving Base velocity $v$ and steer angular velocity $\dot{\delta}$. In figure 5.4, three dimensional diagrams are depicted for simulation as well as experimental data.

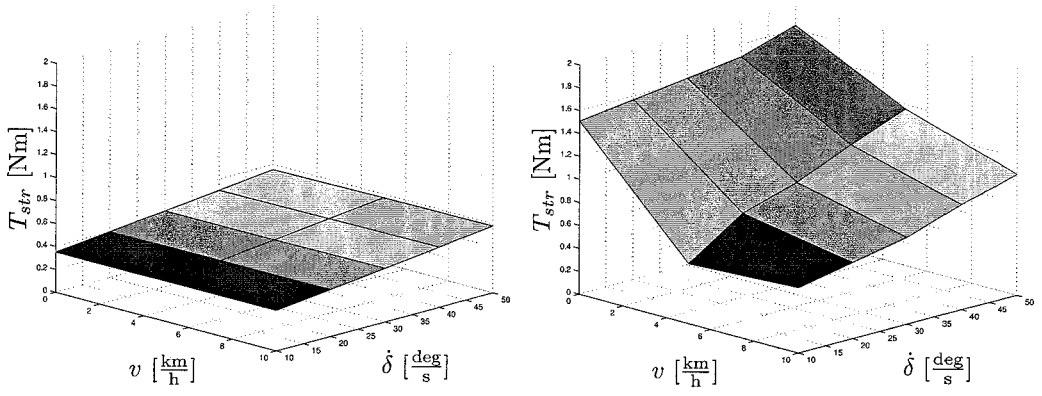


Figure 5.4: Steering torque (related to input) as a function of Moving Base velocity and steer angular velocity (related to output) *Left*: simulation; *Right*: experiment.

In the left figure in figure 5.4, the simulation results are depicted. It follows that the steering torque $T_{str}$ is more or less independent of the Moving Base velocity $v$, while it increases as a function of steer angular velocity $\dot{\delta}$. At $v = 0$ km/h, the tyre model produces no effect and the characteristic from figure 5.3 is obtained. For increasing Moving Base velocity $v$, the steering torque $T_{str}$ slightly increases as a result of the self aligning torque, computed by the tyre model. From the right figure in figure 5.4, it can be concluded that the behaviour of $T_{str}$ is different in practice. The steering torque $T_{str}$ decreases as a function of Moving Base velocity $v$ and increases as a function of steer angular velocity $\dot{\delta}$. Especially for small values of $v$, the difference between simulation and experiment is large, primarily due to the neglect of turn slip in the simulation model. Fortunately, the control of the Moving Base at low velocities is inherently not very critical. However, it is desired to improve the correspondence between simulation and experiment. This correspondence can be improved by including turn slip in the tyre model. As mentioned before, the modelling of turn slip is rather involved and will lead to a complex tyre model, which conflicts with the objective adopted during the development of this model. For this reason, a different

approach is desired. This approach can be found in the application of a look-up table. By means of a look-up table, it is possible to account for the difference between both figures in figure 5.4. Using interpolation and extrapolation, the correspondence between simulation and experiment will improve considerably.

## 5.4 Inertia Estimate

The wheels of the Moving Base are lifted again, in order to determine an estimate for the mass moment of inertia of one wheel unit around the vertical axis, denoted by $J_{st,eff}$. For this reason, a torque sine sweep is applied to each independent electrical steering system, where $T_{ij,str,ref}$ ranges from 0 to 10 Hz, using an amplitude equal to 0.7 Nm. Measurement of the resulting steering torque $T_{ij,str}$, the steer angle $\delta_{ij}$ and the steer angular velocity $\dot{\delta}_{ij}$ allows the computation of the desired estimate. Notice that $\dot{\delta}_{ij}$ is computed by dSPACE. Computation of $J_{st,eff}$ is done in two different ways. In subsection 5.4.1, a time domain approach is discussed. Because this method does not lead to satisfying results, a frequency domain approach is considered in subsection 5.4.2.

### 5.4.1 Time Domain Identification

In order to obtain an estimate for the mass moment of inertia of one wheel unit around the vertical axis, use is made of a parametric identification method. In this context, the block diagram in figure 5.5 is considered, which is set in continuous time.

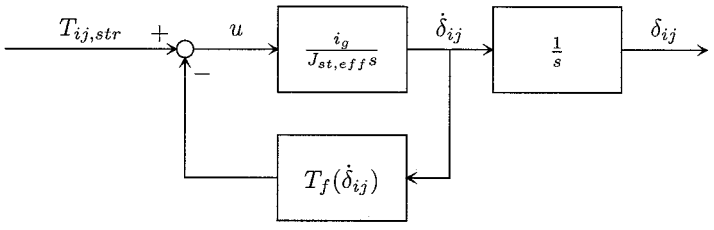


Figure 5.5: Block diagram for system identification purposes.

The input data sequence $u$ is obtained by determination of the effective torque, using $T_f(\dot{\delta}_{ij})$, which equals $T_{str}$ in (5.3). Because of the fact that it is not possible to compute the effective torque $u$ in an exact way, this may lead to difficulties during the identification procedure, due to feedback from $\dot{\delta}_{ij}$ in the generation of $u$ (closed loop data). Furthermore, the output data sequence $y$ is defined to equal $\delta_{ij}$. As a result of this input-output definition, the model to be estimated equals:

$$y = \frac{i_g}{J_{st,eff}s^2}u = \frac{\alpha}{s^2}u, \tag{5.4}$$

where $i_g$ denotes the transmission ratio of the steering system planetary gear set. This transfer function corresponds to the following continuous time state space model:

$$\begin{aligned} \dot{x} &= \begin{bmatrix} 0 & 0 \\ 1 & 0 \end{bmatrix} x + \begin{bmatrix} 1 \\ 0 \end{bmatrix} u \\ y &= \begin{bmatrix} 0 & \alpha \end{bmatrix} x + \begin{bmatrix} 0 \end{bmatrix} u + w(t), \end{aligned} \tag{5.5}$$

where $w(t)$ is an additive noise term. For identification purposes, the continuous time state space model is converted into a discrete time state space model:

$$\begin{aligned} x(kT_s + T_s) &= \begin{bmatrix} 1 & 0 \\ T_s & 1 \end{bmatrix} x(kT_s) + \begin{bmatrix} T_s \\ \frac{T_s}{100} \end{bmatrix} u(kT_s) \\ y(kT_s) &= \begin{bmatrix} 0 & \alpha \end{bmatrix} x(kT_s) + \begin{bmatrix} 0 \end{bmatrix} u(kT_s) + e(kT_s), \end{aligned} \tag{5.6}$$

with $e(kT_s)$ a noise term and $T_s$ the sampling interval. This model is used as an initial model by the prediction error method. By definition of so called structure matrices, the estimation routine is only allowed to adjust the parameter $\alpha$. Adaptation of $\alpha$ takes place in such a way that $e(kT_s)$ is minimized in a quadratic sense. After the estimation procedure is finished, the resulting discrete model is transformed to continuous time. The Bode diagram of the estimated model for the front left (1L) wheel unit is depicted in figure 5.6. Moreover, this figure contains a transfer function and coherence function estimate, obtained from the same data. A comparison reveals that the model estimated by the prediction error method is different with respect to the transfer function estimate. This difference is caused by the fact that the system does not behave like a double integrator over the entire frequency range. Especially for low frequencies, first order behaviour is present, which is accounted for by the time domain identification method. A possible explanation for this first order behaviour is the presence of closed loop data in the system, as mentioned before. For this reason, the mass moment of inertia estimate obtained from the estimated model is not reliable.

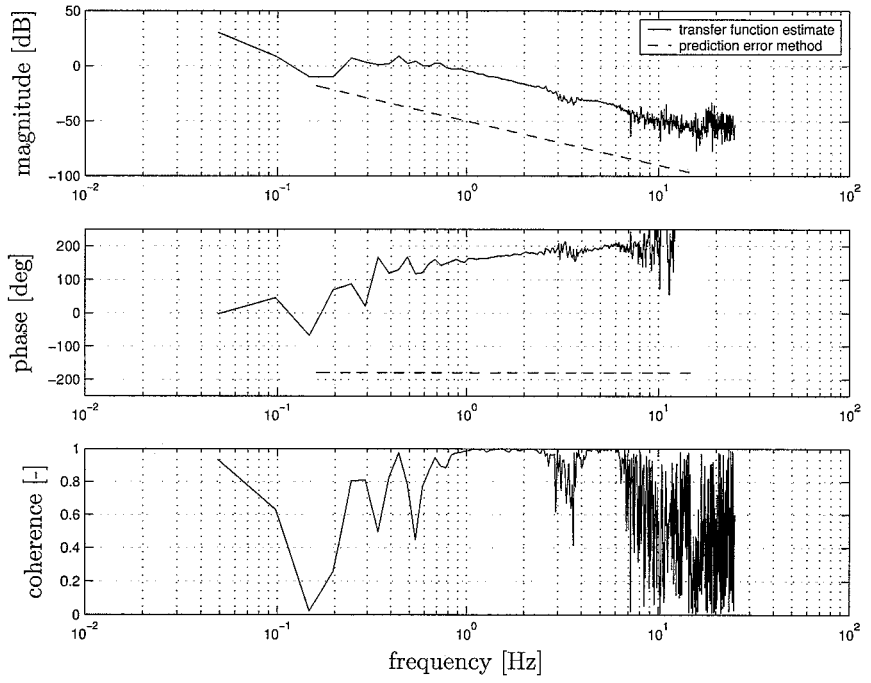


Figure 5.6: Transfer/coherence function estimate and parametric model estimate for front left (1L) wheel unit (solid: transfer function estimate; dashed: prediction error method).

### 5.4.2 Frequency Domain Identification

Hence, in order to obtain an estimate for the mass moment of inertia $J_{st,eff}$, a different approach needs to be followed. For this reason, the transfer function estimate in figure 5.6 is taken as a starting point. The frequency range with acceptable coherence function estimate is used to fit a model according to (5.4). For the front left (1L) wheel unit, this fit is depicted in figure 5.7.

Because the experiment is performed for each wheel unit, four estimates result for $J_{st,eff}$. These are given by the vector:

$$[J_{st,eff,1L}, J_{st,eff,1R}, J_{st,eff,2L}, J_{st,eff,2R}] = [2.54, 2.74, 2.84, 2.71]. \tag{5.7}$$

Averaging the four estimates in (5.7) leads to the value 2.7 kgm$^2$. This estimated value for $J_{st,eff}$ is larger than the value 2.0 kgm$^2$, which is currently being used in the simulation model.

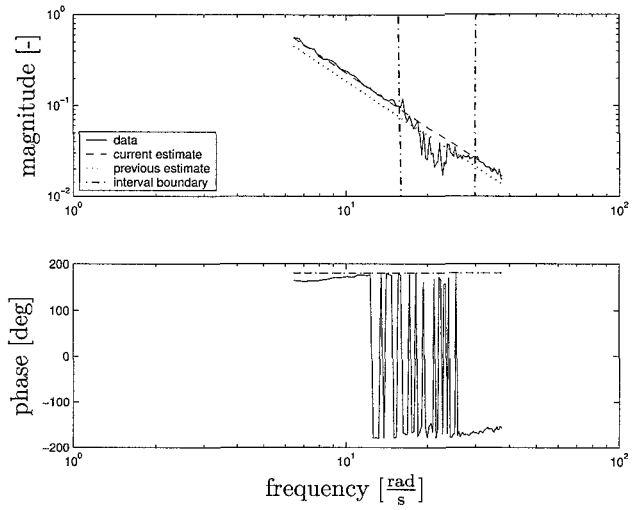


Figure 5.7: Model fit in frequency range with acceptable coherence function for front left (1L) wheel unit (solid: data; dashed: current estimate; dotted: previous estimate; dashed-dotted: excluded interval boundary).

## 5.5 Motion Control

### 5.5.1 Velocity Step Response

By setting a step velocity input, the performance of the motion controller is obtained in terms of a step response. The experiment is performed in longitudinal direction only, without application of acceleration feedforward signals in the motion controller. Notice that infinite acceleration feedforward signals would be generated in case of a step velocity input. Furthermore, the step value is set to 10 km/h and use is made of Kalman filter based position/velocity estimates. The velocity and acceleration responses for simulation as well as experiment are depicted in figure 5.8.

From this figure, several conclusions can be drawn. First, it is seen that simulation and experiment correspond rather well. The rise time for simulation and experiment approximately equals 0.4 s and 0.5 s, respectively. Notice that rise time is defined as the time it takes for the system to reach the vicinity of its new set point, see Franklin et al. [FPEN94]. Obviously, the system approaches its final value without overshoot. Moreover, it can be clearly seen that the system does not even reach its final value, for both simulation and experiment. This steady state offset is a result of the fact that only P-control is used in the motion controller, see section 4.3. From the acceleration response, it is concluded that the specified acceleration of 10 m/s$^2$ is realized during a short time period. The large peak in the experimental signal is probably caused by a local roughness in the floor. Furthermore, on simulation level, both the velocity and the acceleration response show a noise band in steady state. The corresponding frequency equals approximately 25 Hz and is caused by the tyre model. It can be shown that the transient tyre behaviour corresponds to an undamped spring behaviour at low velocities, i.e. $v_{ij,long} \rightarrow 0$.

### 5.5.2 Acceleration Feedforward

In order to investigate the influence of acceleration feedforward on the performance of the motion controller, two experiments are conducted. In both experiments, a ramp velocity signal is set as input for $v_{long,ref}$. This ramp velocity signal is specified by a constant acceleration of 5 m/s$^2$ and a final velocity equal to 18 km/h. The difference between both experiments is found in the application of acceleration feedforward. In the left figure in figure 5.9, the velocity errors

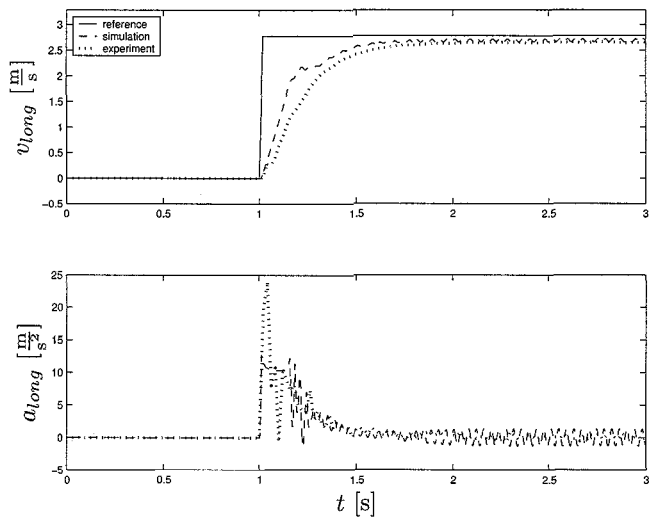


Figure 5.8: Longitudinal velocity response (Kalman filter) and acceleration response (accelerometer) on a step velocity reference for simulation and experiment (solid: reference velocity; dashed: simulation; dotted: experiment).

on simulation and experimental level are depicted, for the experiment without application of feedforward. Notice that the velocity error is defined as the difference between reference velocity and actual velocity. It can be seen that the correspondence between simulation and experiment is not very good. This also holds for the experiment with application of acceleration feedforward, see the right figure in figure 5.9. A possible explanation for the deviations between simulations and experiments can be found in figure 5.10. In this figure, the driving torques $T_{ij,drv}$ are depicted for the experiment without application of feedforward. However, similar results are obtained for the experiment with application of feedforward. It can be seen that substantial differences exist between simulation and experiment for all four electrical drive lines. The cause of this difference will be addressed in section 5.7. Because the driving torques during the experiment are substantially larger than during the simulation, this leads to a slower velocity response in the experimental case, which is seen in the left figure in figure 5.9.

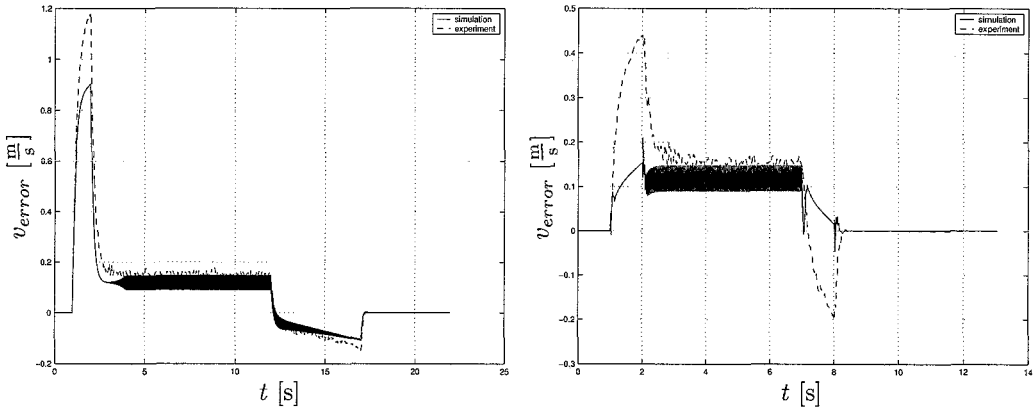


Figure 5.9: *Left*: Velocity error without application of feedforward; *Right*: Velocity error with application of feedforward (solid: simulation; dashed: experiment).

To obtain a clear comparison between both experimental responses, the velocity errors are depicted

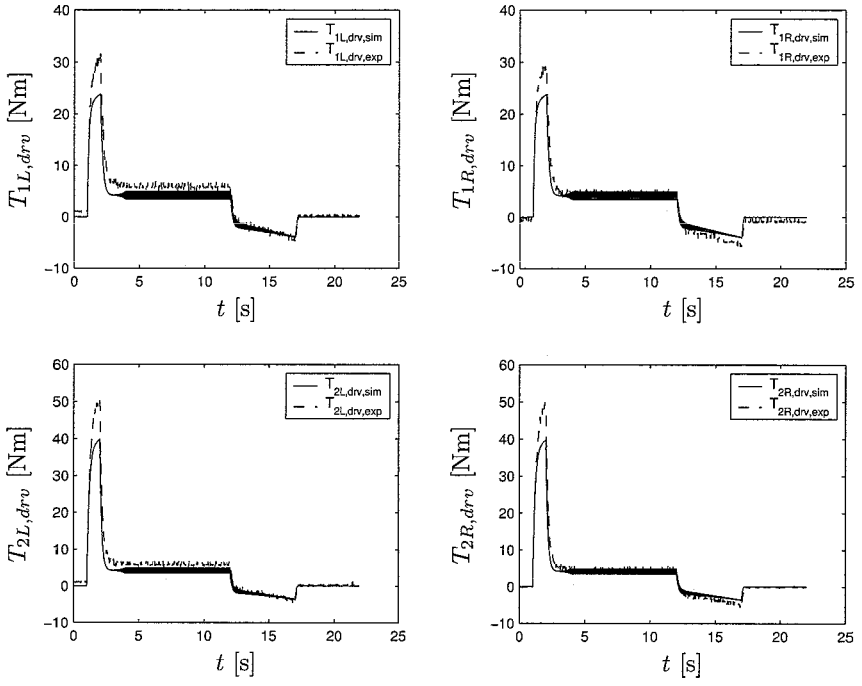


Figure 5.10: Driving torques for experiment without application of feedforward (solid: simulation; dashed: experiment).

in figure 5.11. In this figure, only the time range up to approximately 7 s is of interest, due to differences in the deceleration part of the velocity reference trajectory. During the acceleration part, it can be seen that the velocity error decreases considerably in case acceleration feedforward is applied. The maximum reduction factor appears to be slightly smaller than 3. Furthermore, it can be noticed that the steady state error equals 0.16 m/s.

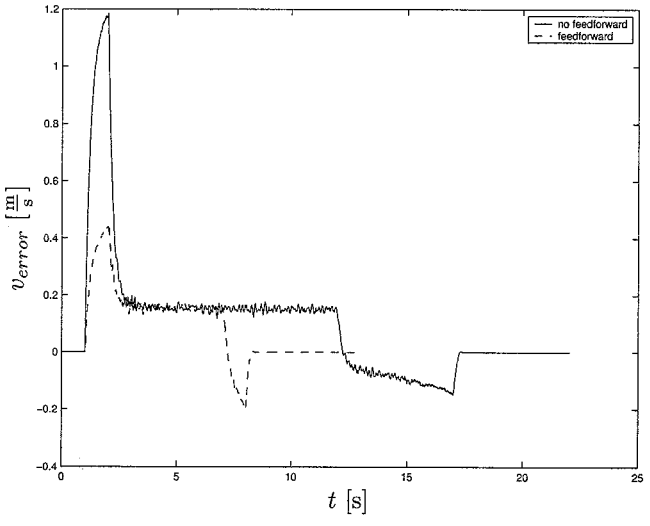


Figure 5.11: Experimental velocity errors on a ramp velocity reference without and with application of acceleration feedforward (solid: no feedforward; dashed: feedforward).

### 5.5.3 Velocity Swept Sine

In order to determine the frequency response function $v_{long,ref} \rightarrow v_{long}$, a swept sine longitudinal reference velocity is applied, which is superposed on a constant reference velocity. Both velocities are set in such a way that the resulting velocity always remains positive. As a result, the influence of the non-linear friction, occurring during a change of sign of the forward velocity, is avoided. The constant velocity level is set to 2 km/h and the amplitude for the swept sine equals 1 km/h. In theory, a resonance occurs at a frequency of approximately 25 Hz, caused by the tyres. The damping level depends on the velocity, which implies that the constant velocity level influences the frequency response. Question is if it is useful to apply a sine sweep with a maximum frequency which exceeds the mentioned 25 Hz, in order to determine the influence of the tyre. Because 25 Hz largely exceeds the bandwidth of the total system, it is likely that unmodelled effects will be measured in the frequency range from 10 to 25 Hz. Therefore, the maximum frequency of the swept sine is limited to 10 Hz. A mere accident is that the frequency response from 0 to 10 Hz is independent of the forward velocity.

It should be remarked that two experiments are performed. One without and the other with application of acceleration feedforward. From the simulation and experimental data, it is possible to determine the frequency response function $v_{long,ref} \rightarrow v_{long}$. The longitudinal velocity $v_{long}$ is represented by the Kalman filter velocity estimate. As a result, the frequency response function incorporates Moving Base dynamics as well as Kalman filter dynamics. In figure 5.12, the resulting magnitude and phase characteristics, as well as the coherence function estimates, are depicted, for the experiment without application of feedforward. The results for the experiment with application of feedforward are depicted in figure 5.13. Notice that in both cases simulation as well as experimental results are shown.

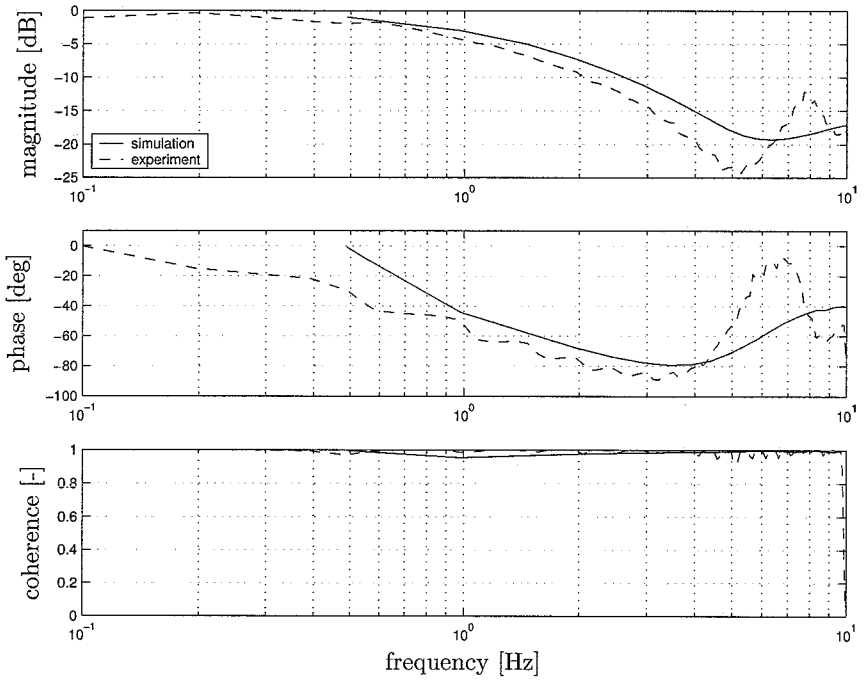


Figure 5.12: Transfer/coherence function estimate for experiment without application of feedforward (solid: simulation; dashed: experiment).

First of all, it can be concluded from figure 5.12 and figure 5.13 that the coherence for both simulation and experiment is extremely good in the frequency range up to 10 Hz. Furthermore, the magnitude as well as the phase characteristic show similar behaviour for simulation and experi-

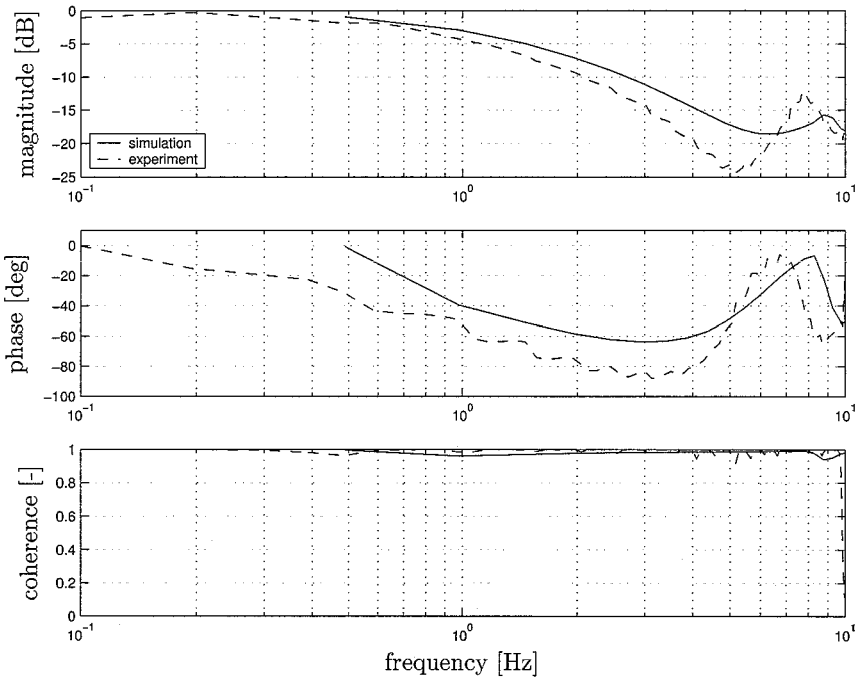


Figure 5.13: Transfer/coherence function estimate for experiment with application of feedforward (solid: simulation; dashed: experiment).

ment, although there are some large differences present in both figures. The simulation magnitude characteristic, for instance, lies above the experimental magnitude characteristic in the major part of the frequency range. This implies a better performance of the simulation model compared to the real Moving Base. Also with respect to the phase characteristic, deviations between simulations and experiments are present. Again, a possible explanation for the deviations may be the difference in driving torques between simulation and experiment. This effect is already discussed in subsection 5.5.2.

A natural specification for system performance in terms of frequency response is the bandwidth, defined to be the maximum frequency at which the output of the system will track an input sinusoid in a satisfactory manner. By convention, for the motion controlled Moving Base, the bandwidth is the frequency of $v_{long,ref}$ at which the output $v_{long}$ is attenuated to a factor 0.707 times the input, see Franklin et al. [FPEN94]. Recall that attenuation by a factor 0.707 corresponds to -3 dB. From figure 5.12, it can be concluded that the bandwidth equals 0.98 Hz and 0.77 Hz, for simulation and experiment, respectively. In addition, figure 5.13 implies a bandwidth of 0.99 Hz for the simulation and 0.77 Hz for the experiment. From these values, it can be concluded that the application of acceleration feedforward has (nearly) no influence on the bandwidth of the motion controlled Moving Base for both simulation and experiment. A possible explanation for this conclusion is that the capacity of the AC servo motors is already fully utilized in case no acceleration feedforward is applied. Furthermore, it is remarkable that the bandwidth does not exceed 1.0 Hz, because this is the typical bandwidth of corresponding transfer functions for conventional passenger cars. In the specifications namely, it is stated that the dynamic manoeuvring behaviour of the Moving Base must largely exceed the handling performance of modern road vehicles, implying a bandwidth of about 5.0 Hz. The main reason for this reduced performance is found in the settings for the PID controllers, see section 4.3. As already mentioned before, the PID controllers only consist of P-control and they are not tuned up to their maximum yet. Increasing the control gains will lead to an increase of the bandwidth of the motion controlled Moving Base.

In addition to the results discussed above, the experiment is also performed for different settings of the constant velocity level and the swept sine amplitude. From the corresponding experimental data it is concluded that the eigenfrequency of the pitch dynamics is approximately 5.5 Hz. This is close to the damped eigenfrequency used in the simulation model, which equals 4.7 Hz, see (3.4).

## 5.6 Tracking and Motion Control

In order to evaluate the performance of the Moving Base tracking and motion control combination, a second order position reference trajectory is applied. The position reference is obtained by double integration of a block-shaped acceleration profile. This implies that the position, velocity and acceleration reference signals are available. These are depicted in figure 5.14.

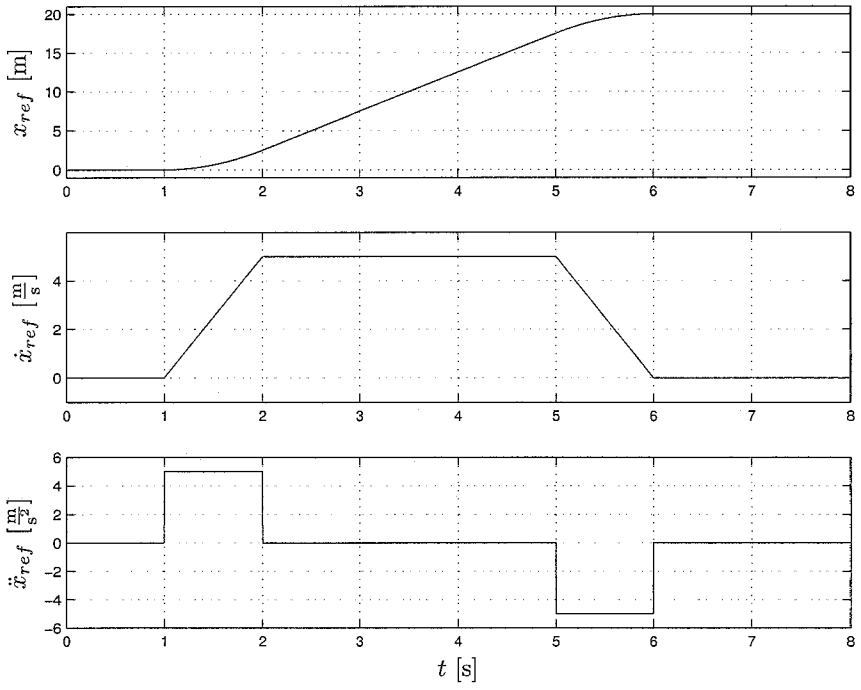


Figure 5.14: Position, velocity and acceleration reference signals in $x$-direction for evaluation of tracking and motion control combination.

Therefore, it is possible to perform three different experiments. In the first experiment, no feedforward is applied. The second experiment makes use of acceleration feedforward, while the third experiment uses velocity and acceleration feedforward. From the corresponding data, it follows that simulation and experimental results correspond reasonably well in all three cases, see Van der Meulen [Meu04]. The performance of the control system can best be characterized by computing the position errors for all experiments. These are depicted in figure 5.15. From this figure, it can be concluded that the position error does not change significantly in case acceleration feedforward is applied. However, in case velocity and acceleration feedforward are applied, the position error decreases considerably. It can be concluded that the performance is quite acceptable in the situation where use is made of both feedforward signals. Notice that in all three cases a steady state offset is present. This is due to fact that the PID controllers again only consist of P-control.

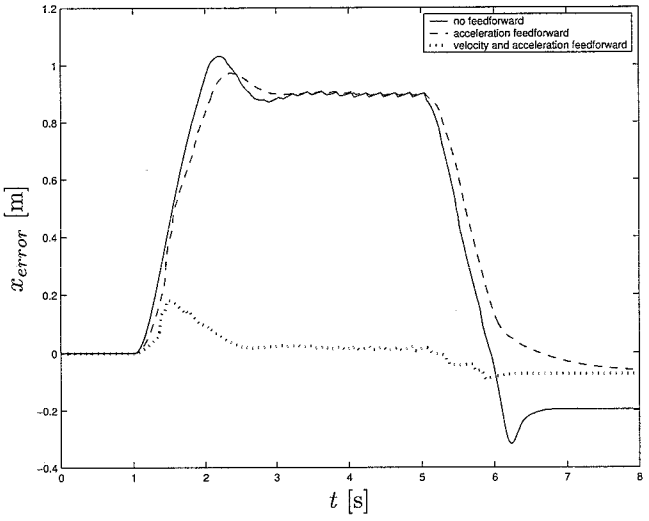


Figure 5.15: Experimental position errors on a second order position reference without and with application of feedforward (solid: no feedforward; dashed: acceleration feedforward; dotted: velocity and acceleration feedforward).

## 5.7 Flywheel Measurements

During the analysis of several experiments, it is noticed that there is a considerable difference between simulations and experiments with respect to the behaviour of the torque curves. In case a constant torque is set, without application of tracking and motion control, the resulting velocity of the Moving Base during experiments is considerably lower than during simulations. On the other hand, in case a certain velocity reference is set and motion control is applied, the desired velocity is achieved. However, the torques that are required in practice appear to be considerably larger than during simulations. This can be clearly seen in figure 5.10, for instance, where the torque responses on a ramp velocity reference are depicted, without application of acceleration feedforward. In the sequel, this specific experiment is taken as a starting point.

First, a closer look is taken at the calculation of the driving torques $T_{ij,drv}$. From (3.19), it follows that the relation between current $I_{ij,drv}$ and torque $T_{ij,drv}$ is given by:

$$T_{ij,drv} = K_{mot,drv} I_{ij,drv}, \tag{5.8}$$

with $K_{mot,drv}$ being the AC servo motor torque constant. In practice, the current $I_{ij,drv}$ is measured in the digital servo amplifiers, see section 2.3. Using this measurement and the torque constant, it is possible to compute the driving torque. On the other hand, the reference driving torques $T_{ij,drv,ref}$ are divided by the torque constant $K_{mot,drv}$, in order to compute the reference current $I_{ij,drv,ref}$. Subsequently, this reference current is applied to the local current control loop in the digital servo amplifier. Recall from appendix A that the torque constant $K_{mot,drv}$ equals 1.0 Nm/A, according to the manufacturer.

From figure 5.10, it follows that the current measurement shows a small offset in practice. Expressed in a percentage, the offset is less than 1 percent of the maximum torque. Furthermore, in figure 5.2, it is concluded that the difference between simulation and experiment with respect to the driving torque $T_{drv}$ at a constant wheel angular velocity $\omega$ is approximately 1.0 Nm. Taking into account both effects, it is possible to match simulation and experiment in the constant velocity range. However, as a result of the difference being 1.0 Nm, the torque difference during acceleration cannot be explained.

Thus, it is plausible to conclude that the simulation model is correct during constant velocity, provided that the difference in figure 5.2 is accounted for. Therefore, the cause of the torque

difference during acceleration needs to be sought in other parts of the model. Two possibilities are erroneous values for the mass $m$ of the Moving Base and the effective wheel inertia $J_{w,eff}$. To investigate these possibilities, additional simulations are performed for a mass increase of 21 percent and an effective wheel inertia increase of 457 percent, respectively. The results are similar for all wheel units. Therefore, only the results for the rear left (2L) wheel unit are depicted in figure 5.16.

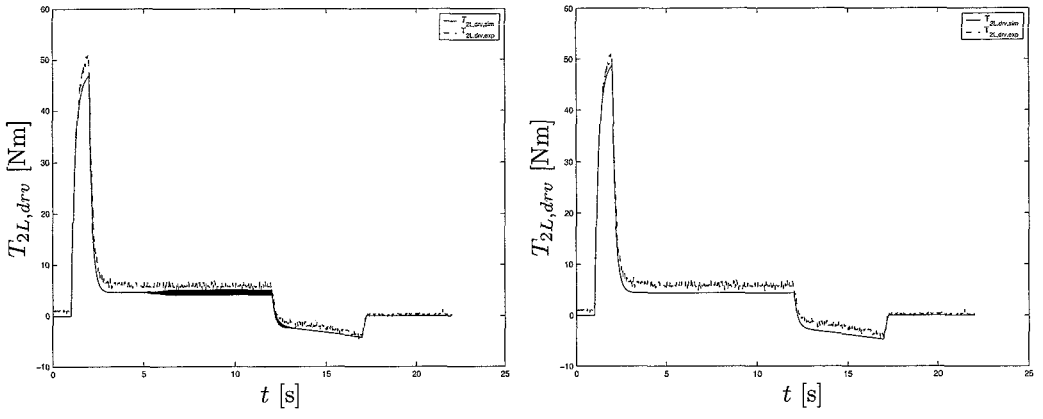


Figure 5.16: Torque responses for rear left (2L) wheel unit *Left*: Increase of mass parameter (21 percent); *Right*: Increase of effective wheel inertia parameter (457 percent) (solid: simulation; dashed: experiment).

From the left figure in figure 5.16, it follows that increasing the mass parameter from 487 kg to 587 kg is necessary to obtain a good correspondence. Hence, it is very unlikely that the difference can be attributed entirely to an erroneous mass parameter. However, a slight difference between the actual mass and the measured 487 kg, which has been obtained by weighing, is possible. This is due to the fact that weighing has been conducted before mounting the crossbeams on the Moving Base.

Increasing the effective wheel inertia parameter from 0.3589 kgm$^2$ to 2.0 kgm$^2$ is also sufficient, as can be concluded from the right figure in figure 5.16. Therefore, the effective wheel inertia needs to be increased 457 percent in order to obtain a match between simulations and experiments. Again, a small error in this parameter may be present, but this is not the full explanation for the difference in torques.

Another possibility is that an unmodelled tyre effect appears during acceleration/deceleration. As already mentioned in section 3.4, the tyre model is strongly simplified with respect to the original Magic Formula, presented in Pacejka et al. [PB97]. In order to investigate this possibility, the aforementioned experiment is repeated two times. The settings for the ramp velocity reference remain unchanged. During the first run, the tyre pressure is set to 2.0 bar, which is the standard value. Subsequently, the second run is performed, setting the tyre pressure equal to 1.0 bar. Changing the tyre pressure leads to a change in the dimensions of the contact patch between tyre and road. In case the response of both experiments is different, the dimension of the contact patch is likely to be of influence. This may indicate that certain neglected parameters in the Magic Formula actually do have importance. However, from the experimental results, it can be concluded that the tyre pressure has no influence on the response at all. With this conclusion, it is unlikely that the torque differences are due to an incorrect tyre model.

The last possibility to be considered is inaccuracy of the torque constant $K_{mot,drv}$ of the AC servo motor. Recall that the actual driving torque $T_{ij,drv}$ is computed using the torque constant $K_{mot,drv}$, according to (5.8). If the available torque constant is not correct, because it is smaller in practice, this implies a decrease in control gain. Consequently, larger currents $I_{ij,drv}$ will be measured, leading to the computation of higher driving torques $T_{ij,drv}$. It should be remarked that a possible error in $K_{mot,drv}$ also manifests itself during parts with constant velocity. In

case $K_{mot,drv}$ is reduced from 1.0 Nm/A to 0.8 Nm/A, good correspondence is obtained between simulation and experiment. The experimental torque curve, depicted in figure 5.2, also needs to be multiplied by the modified torque constant. This leads to a better match between simulation and experiment. Therefore, the influence of this difference in driving torque at constant wheel angular velocities is reduced to a minimum.

Considering all possibilities, it can be concluded that a possible inaccuracy in the torque constant $K_{mot,drv}$ is the most likely option. This conclusion is based on the simulation results, where an excessive mass increase or effective wheel inertia increase is required in order to obtain a match between simulation and experimental results. However, small differences in mass and/or effective wheel inertia may be possible. Additional tests are required to determine the torque constant $K_{mot,drv}$ explicitly.

During these additional tests, the Moving Base is placed on jacks. Attention is focused on the rear left (2L) wheel unit, the choice of which is completely arbitrary. After removal of tyre and rim, a custom made flywheel is mounted directly on the output shaft of the planetary gear set. In order to be able to determine the torque constant accurately, the flywheel mass moment of inertia needs to be known exactly. From the specifications of the manufacturer, it is concluded that the mass moment of inertia theoretically equals 5.49 kgm$^2$, see Meijer [Mei01]. However, during preceding flywheel experiments in 2001/2002, this theoretical value was questioned. It appeared to be necessary to assume a mass moment of inertia equal to 6.75 kgm$^2$ in order to obtain good correspondence between simulations and experiments, see Koopman [Koo02a]. Therefore, it is necessary to determine the flywheel mass moment of inertia accurately, in order to exclude uncertainties. Notice that 5.49 divided by 6.75 equals 0.81, possibly indicating a difference in torque constant, depending on the actual flywheel inertia.

### 5.7.1 Flywheel Mass Moment of Inertia

The flywheel mass moment of inertia is estimated by using a torsional pendulum in trifilar setup. Because such a torsional pendulum is not available, one is built especially for this purpose. The resulting setup is depicted in the right figure in figure 5.17.

A torsional pendulum is a device which can be used to experimentally measure mass moments of inertia for arbitrarily shaped objects. The torsional pendulum in trifilar setup is schematically depicted in the left figure in figure 5.17.

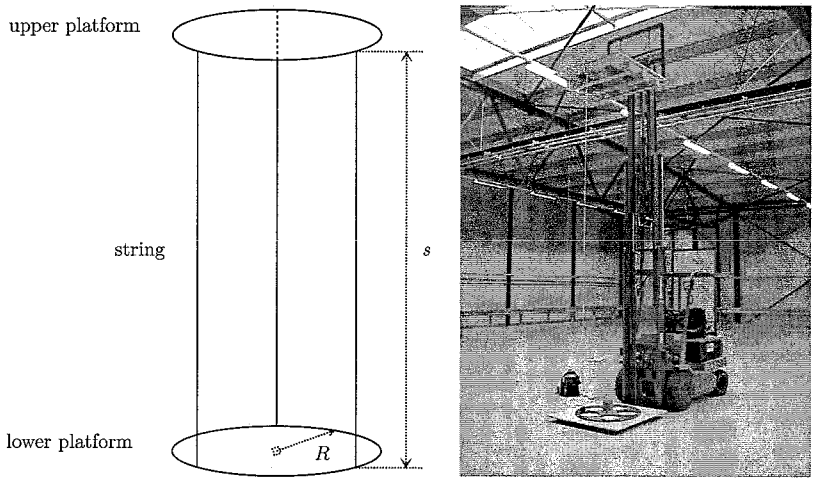


Figure 5.17: Torsional pendulum in trifilar setup *Left*: Schematic representation; *Right*: Actual setup.

Essentially, the pendulum is a vertically mounted torsional spring, where the upper platform is

fixed. The lower platform, whose mass moment of inertia is to be measured, is suspended from the bottom side of the spring. Subsequently, the lower platform is rotated slightly (less than 5 degrees) and released, so that small rotary oscillations occur. Given the (mean) period of the oscillation of the lower platform, its experimental mass moment of inertia $J$ can be found from:

$$J = \frac{mgR^2T^2}{4\pi^2 s}. \tag{5.9}$$

Here, $m$ denotes the mass of the lower platform, $g$ the gravitational acceleration and $T$ the (mean) torsional oscillation period. Furthermore, $s$ is the length of the string from the upper platform to the top of the lower platform and $R$ is the radius from the center of the lower platform to the attachment point of the strings.

From (5.9), it follows that the mass $m$ of the lower platform needs to be determined accurately. Moreover, the upper platform must be level. This also holds for the lower platform, which can be levelled by adjustment of the lengths of the three strings. Next, it is possible to measure the length $s$. The radius $R$ from the center of the lower platform to the attachment point of the strings needs to be accurately measured and fabricated as well.

After these preliminary measurements, the lower platform is started into small rotational oscillation. It is important that the oscillations are small and that translational motion of the platform is minimized as much as possible. This is necessary to obtain accurate results. Using a stopwatch, the time necessary for the lower platform to complete 100 oscillatory periods is measured. This measurement is repeated seven times, the choice of which is arbitrary. With the exception of the smallest and largest time measurement, a computation of the mean oscillation period is performed. Next, it is possible to compute the mass moment of inertia of the lower platform by using (5.9).

In case of the flywheel, no features are available to attach the suspension strings. For this reason, the determination of the mass moment of inertia is executed in two phases. First, the mass moment of inertia of the lower MDF board is measured in isolation. Subsequently, the mass moment of inertia of the lower MDF board and the flywheel is determined. It is important that the flywheel is placed in such a way that its mass center lies at the center of the lower MDF board, see figure 5.18. Since mass moments of inertia obey superposition principles, it is possible to obtain $J_{flywheel}$ by subtraction. The resulting flywheel mass moment of inertia equals $J_{flywheel} = 5.60 \pm 0.028$ kgm$^2$. This implies a deviation from the specification ($J_z = 5.49$ kgm$^2$) equal to 1.9 percent, which is quite reasonable. Notice that the accuracy of the flywheel mass moment of inertia estimate is better than 0.5 percent. The reader is referred to appendix C for the corresponding uncertainty analysis and m-file. More information about the torsional pendulum can be found in [PSU04].

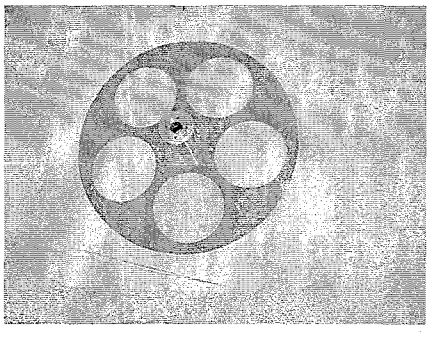

Figure 5.18: Close-up of flywheel and lower MDF board.

### 5.7.2 Drive Line Measurements

As a result of the fact that the flywheel mass moment of inertia only slightly deviates from its specification, it is very likely that the cause of the torque difference can be found in the electrical

drive line. To investigate the rear left (2L) drive line, the Moving Base is placed on jacks, as mentioned before. Subsequently, the flywheel is mounted directly on the output shaft of the planetary gear set. This experimental setup is shown in figure 5.19.

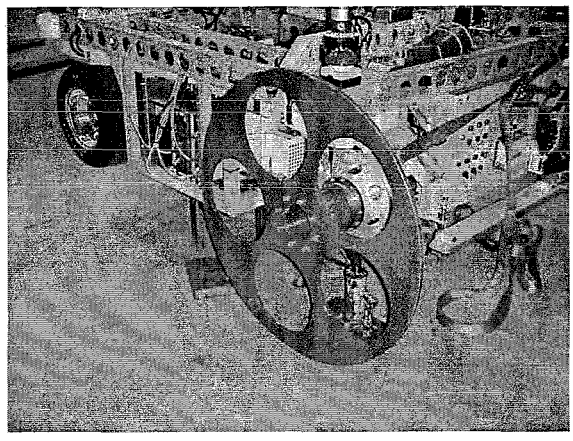

Figure 5.19: Moving Base I on jacks, with flywheel being mounted on rear left (2L) drive line.

The experiments to be discussed in this subsection are performed for Moving Base I, as well as Moving Base II and are completely identical. Furthermore, the rear left (2L) drive line is used for both Moving Bases. The main reason for using both Moving Bases is that the drive lines are identical. So, if it appears that the drive line specifications of Moving Base I, for instance, are not met, in contrast to Moving Base II, it is obvious that the problem rests entirely with the manufacturer.

The relation to be investigated is given by:

$$T_{flywheel} = I_{drv,eff} K_{mot,drv} i_g = J_{fw,eff} \dot{\omega}. \tag{5.10}$$

Here, $T_{flywheel}$ denotes the torque related to the transmission output shaft, $I_{drv,eff}$ the effective current and $\dot{\omega}$ the flywheel angular acceleration. Furthermore, the torque constant $K_{mot,drv}$ equals 1.0 Nm/A and the transmission ratio $i_g$ equals 5.000, see appendix A. The effective flywheel inertia $J_{fw,eff}$ is computed according to the relation:

$$J_{fw,eff} = (J_{rotor} + J_{brake} + J_{pgs})\, i_g^2 + J_{flywheel}, \tag{5.11}$$

where $J_{rotor}$ denotes the rotor inertia, $J_{brake}$ the brake inertia and $J_{pgs}$ the inertia of the planetary gear set. The corresponding values can be found in appendix A. It should be noted that $J_{flywheel}$ forms the major contribution to $J_{fw,eff}$. In order to obtain the effective current $I_{drv,eff}$, which is responsible for the acceleration $\dot{\omega}$, it is required to determine the steady state characteristic for the current $I_{drv}$ as a function of angular velocity $\omega$. This is done by application of velocity control to the electrical drive line and setting different constant velocity references, spread over a certain range. The resulting characteristics for both Moving Bases are depicted in figure 5.20.

Using the characteristics in figure 5.20 and interpolation techniques, it is possible to compute the effective current $I_{drv,eff}$. Next, an experiment is performed without making use of control. Basically, a constant torque reference $T_{2L,drv,ref}$ is set, which is decreased after reaching a certain maximum wheel angular velocity. The constant torque reference equals 5.0 Nm for both Moving Bases. By measuring the drive line current $I_{drv}$ and the angular velocity $\omega$ and taking into account figure 5.20, it is possible to compute $I_{drv,eff}$. Furthermore, $\dot{\omega}$ is obtained by numerical differentiation of $\omega$. Both $I_{drv,eff}$ and $\dot{\omega}$ are low pass filtered, in order to reduce the noise. Subsequently, it is possible to compute an estimate for $K_{mot,drv}$ at each sample moment, using (5.10). These estimates are depicted in figure 5.21, including the average values.

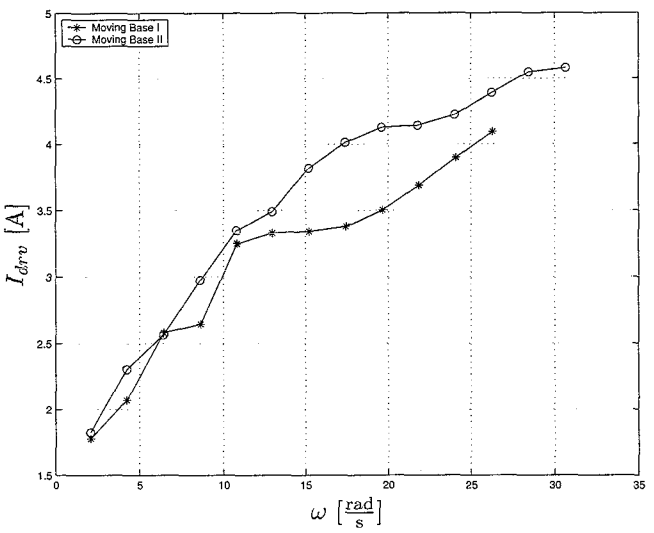


Figure 5.20: Steady state current as a function of wheel angular velocity for rotation in positive direction (solid-star: Moving Base I; solid-circle: Moving Base II).

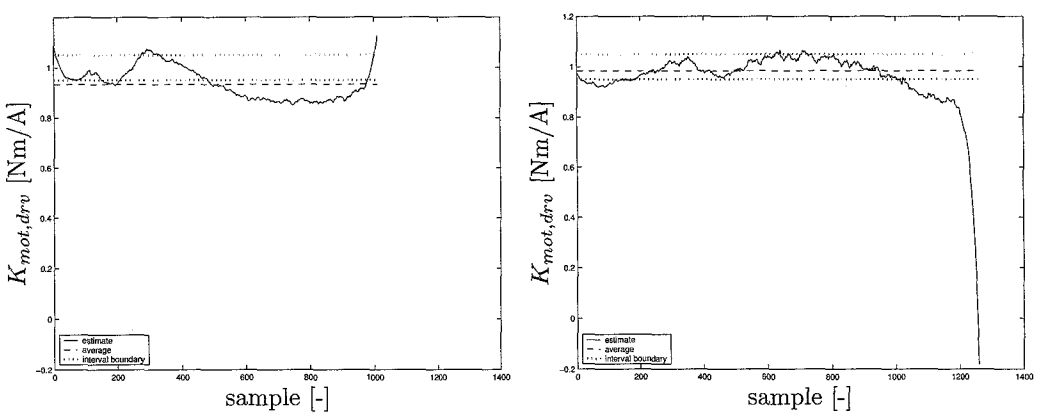


Figure 5.21: Estimated values for $K_{mot,drv}$ at each sample moment with application of low pass filtering *Left*: Moving Base I; *Right*: Moving Base II (solid: estimate; dashed: average; dotted: interval boundary).

Due to low pass filtering, the estimates for the first and last number of sample moments in figure 5.21 are unreliable. They are therefore omitted during the determination of the average value for $K_{mot,drv}$, which is also indicated in both figures. Notice that the interval boundary indicates the range of $K_{mot,drv}$ according to Mavilor Motors [Mav01]. It can be concluded that the average value equals 0.93 Nm/A for Moving Base I and 0.98 Nm/A for Moving Base II. Therefore, the torque constant of Moving Base II lies within specification, being $0.95 \leq K_{mot,drv} \leq 1.05$, while the torque constant of Moving Base I lies just slightly outside the specification range.

The computed results for $K_{mot,drv}$ appear to be relatively sensitive for the bandwidth of the applied low pass filters. For this reason, additional simulations are performed, in order to obtain more certainty with respect to $K_{mot,drv}$. In the gearbox model, use is made of the characteristics from figure 5.20. During the simulations, the constant reference torque $T_{2L,drv,ref}$ is varied until a good match is obtained between simulation and experiment for the angular velocity $\omega$. Subsequently, the torque constant $K_{mot,drv}$ is adapted until the driving torques $T_{drv}$ show a good match for simulation and experiment. The results for Moving Base II are depicted in figure 5.22. Notice

that from the left figure, it follows that simulation and experiment only match for the acceleration part. This is probably due to the fact that the kinetic energy is dissipated in the form of heat in case the battery package is sufficiently charged.

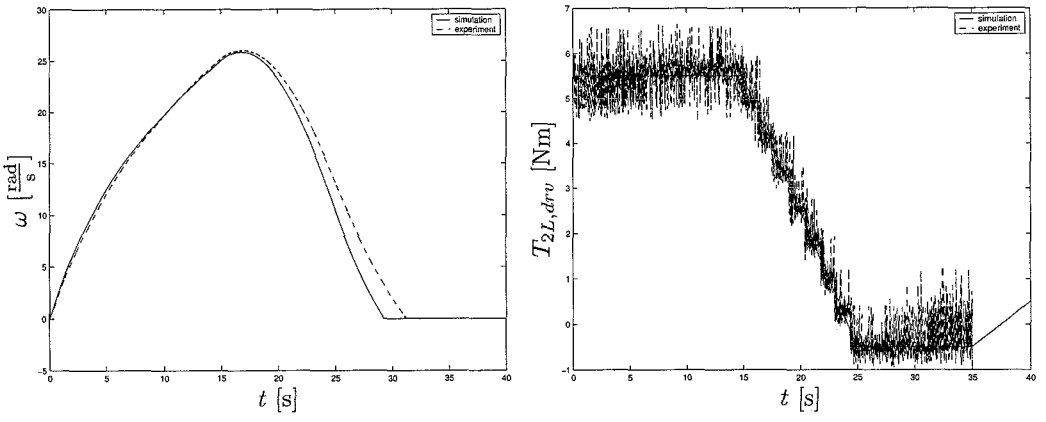


Figure 5.22: *Left*: Angular velocity as a function of time; *Right*: Driving torque (related to input) as a function of time (solid: simulation; dashed: experiment).

For Moving Base II, it follows that the torque constant equals 1.0 Nm/A in the right figure in figure 5.22. On the contrary, Moving Base I requires $K_{mot,drv}$ to equal 0.96 Nm/A in order to obtain a good match. It can be concluded that both values are inside the specification range.

These results imply that the torque constants for both Moving Bases are within specification. This raises the question if it is possible that the torque constant depends on the acceleration level. In the experiments discussed above, the acceleration is approximately 1 m/s$^2$, which is relatively low. Therefore, additional experiments are discussed in the next paragraph.

During these additional experiments, use is made of velocity control again. The velocity reference trajectory is as follows: zero, linear increase, constant velocity, linear decrease, zero. Five experiments are conducted for each Moving Base: two with acceleration/deceleration 5 m/s$^2$, two with acceleration/deceleration 8 m/s$^2$ and one with acceleration/deceleration 10 m/s$^2$. Using the available data and (5.10), it is possible to compute estimates for $K_{mot,drv}$ at each sample moment during acceleration and deceleration. These computations are performed in an identical way as described before. Estimates for $K_{mot,drv}$ during the acceleration part are depicted in figure 5.23 for both Moving Bases.

From both figures, the tendency follows that $K_{mot,drv}$ decreases for higher acceleration levels. Furthermore, it can be concluded that the values are outside the specification range, which has 0.95 Nm/A as its lower boundary. These experiments are also simulated, using the simulation model. As done before, the torque constant is varied in order to obtain a match between simulations and experiments for $T_{2L,drv}$. From the results, the same tendency for $K_{mot,drv}$ follows, with values ranging from 0.92 Nm/A to 0.86 Nm/A for Moving Base I and 0.92 Nm/A to 0.85 Nm/A for Moving Base II. This implies that $K_{mot,drv}$ is load dependent.

A different view on the results is obtained by computing the efficiency of the drive line for all five additional experiments. The efficiency $\eta$ is defined as:

$$\eta = \frac{P_{out}}{P_{in}} = \frac{J_{fw,eff}\dot{\omega}}{I_{drv}K_{mot,drv}i_g}, \tag{5.12}$$

with $P$ denoting power. Efficiency is calculated during the acceleration part and because $\dot{\omega}$ and $I_{drv}$ are nearly constant, they are averaged. Using the average values and assuming that $K_{mot,drv}$ equals 1.0 Nm/A, the efficiency follows from (5.12). This assumption actually implies that the planetary gear set is responsible for all losses. The efficiency as a function of output torque is depicted in figure 5.24.

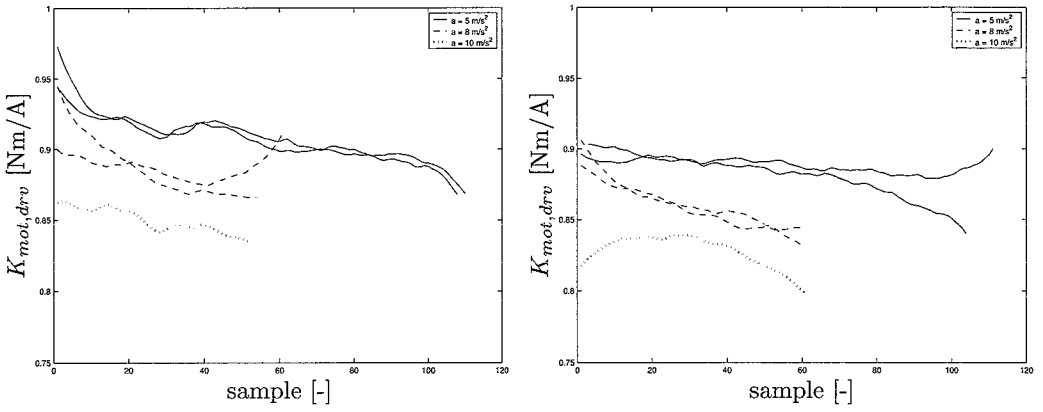


Figure 5.23: Estimated values for $K_{mot,drv}$ at each sample moment during acceleration with application of low pass filtering *Left*: Moving Base I; *Right*: Moving Base II (solid: 5 m/s$^2$; dashed: 8 m/s$^2$; dotted: 10 m/s$^2$).

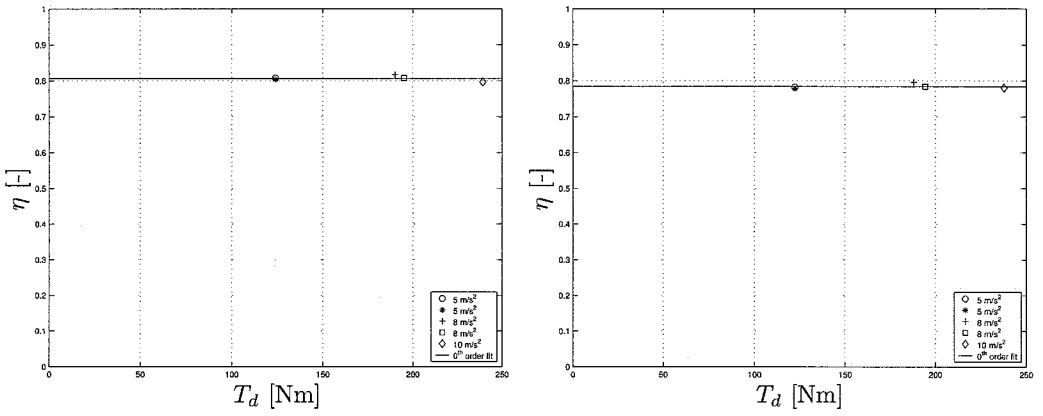


Figure 5.24: Planetary gear set efficiency during acceleration as a function of output torque using average values for current and angular acceleration *Left*: Moving Base I; *Right*: Moving Base II (circle: 5 m/s$^2$; star: 5 m/s$^2$; plus: 8 m/s$^2$; square: 8 m/s$^2$; diamond: 10 m/s$^2$; solid: $0^{th}$ order fit).

From both figures, it follows that $\eta$ is constant and approximately equal to 0.8. This implies the presence of a load dependent resistance in the planetary gear set and is a very plausible explanation. However, from appendix A, it follows that the efficiency of the planetary gear set is specified to be equal to or larger than 96 percent at a nominal torque of 400 Nm (related to output). Therefore, the planetary gear set would not satisfy its specifications.

It is also possible that both the torque constant $K_{mot,drv}$ and the planetary gear set efficiency $\eta$ do not satisfy their specifications. However, at least one of both components is outside specification. This can be concluded from the multiplication of the lowest efficiency (0.96) and the lowest torque constant (0.95), according to the specifications. The product namely results in 0.91, which is substantially larger than 0.8. In order to further investigate the question at hand, one or both components need to be tested separately, using dedicated test rigs.

In the meanwhile, it is possible to improve the correspondence between simulation and experimental results in two possible ways. A first possibility is to include an acceleration dependent torque constant $K_{mot,drv}$ in the simulation model for the drive line AC servo motor. A second possibility is to introduce a so called 'efficiency gain' in the gearbox model of the electrical drive line.

# Chapter 6

# Model Analysis

## 6.1 Introduction

In chapter 4, the Moving Base control structure is discussed. Basically, the path controller consists of tracking control and motion control, which can be considered a master-slave structure. From the validation experiments in chapter 5, it follows that the controller functions properly. However, certain specific situations may occur during execution of a position reference trajectory, which require modifications of the path controller.

As the longitudinal velocity of the Moving Base decreases, the steer angle which is required to reduce a lateral velocity/position error increases. This may lead to severe interventions of the steer angle controller in case the Moving Base is slowed down to standstill. These interventions are undesired, because they overload the AC servo motors and induce additional disturbances. In order to obtain an adequate solution for this problem, the dynamic behaviour of the Moving Base as a function of the velocity needs to be investigated.

One of the possibilities to investigate the dynamic behaviour of the Moving Base is linearization. By means of linearization, it is possible to evaluate the influence of velocity on the dynamic manoeuvring behaviour in an effective way. Linearization is performed in MATLAB, using the Moving Base simulation model and several routines. Due to insufficient time, the analysis could not be completed. The obtained results are discussed in section 6.2. Several other methods which can be used for the analysis of the simulation model are mentioned in section 6.3.

## 6.2 Linearization

During linearization, the following general system equations are taken as a starting point:

$$\begin{aligned} \dot{x}(t) &= f[x(t), u(t)] \\ y(t) &= g[x(t), u(t)], \end{aligned} \tag{6.1}$$

which are referred to as state equation and output equation, respectively. Here, $u(t)$ denotes the input vector $(m \times 1)$, $x(t)$ the state vector $(n \times 1)$ and $y(t)$ the output vector $(l \times 1)$. Essentially, linearization results in equations which constitute an approximation of (6.1), for small perturbations $\delta u(t)$ and $\delta x(t)$ with respect to the nominal values $\overline{u}(t)$ and $\overline{x}(t)$, respectively. The values $\overline{x}(t)$ and $\overline{u}(t)$ denote the nominal trajectory in state space and the nominal input signal, respectively and may vary as a function of time. The linearized equations, valid for small perturbations $\delta u(t)$ and $\delta x(t)$, are given by:

$$\begin{aligned} \delta\dot{x}(t) &= A(t)\delta x(t) + B(t)\delta u(t) \\ \delta y(t) &= C(t)\delta x(t) + D(t)\delta u(t), \end{aligned} \tag{6.2}$$

where the matrices $A(t)$, $B(t)$, $C(t)$ and $D(t)$ are obtained by partial differentiation of the functions $f$ and $g$ to $x(t)$ and $u(t)$, which subsequently are validated along the nominal trajectory:

$$A(t) = \left.\frac{\partial f}{\partial x}\right|_{\overline{x}(t),\overline{u}(t)}, \; B(t) = \left.\frac{\partial f}{\partial u}\right|_{\overline{x}(t),\overline{u}(t)}, \; C(t) = \left.\frac{\partial g}{\partial x}\right|_{\overline{x}(t),\overline{u}(t)}, \; D(t) = \left.\frac{\partial g}{\partial u}\right|_{\overline{x}(t),\overline{u}(t)}. \tag{6.3}$$

In the special case that the nominal trajectory is a stationary operating point, the matrices become constant and are denoted by $A$, $B$, $C$ and $D$. More detailed information with respect to linearization can be found in Kok [Kok01].

As already mentioned in section 6.1, use is made of the simulation model and several MATLAB routines, in order to execute the linearization procedure. In this context, 'dlinmod' is the most important MATLAB routine. Using this routine, the available discrete time system is linearized, resulting in a continuous model approximation of this discrete system, as given by (6.2). From (6.1), it follows that the inputs $u(t)$ and the outputs $y(t)$ need to be specified. The steer angles $\delta_{ij}$, for $i = 1, 2$ and $j = L, R$, are chosen as inputs, while the output is given by the lateral velocity $v_{lat}$. This choice is made because it is desired to investigate the relation between steer angles and lateral velocity, according to section 6.1. As a result, $m$ equals 4 and $l$ equals 1.

Next, it is necessary to set a certain operating point, at which the linear model is to be extracted. In this specific case, the operating point is specified by the state vector $x(t)$, the reference driving torques $T_{ij,drv,ref}$ and the reference steering torques $T_{ij,str,ref}$. The values of the state vector and the reference torques are obtained by simulation of a circular reference trajectory, with radius $R = 10$ m and constant velocity $v = 7$ km/h. At a certain time instant, the reference torques are extracted, as well as the state vector $x(t)$, with $n$ equal to 38. Subsequently, it is possible to apply the 'dlinmod' routine. This routine generates the matrices $A$, $B$, $C$ and $D$ in (6.2). Because it is desired to investigate the influence of the longitudinal velocity $v_{long}$, this procedure is repeated for constant velocities equal to 4, 5 and 6 km/h. Examining the pole locations of the system matrix $A$ in the complex plane reveals that several poles are located in the right half plane, see figure 6.1. This is the case for all considered longitudinal velocities and implies that the system is unstable, which is very unlikely. A possible explanation for this phenomenon is that the operating point is not a stationary operating point, as a result of the fact that it is obtained from a controlled situation. Therefore, a stationary operating point, or at least a somewhat unforced operating point needs to be selected in order to perform the linearization.

## 6.3 Suggestions

Besides linearization, using the MATLAB routine 'dlinmod', there are several other possibilities to obtain information about the simulation model and its properties. One of these possibilities is step testing. In this method, step references are applied to certain system inputs, after which the system output is investigated. Another possibility is to apply closed loop system identification in order to obtain a linearized model at a certain operating point.

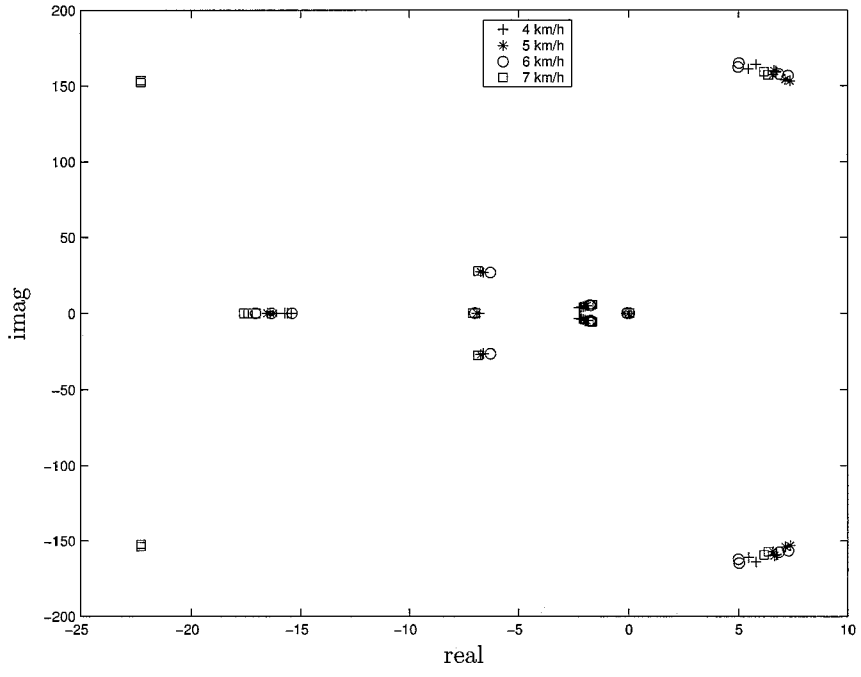


Figure 6.1: Pole locations of linearized model in complex plane for different longitudinal velocities (plus: 4 km/h; star: 5 km/h; circle: 6 km/h; square: 7 km/h).

# Chapter 7

# Conclusions and Recommendations

## 7.1 Conclusions

TNO Automotive in Helmond is currently developing a professional full scale intelligent vehicle simulator, called VEHIL. With VEHIL, new prototype intelligent vehicles can be tested in a synthetic traffic flow. First, the intelligent Vehicle Under Test (VUT) is mounted on a chassis dynamometer. Then, the VUT is placed in a simulated environment consisting of mobile robots, called Moving Bases. These Moving Bases are key components of the Hardware-In-the-Loop simulator, as they represent the surrounding traffic of the VUT. For this purpose, every Moving Base simulates the motion of a specific traffic participant relative to the VUT.

Within the framework described above, TNO Automotive has developed two high performance Automatic Guided Vehicle's (AGV's), called Moving Base I and Moving Base II. These vehicles are based on a four wheel drive and four wheel steer concept, which allows for a high handling performance in combination with the ability to carry out complex manoeuvres. In order to evaluate the behaviour of the Moving Base, extensive use is made of a dynamic simulation model. Component specifications and control system design, for instance, are based on this model. However, the full simulation model has not yet been validated. For this reason, the simulation model is validated and improved during the traineeship, by developing and executing new tests on simulation and experimental level. Moreover, certain tests make it possible to draw conclusions with respect to the overall performance of the real Moving Bases.

**Main Conclusion:**

*Introduction of the proposed improvements in the dynamic simulation model results in a relatively good correspondence between simulations and experiments for arbitrary manoeuvres.*

Several new tests are developed in order to validate and improve the simulation model. From the results of these tests, different conclusions can be drawn, which are divided into three categories. The first category is constituted by conclusions with respect to the validity of the simulation model. In general, it can be concluded that the simulation model is a good representation of the real Moving Base. There are, however, some exceptions, which will be mentioned here.

- During a steady state circular test, the simulation and experimental handling diagram do not correspond, due to an unmodelled effect in the fiber optic gyro.
- The self aligning torque characteristic computed by the simulation model is not correct, as a result of neglecting the influence of turn slip.

- In all tests, where use is made of the electrical drive lines, it is noticed that the torque responses on simulation and experimental level show substantial differences.

Conclusions with respect to the simulation model improvements constitute the second category.

- In the Moving Base simulation model, the electrical steering system gearbox model does not incorporate a friction torque as a function of steer angular velocity. For this reason, an average characteristic is determined, which can be included in the model.
- The tyre model does not take into account turn slip, the influence of which appears to be considerable. An approach is proposed to introduce the effects of turn slip into the simulation model.
- A new estimate for the mass moment of inertia of one wheel unit around the vertical axis is obtained by application of a torque sine sweep to the electrical steering system and using a frequency domain approach.
- From the drive line measurements, two different approaches are obtained, which improve the correspondence between the drive line torques on simulation and experimental level.

Finally, several conclusions can be drawn with respect to the overall performance of the Moving Bases. These are given by the third category and apply to Moving Base I, unless stated otherwise.

- The Moving Base shows nearly neutral behaviour during a steady state circular test.
- The rise time for a velocity step reference from 0 to 10 km/h equals 0.5 s.
- Application of acceleration feedforward in the motion controller leads to a decrease in the velocity error with a maximum reduction factor slightly smaller than 3.
- The bandwidth of the frequency response function $v_{long,ref} \rightarrow v_{long}$ equals 0.77 Hz, which is relatively low due to soft tuning of the PID controllers.
- Velocity feedforward in the tracking controller leads to a considerably improved performance, while the application of acceleration feedforward has a minimal influence.
- Both the tracking controller and the motion controller only consist of P-control, leading to steady state offsets.
- Drive line efficiency is below the minimum specification, which is obtained from specifications of the AC servo motor and the planetary gear set.

## 7.2 Recommendations

During the research, several issues are encountered that have remained unsolved. Furthermore, besides the proposed improvements, there are several possibilities to further improve the Moving Base performance. These are subject for further research and are discussed in the following recommendations.

- With respect to the drive line efficiency, it is desired to investigate whether the low efficiency is caused by the AC servo motor or the planetary gear set. This can be done by separately testing these components, using dedicated test rigs.
- The performance of the Moving Base can be greatly improved by modification and/or additional tuning of the existing PID controllers.
- Certain specific situations may occur during execution of a position reference trajectory, which require modifications of the control system. For this reason, a thorough analysis of the simulation model needs to be performed, requiring additional effort with respect to model linearization.

# Appendix A

# Hardware Specifications

Table A.1: Hardware specifications.

| **Mavilor MA-55 AC Servo Motor** | | | |
|---|---|---|---|
| *Characteristic* | *Symbol* | *Unit* | *Value* |
| Torque-weight ratio ±10% | $T_W$ | Nm/kg | 1.9 |
| Torque constant ±5% | $K_T$ | Nm/A | 1.0 |
| Winding resistance ±5% | $R$ | Ω | 0.2 |
| Winding inductance ±5% | $L$ | mH | 1.9 |
| Rotor inertia | $J$ | $\text{kgm}^2$ | $3.60 \cdot 10^{-3}$ |
| Electrical time constant | $\tau_E$ | ms | 7.6 |
| Brake inertia | $J$ | $\text{kgm}^2$ | $0.30 \cdot 10^{-4}$ |
| **Mavilor MSA-02 220 VAC AC Servo Motor** | | | |
| *Characteristic* | *Symbol* | *Unit* | *Value* |
| Torque-weight ratio | $T_W$ | Nm/kg | 0.74 |
| Torque constant ±5% | $K_T$ | Nm/A | 0.52 |
| Winding resistance ±5% | $R$ | Ω | 6.62 |
| Winding inductance ±5% | $L$ | mH | 32.00 |
| Rotor inertia | $J$ | $\text{kgm}^2$ | $0.05 \cdot 10^{-3}$ |
| Electrical time constant | $\tau_E$ | ms | 4.83 |
| **ServoFit PH701_0050 Planetary Gear** | | | |
| *Characteristic* | *Symbol* | *Unit* | *Value* |
| Total transmission | $i_g$ | - | 5.000 |
| Mass moment of inertia (related to input) | $J$ | $\text{kgm}^2$ | $7.26 \cdot 10^{-4}$ |
| Efficiency at nominal torque (400 Nm, related to output) | $\eta$ | % | $\geq 96$ |
| **Sumitomo Cyclo Europe FC-A 15 (G)** | | | |
| *Characteristic* | *Symbol* | *Unit* | *Value* |
| Total transmission | $i_g$ | - | 59 |
| Mass moment of inertia (related to input) | $J$ | $\text{kgm}^2$ | $0.313 \cdot 10^{-4}$ |

# Appendix B

# Experiment Information

## B.1 Experiment Descriptions

**Experiment 1:** The Moving Base drives in a circle with constant radius $R$, using tracking and motion control. The longitudinal velocity $v_{long}$ is increased very slowly (may be considered steady state), leading to a change in steer angles $\delta_{ij}$. In this way, four handling diagrams are obtained.

**Experiment 2:** In order to determine the driving torque $T_{ij,drv}$ as a function of wheel angular velocity $\omega_{ij}$, seven experiments are performed. For each experiment, a different constant longitudinal reference velocity is set. Using the measurements, an average driving torque as a function of wheel angular velocity can be computed.

**Experiment 3:** An identical torque reference signal $T_{ij,drv,ref}$ is applied to all four electrical drive lines in this experiment. Furthermore, it holds that $T_{ij,str,ref}$ equals zero, leading to a longitudinal motion. Taking into account the characteristic resulting from Experiment 2, it is possible to calculate an estimate for the mass of the Moving Base.

**Experiment 4:** The purpose of this experiment is to determine an estimate for the mass moment of inertia in vertical direction with respect to the c.o.g. of the Moving Base ($I_z$). For this reason, the wheels are first oriented such that it is possible to generate a pure rotation around the center of gravity. Subsequently, this rotation is obtained by application of an identical torque reference signal $T_{ij,drv,ref}$ to all four electrical drive lines.

**Experiment 5:** During this experiment, the Moving Base is lifted from the ground. Subsequently, the steering torque $T_{ij,str}$ is determined as a function of steer angular velocity $\dot{\delta}_{ij}$ for all four electrical steering systems. For this reason, a series of different steer angular velocities is applied.

**Experiment 6:** This experiment is identical to Experiment 5, except that the Moving Base is placed at the floor instead of being lifted from the ground.

**Experiment 7:** In addition to Experiment 6, this experiment is performed in order to determine the steering torque as a function of steer angular velocity in case the velocity of the Moving Base is unequal to zero. For this reason, a velocity $\overline{v}(t)$ is defined, specified by magnitude $v(t)$ and direction $\beta(t)$. The direction $\beta(t)$ is defined such that a constant steer angular velocity is obtained during a certain time period. It is necessary for the magnitude $v(t)$ to be constant during this time period as well.

**Experiment 8:** In this experiment, the wheels of the Moving Base are lifted again. Subsequently, a torque sine sweep is applied to each electrical steering system, by setting appropriate reference torques $T_{ij,str,ref}$. By measuring the steer angle $\delta_{ij}$ and the steer angular velocity $\dot{\delta}_{ij}$, a mass moment of inertia estimate can be computed.

**Experiment 9:** The performance of the motion controller, in terms of a step response, is obtained by setting a step velocity input. The experiment is performed in longitudinal direction only, without application of acceleration feedforward.

**Experiment 10:** Basically, this experiment is similar to Experiment 9. However, in this case a ramp velocity is set as input for $v_{long,ref}$.

**Experiment 11:** This experiment is identical to Experiment 10. In addition, an acceleration feedforward signal is applied.

**Experiment 12:** The purpose of this experiment is to determine the frequency response function $v_{long,ref} \rightarrow v_{long}$, without application of acceleration feedforward. To achieve this, a swept sine longitudinal reference velocity is applied, which is superposed on a constant reference velocity.

**Experiment 13:** The only difference with respect to Experiment 12 is that in this case acceleration feedforward is applied.

**Experiment 14:** In order to evaluate the performance of the Moving Base tracking and motion control combination, a second order position reference trajectory is applied. Furthermore, no use is made of velocity and acceleration feedforward signals.

**Experiment 15:** The experiment is identical to Experiment 14, except that in this case use is made of acceleration feedforward.

**Experiment 16:** In addition to Experiment 15, velocity feedforward is applied as well.

**Experiment 17:** In contrast to all other experiments, this experiment is performed on simulation level only. A swept sine longitudinal reference position is applied, in order to determine the frequency response function $x_{ref} \rightarrow x$.

**Experiment 18:** The steady state characteristic for current $I_{drv}$ as a function of angular velocity $\omega$ is determined in this experiment. This is done by application of velocity control to the electrical drive line and setting different constant velocity references, spread over a certain range. Notice that the rear left (2L) wheel unit of Moving Base II, which is placed on jacks, is used, in combination with the flywheel.

**Experiment 19:** Again, this experiment is performed using the rear left (2L) wheel unit of Moving Base II and the flywheel. Basically, a constant torque reference $T_{2L,drv,ref}$ is set, which is decreased after reaching a certain maximum wheel angular velocity. The constant torque reference equals 5.0 Nm.

**Experiment 20:** This experiment is identical to Experiment 18, except that in this case use is made of Moving Base I.

**Experiment 21:** This experiment is identical to Experiment 19, except that in this case use is made of Moving Base I.

**Experiment 22:** Moving Base I, with the flywheel being mounted to the rear left (2L) drive line, is used in this experiment. Five measurements are conducted, setting three different constant acceleration/deceleration levels and using velocity control.

**Experiment 23:** This experiment is identical to Experiment 22, except that in this case use is made of Moving Base II.

## B.2 Data File List

**Experiments February 12, 2004; Moving Base I**

| *Exp. No.* | *Time* | *Filename* | *Comment* |
|---|---|---|---|
| 2 | 18:34 | Exp2_1.mat | 1 [m/s] |
| 2 | 18:37 | Exp2_2.mat | 2 [m/s] |
| 2 | 18:39 | Exp2_3.mat | 3 [m/s] |
| 2 | 18:42 | Exp2_4.mat | 4 [m/s] |
| 2 | 18:45 | Exp2_5.mat | 5 [m/s] |
| 2 | 18:50 | Exp2_6_1.mat | 6 [m/s] Outside safety area |
| 2 | 18:52 | Exp2_6_2.mat | 6 [m/s] |
| 2 | 18:54 | Exp2_7.mat | 7 [m/s] |
| 3 | 18:26 | Exp3.mat | |
| 6 | 15:47 | Exp6_1.mat | $\dot{\delta}_{ij} = 20$ [deg/s] Setpoint starts too early |
| 6 | 18:08 | Exp6_2.mat | $\dot{\delta}_{ij} = 20$ [deg/s] Not all wheels rotate |
| 7 | 16:33 | Exp7_1.mat | $\dot{\delta}_{ij} = 20$ [deg/s] 5 [km/h] |
| 7 | 16:37 | Exp7_2.mat | $\dot{\delta}_{ij} = 20$ [deg/s] 5 [km/h] |
| 7 | 18:18 | Exp7_10_1.mat | $\dot{\delta}_{ij} = 20$ [deg/s] 10 [km/h] |

**Experiments February 16, 2004; Moving Base I**

| *Exp. No.* | *Time* | *Filename* | *Comment* |
|---|---|---|---|
| 4 | 16:53 | Exp4_1.mat | Measurement 1 |
| 4 | 16:55 | Exp4_2.mat | Measurement 2 |
| 6 | 16:44 | Exp6_40_1.mat | $\dot{\delta}_{ij} = 40$ [deg/s] Rear right (2R) does not rotate |
| 6 | 16:46 | Exp6_50_1.mat | $\dot{\delta}_{ij} = 50$ [deg/s] |
| 6 | 16:50 | Exp6_50_2.mat | $\dot{\delta}_{ij} = 50$ [deg/s] Not all wheels rotate |

**Experiments February 17, 2004; Moving Base I**

| *Exp. No.* | *Time* | *Filename* | *Comment* |
|---|---|---|---|
| 1 | 09:06 | Exp1_1.mat | $R = 7$ [m] |
| 9 | 10:36 | Exp9_1.mat | |
| 10 | 09:15 | Exp10_1.mat | Outside safety area |
| 10 | 09:29 | Exp10_2.mat | |
| 11 | 09:32 | Exp11_1.mat | Possible BMS shutdown |
| 11 | 10:40 | Exp11_2.mat | |
| 12 | 10:43 | Exp12_1.mat | Remote shutdown: vibrations (approximately 6 [Hz]) |
| 13 | 15:11 | Exp13_1.mat | Noodstop (Autonoom) |
| 14 | 15:28 | Exp14_1.mat | No feedforward |
| 15 | 15:22 | Exp15_1.mat | Acceleration feedforward |
| 16 | 15:17 | Exp16_1.mat | Velocity & acceleration feedforward (Measurement 1) |
| 16 | 15:25 | Exp16_2.mat | Velocity & acceleration feedforward (Measurement 2) |

**Experiments February 18, 2004; Moving Base I**

| *Exp. No.* | *Time* | *Filename* | *Comment* |
|---|---|---|---|
| 5 | 09:19 | Exp5_1l10.mat | $\dot{\delta}_{1L} = 10$ [deg/s] |
| 5 | 09:21 | Exp5_1l20.mat | $\dot{\delta}_{1L} = 20$ [deg/s] |
| 5 | 09:23 | Exp5_1l30.mat | $\dot{\delta}_{1L} = 30$ [deg/s] |
| 5 | 09:24 | Exp5_1l40.mat | $\dot{\delta}_{1L} = 40$ [deg/s] |
| 5 | 09:26 | Exp5_1l50.mat | $\dot{\delta}_{1L} = 50$ [deg/s] |
| 5 | 09:28 | Exp5_1r10.mat | $\dot{\delta}_{1R} = 10$ [deg/s] |
| 5 | 09:30 | Exp5_1r20.mat | $\dot{\delta}_{1R} = 20$ [deg/s] |
| 5 | 09:31 | Exp5_1r30.mat | $\dot{\delta}_{1R} = 30$ [deg/s] |
| 5 | 09:32 | Exp5_1r40.mat | $\dot{\delta}_{1R} = 40$ [deg/s] |
| 5 | 09:33 | Exp5_1r50.mat | $\dot{\delta}_{1R} = 50$ [deg/s] |
| 5 | 09:35 | Exp5_2l10.mat | $\dot{\delta}_{2L} = 10$ [deg/s] |
| 5 | 09:37 | Exp5_2l20.mat | $\dot{\delta}_{2L} = 20$ [deg/s] |
| 5 | 09:38 | Exp5_2l30.mat | $\dot{\delta}_{2L} = 30$ [deg/s] |
| 5 | 09:40 | Exp5_2l40.mat | $\dot{\delta}_{2L} = 40$ [deg/s] |
| 5 | 09:41 | Exp5_2l50.mat | $\dot{\delta}_{2L} = 50$ [deg/s] |
| 5 | 09:43 | Exp5_2r10.mat | $\dot{\delta}_{2R} = 10$ [deg/s] |
| 5 | 09:45 | Exp5_2r20.mat | $\dot{\delta}_{2R} = 20$ [deg/s] |
| 5 | 09:46 | Exp5_2r30.mat | $\dot{\delta}_{2R} = 30$ [deg/s] |
| 5 | 09:47 | Exp5_2r40.mat | $\dot{\delta}_{2R} = 40$ [deg/s] |
| 5 | 09:48 | Exp5_2r50.mat | $\dot{\delta}_{2R} = 50$ [deg/s] |
| 8 | 10:59 | Exp8_1l_07.mat | 1L $s\_gain8 = 0.7$ [Nm] |
| 8 | 10:56 | Exp8_1r_07.mat | 1R $s\_gain8 = 0.7$ [Nm] |
| 8 | 11:01 | Exp8_2l_07.mat | 2L $s\_gain8 = 0.7$ [Nm] |
| 8 | 10:53 | Exp8_2r_07.mat | 2R $s\_gain8 = 0.7$ [Nm] |

**Experiments March 04, 2004; Moving Base I**

| *Exp. No.* | *Time* | *Filename* | *Comment* |
|---|---|---|---|
| 10 | 16:43 | Exp10_3.mat | Unchanged settings: tyre pressure 2.0 [bar] (Outside safety area) |
| 10 | 16:50 | Exp10_4.mat | Unchanged settings: tyre pressure 2.0 [bar] |
| 10 | 17:09 | Exp10_5_1bar.mat | Unchanged settings: tyre pressure 1.0 [bar] |

**Experiments March 19, 2004; Moving Base I**

| *Exp. No.* | *Time* | *Filename* | *Comment* |
|---|---|---|---|
| 7 | 12:59 | Exp7_5_10_1.mat | $\dot{\delta}_{ij} = 10$ [deg/s] 5 [km/h] |
| 7 | 13:02 | Exp7_5_30_1.mat | $\dot{\delta}_{ij} = 30$ [deg/s] 5 [km/h] |
| 7 | 13:05 | Exp7_5_40_1.mat | $\dot{\delta}_{ij} = 40$ [deg/s] 5 [km/h] |
| 7 | 13:08 | Exp7_5_50_1.mat | $\dot{\delta}_{ij} = 50$ [deg/s] 5 [km/h] |
| 7 | 13:12 | Exp7_10_10_1.mat | $\dot{\delta}_{ij} = 10$ [deg/s] 10 [km/h] & Remote shutdown: infeasible trajectory |
| 7 | 13:22 | Exp7_10_30_1.mat | $\dot{\delta}_{ij} = 30$ [deg/s] 10 [km/h] |
| 7 | 13:25 | Exp7_10_40_1.mat | $\dot{\delta}_{ij} = 40$ [deg/s] 10 [km/h] |
| 7 | 13:28 | Exp7_10_50_1.mat | $\dot{\delta}_{ij} = 50$ [deg/s] 10 [km/h] |
| 12 | 12:11 | Exp12_2.mat | Odometry based & Safety area shutdown |
| 12 | 12:19 | Exp12_3.mat | Kalman filter based & Safety area shutdown |
| 12 | 12:26 | Exp12_4.mat | Kalman filter based |
| 13 | 12:32 | Exp13_2.mat | Kalman filter based |

**Experiments March 26, 2004; Moving Base II (Rear Left 2L)**

| *Exp. No.* | *Time* | *Filename* | *Comment* |
|---|---|---|---|
| 18 | 14:49 | Exp18_v05_1.mat | $v = 0.5$ [m/s] |
| 18 | 14:54 | Exp18_v1_1.mat | $v = 1.0$ [m/s] |
| 18 | 14:56 | Exp18_v15_1.mat | $v = 1.5$ [m/s] |
| 18 | 14:58 | Exp18_v2_1.mat | $v = 2.0$ [m/s] |
| 18 | 15:00 | Exp18_v25_1.mat | $v = 2.5$ [m/s] |
| 18 | 15:02 | Exp18_v3_1.mat | $v = 3.0$ [m/s] |
| 18 | 15:05 | Exp18_v35_1.mat | $v = 3.5$ [m/s] |
| 18 | 15:06 | Exp18_v4_1.mat | $v = 4.0$ [m/s] |
| 18 | 15:08 | Exp18_v45_1.mat | $v = 4.5$ [m/s] |
| 18 | 15:09 | Exp18_v5_1.mat | $v = 5.0$ [m/s] |
| 18 | 15:14 | Exp18_v55_1.mat | $v = 5.5$ [m/s] |
| 18 | 15:15 | Exp18_v6_1.mat | $v = 6.0$ [m/s] |
| 18 | 15:18 | Exp18_v65_1.mat | $v = 6.5$ [m/s] |
| 18 | 15:20 | Exp18_v7_1.mat | $v = 7.0$ [m/s] |
| 18 | 15:25 | Exp18_vm1_1.mat | $v = -1.0$ [m/s] |
| 18 | 15:27 | Exp18_vm3_1.mat | $v = -3.0$ [m/s] |
| 18 | 15:29 | Exp18_vm5_1.mat | $v = -5.0$ [m/s] |
| 19 | 15:31 | Exp19_t5_1.mat | $T_{2L,drv,ref} = 5.0$ [Nm] |
| 19 | 15:35 | Exp19_t5_2.mat | $T_{2L,drv,ref} = 5.0$ [Nm] |

**Experiments March 30, 2004; Moving Base I (Rear Left 2L)**

| *Exp. No.* | *Time* | *Filename* | *Comment* |
|---|---|---|---|
| 20 | 11:26 | Exp20_v05_1.mat | $v = 0.5$ [m/s] |
| 20 | 11:28 | Exp20_v1_1.mat | $v = 1.0$ [m/s] |
| 20 | 11:31 | Exp20_v15_1.mat | $v = 1.5$ [m/s] |
| 20 | 11:32 | Exp20_v2_1.mat | $v = 2.0$ [m/s] |
| 20 | 11:34 | Exp20_v25_1.mat | $v = 2.5$ [m/s] |
| 20 | 11:36 | Exp20_v3_1.mat | $v = 3.0$ [m/s] |
| 20 | 11:37 | Exp20_v35_1.mat | $v = 3.5$ [m/s] |
| 20 | 11:38 | Exp20_v4_1.mat | $v = 4.0$ [m/s] |
| 20 | 11:40 | Exp20_v45_1.mat | $v = 4.5$ [m/s] |
| 20 | 11:42 | Exp20_v5_1.mat | $v = 5.0$ [m/s] |
| 20 | 11:44 | Exp20_v55_1.mat | $v = 5.5$ [m/s] |
| 20 | 11:47 | Exp20_v6_1.mat | $v = 6.0$ [m/s] |
| 21 | 11:50 | Exp21_t5_1.mat | $T_{2L,drv,ref} = 5.0$ [Nm] |
| 21 | 11:52 | Exp21_t5_2.mat | $T_{2L,drv,ref} = 5.0$ [Nm] |
| 21 | 11:54 | Exp21_t5_3.mat | $T_{2L,drv,ref} = 5.0$ [Nm] |
| 22 | 14:46 | Exp22_v7_1.mat | $v = 7.0$ [m/s], $a = 5.0$ [m/s$^2$] |
| 22 | 14:47 | Exp22_v7_2.mat | $v = 7.0$ [m/s], $a = 5.0$ [m/s$^2$] |
| 22 | 14:52 | Exp22_v7_8_1.mat | $v = 7.0$ [m/s], $a = 8.0$ [m/s$^2$] |
| 22 | 15:05 | Exp22_v7_8_2.mat | $v = 8.5$ [m/s], $a = 8.0$ [m/s$^2$] |
| 22 | 15:08 | Exp22_v7_10_1.mat | $v = 8.5$ [m/s], $a = 10.0$ [m/s$^2$] |

**Experiments April 01, 2004; Moving Base II (Rear Left 2L)**

| *Exp. No.* | *Time* | *Filename* | *Comment* |
|---|---|---|---|
| 23 | 10:54 | Exp23_v7_1.mat | $v = 7.0$ [m/s], $a = 5.0$ [m/s$^2$] |
| 23 | 10:55 | Exp23_v7_2.mat | $v = 7.0$ [m/s], $a = 5.0$ [m/s$^2$] |
| 23 | 10:57 | Exp23_v7_8_1.mat | $v = 7.0$ [m/s], $a = 8.0$ [m/s$^2$] |
| 23 | 10:58 | Exp23_v7_8_2.mat | $v = 8.5$ [m/s], $a = 8.0$ [m/s$^2$] |
| 23 | 10:59 | Exp23_v7_10_1.mat | $v = 8.5$ [m/s], $a = 10.0$ [m/s$^2$] |

## B.3 Signal List

```
varNames={'deltadot_1Lm',
          'deltadot_1Rm',
          'deltadot_2Lm',
          'deltadot_2Rm',
          'delta_1Lm',
          'delta_1Rm',
          'delta_2Lm',
          'delta_2Rm',
          'w_1Lm',
          'w_1Rm',
          'w_2Lm',
          'w_2Rm',
          'a_longm',
          'a_latm',
          'xdot_lpm',
          'ydot_lpm',
          'psidot_g',
          'x_lpm',
          'y_lpm',
          'psi_g',
          's_r1m',
          's_r2m',
          's_r3m',
          's_r4m',
          'x_0',
          'y_0',
          'psi_0',
          'x_est',
          'y_est',
          'psi_est',
          'v_longest',
          'v_latest',
          'psidot_est',
          'flag_m',
          'ruler_ID',
          'xG_m',
          'yG_m',
          'xk',
          'yk',
          'xdotk',
          'ydotk',
          'obsolete1',
          'obsolete2',
          'obsolete3',
          'obsolete4',
          'obsolete5',
          'obsolete6',
          'obsolete7',
          'obsolete8',
          'obsolete9',
          'x_mref',
          'y_mref',
          'psi_mref',
          'xdot_mref',
          'ydot_mref',
          'psidot_mref',
          'xddot_mref',
          'yddot_mref',
          'psiddot_mref',
          'v_longref',
          'v_latref',
          'psidot_ref',
          'F_longcog',
          'F_latcog',
          'M_cog',
```

```
'F_1Lz',
'F_1Rz',
'F_2Lz',
'F_2Rz',
'T_1Ldrvref',
'T_1Rdrvref',
'T_2Ldrvref',
'T_2Rdrvref',
'T_1Lstrref',
'T_1Rstrref',
'T_2Lstrref',
'T_2Rstrref',
'delta_1Lref',
'delta_1Rref',
'delta_2Lref',
'delta_2Rref',
'I_1Ldrv'
'I_1Rdrv'
'I_2Ldrv'
'I_2Rdrv'
'I_1Lstr'
'I_1Rstr'
'I_2Lstr'
'I_2Rstr'
'spare1'
'spare2'
'spare3'
'spare4'
'spare5'
'spare6'
'spare7'
'spare8'
'a_coglongm'
'a_coglatm'};
```

# Appendix C

# Flywheel Mass Moment of Inertia

## C.1 Uncertainty Analysis

The mass moment of inertia $J$ is computed by making use of the following relation:

$$J = \frac{mgR^2T^2}{4\pi^2 s}, \tag{C.1}$$

where:

| | | |
|---|---|---|
| $m$ | [kg] | lower platform mass |
| $g$ | [m/s$^2$] | gravitational acceleration |
| $R$ | [m] | radius from lower platform center to attachment point of strings |
| $T$ | [s] | time period for one torsional oscillation |
| $s$ | [m] | length of string from upper platform to top of lower platform |

Hence, it can be concluded that the mass moment of inertia $J$ is a function of several parameters $m_i$. These quantities $m_i$ incorporate uncertainties. In order to obtain the standard uncertainty $u_J$ in the quantity $J$, the influence of the standard uncertainties $u_{m_i}$ in the quantities $m_i$ on the quantity $J$ is determined. For this reason, use is made of the following relation, see Schellekens et al. [SH00]:

$$u_J^2 = \sum_i \left( \left[ \frac{\partial J}{\partial m_i} \right]_{J_\mu} \right)^2 \cdot u_{m_i}^2, \tag{C.2}$$

where $J_\mu$ represents the most likely value of $J$. The standard uncertainty $u_J$ will now be computed separately for the lower platform and the lower platform including flywheel, respectively. Notice that the standard uncertainty in the flywheel mass moment of inertia equals the sum of both standard uncertainties.

| Quantity $M_i$ | Quantity value $m_i$ | Standard uncertainty $u(m_i)$ | Sensitivity coefficient $c_i = \frac{\partial J}{\partial m_i}$ | Contribution $u_i(J) = c_i u(m_i)$ |
|---|---|---|---|---|
| $m$ | 16.67 kg | $2.9 \cdot 10^{-2}$ kg | $2.5 \cdot 10^{-1}$ m$^2$ | $7.3 \cdot 10^{-3}$ kgm$^2$ |
| $g$ | 9.81 ms$^{-2}$ | $5.8 \cdot 10^{-3}$ ms$^{-2}$ | $4.2 \cdot 10^{-1}$ kgms$^2$ | $2.4 \cdot 10^{-3}$ kgm$^2$ |
| $R$ | $600.0 \cdot 10^{-3}$ m | $0.5 \cdot 10^{-3}$ m | $1.4 \cdot 10^{1}$ kgm | $6.9 \cdot 10^{-3}$ kgm$^2$ |
| $T$ | 3.6775 s | $4 \cdot 10^{-4}$ s | 2.2 kgm$^2$s$^{-1}$ | $9 \cdot 10^{-4}$ kgm$^2$ |
| $s$ | 4.883 m | $1 \cdot 10^{-3}$ m | $8.5 \cdot 10^{-1}$ kgm | $8 \cdot 10^{-4}$ kgm$^2$ |
| $J$ | 4.13 kgm$^2$ | | | $1.0 \cdot 10^{-2}$ kgm$^2$ |

| Quantity $M_i$ | Quantity value $m_i$ | Standard uncertainty $u(m_i)$ | Sensitivity coefficient $c_i = \frac{\partial J}{\partial m_i}$ | Contribution $u_i(J) = c_i u(m_i)$ |
|---|---|---|---|---|
| $m$ | 51.25 + 16.67 kg | $1.4 \cdot 10^{-2}$ kg | $1.4 \cdot 10^{-1}$ m$^2$ | $2.1 \cdot 10^{-3}$ kgm$^2$ |
| $g$ | 9.81 ms$^{-2}$ | $5.8 \cdot 10^{-3}$ ms$^{-2}$ | $9.9 \cdot 10^{-1}$ kgms$^2$ | $5.7 \cdot 10^{-3}$ kgm$^2$ |
| $R$ | $600.0 \cdot 10^{-3}$ m | $0.5 \cdot 10^{-3}$ m | $3.2 \cdot 10^{1}$ kgm | $1.6 \cdot 10^{-2}$ kgm$^2$ |
| $T$ | 2.7962 s | $3 \cdot 10^{-4}$ s | 7.0 kgm$^2$s$^{-1}$ | $2 \cdot 10^{-3}$ kgm$^2$ |
| $s$ | 4.883 m | $1 \cdot 10^{-3}$ m | 2.0 kgm | $2 \cdot 10^{-3}$ kgm$^2$ |
| $J$ | 9.73 kgm$^2$ | | | $1.8 \cdot 10^{-2}$ kgm$^2$ |

From the data in the tables above, it can be concluded that the flywheel mass moment of inertia equals $J_{flywheel} = 5.60 \pm 0.028$ kgm$^2$. This implies a deviation from the specification ($J_z = 5.49$ kgm$^2$) equal to 1.9 percent, which is quite reasonable. Notice that the accuracy of the flywheel mass moment of inertia estimate is better than 0.5 percent.

## C.2 M-File

```
% FLYWHEEL_INERTIA.m
%
% General:
% ------------------------------------------------------------------------------
% Creation      : 09-03-2004
% Adapted       : 10-03-2004
% Editor        : S.H. van der Meulen
% TNO Automotive
%
% Summary:
% ------------------------------------------------------------------------------
% Computation of flywheel mass moment of inertia, including standard deviation.

% Initialization:
clear all
close all
clc

% Theoretical consideration:
% ------------------------------------------------------------------------------
% Specifications flywheel according to "Tennen Machinefabriek BV":
rho_s=7.8e3;                            % [kg/m^3]  density for steel
m_flyt=0.00660847*rho_s;                % [kg]      flywheel mass
Jz_flyt=0.00070397*rho_s;               % [kgm^2]   flywheel moment of inertia around z-axis

% Specifications MDF-board:
la=1.22;                                % [m]       length specification
lb=1.22;                                % [m]       width specification
lh=18*1e-3;                             % [m]       height specification
rho_mdf=0.6*1e3;                        % [kg/m^3]  density for MDF (estimated)
m_mdft=(la*lb*lh)*rho_mdf;              % [kg]      theoretical mass estimate
Jz_mdft=m_mdft*(la^2+lb^2)/12;          % [kgm^2]   mass moment of inertia

% Model function: J = (m g R^2 T^2)/(4 pi^2 s):
% m : [kg]      lower platform mass
% g : [m/s^2]   gravitational acceleration
% R : [m]       radius from lower platform center to attachment point of strings
% T : [s]       time period for one torsional oscillation
% s : [m]       length of string from upper platform to top of lower platform

% Measurements:
% ------------------------------------------------------------------------------
g=9.81;                                 % [m/s^2]   table
u_g=0.01/sqrt(3);                       % [m/s^2]   "rechthoekige verdeling"

m_fly=51.25;                            % [kg]      force transducer (kg mode)
u_m_fly=0.025/sqrt(3);                  % [kg]      digital display: "rechthoekige verdeling"
```

```
m_mdf=163.5/g;                          % [kg]      force transducer (N mode)
u_m_mdf=0.5/g/sqrt(3);                  % [kg]      digital display: "rechthoekige verdeling"

R=600.0*1e-3;                           % [m]       calibrated ruler (DIN 866/2)
u_R=0.5*1e-3;                           % [m]       Type B: experience

% s_fly=4.75+0.156;                       % [m]       cord + ruler
% u_s_fly=1.0*1e-3;                       % [m]
s_fly=(4901-18)*1e-3;                   % [m]       ruler
u_s_fly=1.0*1e-3;                       % [m]

% s_mdf=4.75+0.156;                       % [m]       cord + ruler
% u_s_mdf=1.0*1e-3;                       % [m]
s_mdf=(4901-18)*1e-3;                   % [m]       ruler
u_s_mdf=1.0*1e-3;                       % [m]

N=100;                                  % [-]       number of periods

Tmdf1=6*60+7.71;                        % 06 : 07 71 measurement 1
Tmdf2=6*60+7.72;                        % 06 : 07 72 measurement 2
Tmdf3=6*60+7.86;                        % 06 : 07 86 measurement 3
Tmdf4=6*60+7.73;                        % 06 : 07 73 measurement 4
Tmdf5=6*60+7.79;                        % 06 : 07 79 measurement 5
Tmdf6=6*60+7.70;                        % 06 : 07 70 measurement 6
Tmdf7=6*60+7.80;                        % 06 : 07 80 measurement 7

% Do not use lowest (Tmdf6) and highest (Tmdf3) measurement in computation:
T_mdf=mean([Tmdf1,Tmdf2,Tmdf4,Tmdf5,Tmdf7])/N;
u_T_mdf=std([Tmdf1,Tmdf2,Tmdf4,Tmdf5,Tmdf7]/N); % Type A:   statistical analysis

% 09-03-2004:
% Tfly1=4*60+39.30;                       % 04 : 39 30 measurement 1
% Tfly2=4*60+39.35;                       % 04 : 39 35 measurement 2
% Tfly3=4*60+39.18;                       % 04 : 39 18 measurement 3
% Tfly4=4*60+39.16;                       % 04 : 39 16 measurement 4

% 10-03-2004:
Tfly1=4*60+39.64;                       % 04 : 39 64 measurement 1
Tfly2=4*60+39.64;                       % 04 : 39 64 measurement 2
Tfly3=4*60+39.64;                       % 04 : 39 64 measurement 3
Tfly4=4*60+39.58;                       % 04 : 39 58 measurement 4
Tfly5=4*60+39.54;                       % 04 : 39 54 measurement 5
Tfly6=4*60+39.64;                       % 04 : 39 64 measurement 6
Tfly7=4*60+39.60;                       % 04 : 39 60 measurement 7

% Do not use lowest (Tfly5) and highest (Tfly6) measurement in computation:
T_fly=mean([Tfly1,Tfly2,Tfly3,Tfly4,Tfly7])/N;
u_T_fly=std([Tfly1,Tfly2,Tfly3,Tfly4,Tfly7]/N); % Type A:   statistical analysis

% Computation of mass moments of inertia:
Jz_mdf=(m_mdf*g*R^2*T_mdf^2)/(4*pi^2*s_mdf);
Jz_fly=((m_mdf+m_fly)*g*R^2*T_fly^2)/(4*pi^2*s_fly);
disp('Flywheel mass moment of inertia around z-axis: ')
Jz=Jz_fly-Jz_mdf

% Uncertainty analysis:
% MDF-board separately:
c_m_mdf=Jz_mdf/m_mdf
c_g_mdf=Jz_mdf/g
c_R_mdf=2*Jz_mdf/R
c_T_mdf=2*Jz_mdf/T_mdf
c_s_mdf=Jz_mdf/s_mdf

uJ_m_mdf=c_m_mdf*u_m_mdf
uJ_g_mdf=c_g_mdf*u_g
uJ_R_mdf=c_R_mdf*u_R
```

```
uJ_T_mdf=c_T_mdf*u_T_mdf
uJ_s_mdf=c_s_mdf*u_s_mdf

% MDF-board and flywheel:
c_m_fly=Jz_fly/(m_mdf+m_fly)
c_g_fly=Jz_fly/g
c_R_fly=2*Jz_fly/R
c_T_fly=2*Jz_fly/T_fly
c_s_fly=Jz_fly/s_fly

uJ_m_fly=c_m_fly*u_m_fly
uJ_g_fly=c_g_fly*u_g
uJ_R_fly=c_R_fly*u_R
uJ_T_fly=c_T_fly*u_T_fly
uJ_s_fly=c_s_fly*u_s_fly

% Standard uncertainty:
u_Jz_mdf=sqrt(sum([uJ_m_mdf^2,uJ_g_mdf^2,uJ_R_mdf^2,uJ_T_mdf^2,uJ_s_mdf^2]))
u_Jz_fly=sqrt(sum([uJ_m_fly^2,uJ_g_fly^2,uJ_R_fly^2,uJ_T_fly^2,uJ_s_fly^2]))
disp('Standard uncertainty in Jz: ')
u_Jz=u_Jz_mdf+u_Jz_fly
```

# Bibliography


[BDA+98] S.M. Bennett, R. Dyott, D. Allen, J. Brunner, R. Kidwell, and R. Miller, *Fiber Optic Rate Gyros as Replacements for Mechanical Gyros*, American Institute of Aeronautics and Astronautics (1998), no. 4401.

[Bes03] I.J.M. Besselink, *Vehicle Dynamics 4L150 - Lecture Sheets*, Eindhoven University of Technology, Department of Mechanical Engineering, 2003.

[Cro] Crossbow Technology, *Accelerometers - High Sensitivity LF Series*, Data Sheet.

[FPEN94] G.F. Franklin, J.D. Powell, and A. Emami-Naeini, *Feedback Control of Dynamic Systems*, Third ed., Addison-Wesley Publishing Company, 1994.

[GKN+99] A. Gelb, J.F. Kasper, Jr., R.A. Nash, Jr., C.F. Price, and A.A. Sutherland, Jr., *Applied Optimal Estimation*, The M.I.T. Press, 1999.

[Kok01] J.J. Kok, *Regelen van Multivariabele Systemen 4A560*, Eindhoven University of Technology, Department of Mechanical Engineering, 2001.

[Koo02a] M.R. Koopman, *Measurement data ATS/AGV*, TNO Work File, TNO Automotive, 2002.

[Koo02b] ———, *Stageverslag ATS/AGV - Inbedrijfstelling ATS/AGV*, TNO Report 02.OR.AC.006.1/MRK, TNO Automotive, 2002.

[KP00] A.C.M. van der Knaap and J. Ploeg, *ATS/CAR - Advanced Transport Systems/Computer Analysis of Road vehicles*, TNO Report 97.RASID.2647.1/AVDK, TNO Automotive, 2000.

[Mav] Mavilor Motors, *AC Servo Motors - MSA Series*, Data Sheet.

[Mav01] ———, *AC Servo Motors - MA Series*, 2001, Data Sheet.

[Mei01] A. Meijer, *Quotation - Manufacture of flywheel on behalf of ATS/AGV*, September 2001, Quotation No. 981380.

[Meu04] S.H. van der Meulen, *Measurement Data Moving Base I and Moving Base II*, TNO Work File, TNO Automotive, May 2004.

[Pac02] H.B. Pacejka, *Tyre and Vehicle Dynamics*, First ed., Butterworth-Heinemann, 2002.

[PB97] H.B. Pacejka and I.J.M. Besselink, *Magic Formula Tyre Model with Transient Properties*, Vehicle System Dynamics Supplement **27** (1997), p. 234–249.

[PK00] J. Ploeg and A.C.M. van der Knaap, *Tyre 1.0*, ATS/CAR Documentation, TNO Automotive, 2000.

[PK03a] ———, *Brushless DC Drive 1.01*, ATS/CAR Documentation, TNO Automotive, 2003.

[PK03b] ———, *Wheel Inertia 1.12*, ATS/CAR Documentation, TNO Automotive, 2003.

[PKV02] J. Ploeg, A.C.M. van der Knaap, and D.J. Verburg, *ATS/AGV – Design, Implementation and Evaluation of a High Performance AGV*, Intelligent Vehicle (IV'2002), 2002 Symposium, IEEE Intelligent Transportation Systems Council, June 2002.

[Plo03a] J. Ploeg, *ATS/AGV – Advanced Transport Systems/Automatic Guided Vehicle*, TNO Werkdocument, TNO Automotive, 2003, Werkpakket 02: Regeling en Simulatie.

[Plo03b] ———, *Regelingontwerp ATS/AGV – Advanced Transport Systems/Automatic Guided Vehicle*, TNO Werkdocument, TNO Automotive, 2003, Werkpakket 02: Regeling en Simulatie.

[PSU04] The Pennsylvania State University, *Torsional Pendulum – Determining Mass Moments of Inertia*, http://www.mne.psu.edu, March 2004.

[SH00] P.H.J. Schellekens and H. Haitjema, *Meten en Signaalverwerking 4C350 – Precision Engineering: Inleiding Metrologie*, Eindhoven University of Technology, Department of Mechanical Engineering, 2000.

[VKP02] D.J. Verburg, A.C.M. van der Knaap, and J. Ploeg, *VEHIL – Developing and Testing Intelligent Vehicles*, Intelligent Vehicle (IV'2002), 2002 Symposium, IEEE Intelligent Transportation Systems Council, June 2002.